

Faculty of Sciences
Physics and Astronomy

The fundamental role of cardiac tissue morphology in electrical signal propagation

Nina N. Kudryashova

Thesis submitted in the fulfillment of the requirements for the degree of
Doctor (Ph.D.) in Sciences: Physics

Promotor: Prof. Dr. Alexander V. Panfilov
Co-promotor: Prof. Dr. Konstantin I. Agladze

Ghent, 2018

Promotors:

Prof. Dr. Alexander V. Panfilov (UGent)

Prof. Dr. Konstantin I. Agladze (MIPT, Moscow)

Examination Committee:

Prof. Dr. Dirk Poelman (UGent)

Prof. Dr. Henri Verschelde (UGent)

Prof. Dr. Roeland Merks (CWI Amsterdam)

Prof. Dr. Olivier Bernus (IHU Liryc, Bordeaux)

Dr. D.A.Pijnappels (LUMC, Leiden)

Dr. Hans Dierckx (UGent)

Dr. Nele Vandersickel (UGent)

The research of this thesis was funded by Bijzonder Onderzoeksfonds (BOF), Russian Foundation for Basic Research (RFBR) and Russian Federal “5top100” Program.

Nina Kudryashova, 2018

Cover design: Sergey Efimov, 2018

Contents

Introduction	4
Thesis Outline	10
1 Arrhythmogenic role of the border between two areas of cardiac cells alignment	15
2 Conditions for uni-directional block due to anisotropy in a model of human ventricular tissue	37
3 Excitation wave propagation in a patterned multi-domain cardiac tissue	63
4 Virtual cardiac monolayers for electrical wave propagation	73
5 Self-organization of conducting pathways explains electrical wave propagation in cardiac tissues with high fibrosis	115
Summary	139
Samenvatting	145
Acknowledgments	155

Introduction

Cardiac arrhythmias

According to the reports of the World Health Organization, cardiovascular disease (CVD) is the major cause of death in the world, accounting for 46% of all deaths caused by non-communicable diseases and equivalent to 17.5 million deaths per year [1]. In 90% of cases, CVD occurs in patients older than 65. In 4 out of 5 lethal CVD cases, cardiac arrhythmia was present [2]. Overall, cardiac arrhythmia is involved in 21% of all fatal outcomes.

Cardiac arrhythmia is an abnormal propagation of the electrical excitation waves, which control the contraction of the heart. Normally, these electrical waves initiate contraction of the heart chambers in the correct sequence, allowing for the most efficient blood pumping. Cardiac arrhythmias perturb normal signal propagation, which results in reduced cardiac output. In most of the cases, cardiac arrhythmias occur as a result of formation of abnormal sources of excitation, or *reentry* [3]. These reentries, in turn, form due to a block of propagation, which occurs when waves cannot propagate through a certain region in a certain direction. The blocked wave takes a detour around the obstacle and eventually may start rotating around it. Such a persistent, self-sustaining circulation around the defect, such as scar, is called *anatomical* reentry. The wave can also rotate around its own tip forming a spiral, which is called *functional* reentry. Both types of reentries often have a higher frequency than the normal cardiac rhythm, and therefore they can overdrive the low-frequency signals from the sinus node and take over the control over the heart. Therefore, cardiac reentry breaks the symmetry of normal signal propagation and may result in persistent arrhythmia.

Electrical signals in the heart

Propagation of the signals in the heart is a result of two main processes: *excitation* of cardiac cells and transmission of this excitation from one excited cell to another. In resting state, cardiomyocytes maintain the negative transmembrane potential on their membrane. The excitation corresponds to the change in transmembrane potential of the cell (depolarisation), which occurs

as a result of the activation of various ion channels. There are many types of these channels in the cell membrane, each of which transfers specific ions and thus creates electric current. Each type of ionic currents has a special time and voltage dependence, which results in a complex sequence of changes in transmembrane potential. This characteristic resulting signal is called *action potential*.

The depolarised (excited) cell then transmits the signal further, by depolarising the neighbouring cells. All cells are connected via intercellular junctions called *gap-junctions*, which allow ions diffuse from one cell to another, practically merging internal volumes of the cells. Once excited, the cell further enters the *refractory* state, meaning that it needs time to recover before transmitting signal again. During this period, the cell does not respond to any depolarising stimulation.

These basic properties of cardiac cells: ability to get excited, transmit excitation and remain refractory afterwards, are already sufficient to describe the complex spatiotemporal patterns in cardiac tissue during arrhythmia.

Cardiac tissue structure

Propagation of the waves in two and three dimensions is affected by the texture of cardiac tissue, which includes not only excitable and contractile cells (*cardiomyocytes*), but also inexcitable connective tissue (*fibroblasts*) and intercellular collagen barriers. The cells of connective tissue, or fibroblasts, even outnumber the cardiomyocytes [4] in a normal adult human heart. The fibroblasts are vitally important during prenatal development of the heart since they produce the extracellular matrix which guides cardiac cells inducing the formation of cardiac bundles. Due to this structure, wave propagation in the heart is highly *anisotropic*: the velocity of the wave propagation along the cardiac fibers is 2-6 times faster than in the orthogonal directions [5].

Anisotropy and block formation are closely related. It was shown that direction in which blocks of propagation occur first in response to high-frequency stimulation depends on the local orientation of myocardial fibers [6]. It was shown that the cardiac tissue consisting of multiple anisotropic regions with different fiber directions under certain conditions, such as the influence of cer-

tain drugs, can become a source of reentry [7]. Relation of anisotropy and arrhythmias is also a basis of one of the most widely used mechanisms of cardiac arrhythmias called anisotropic re-entry [8]. Overall, anisotropy complicates the excitation pattern in the heart and also may play an arrhythmogenic role, as will be shown further in this work [9].

However, the biophysical mechanisms of both anisotropy and block formation due to anisotropy are still not completely understood. One of the major problems here is that wave propagation and block formation occur at the tissue level and involve millions of cardiac cells. However, excitation of each cardiac cell occurs as a result of subcellular processes, such as the opening of the ion channels and diffusion of the ions through gap junctions. The multi-scale nature of cardiac arrhythmias that spread from the subcellular level to tissue or even organ scale complicates the research. Besides, the data on the ultrastructure of the cells, which is the location of different ion channels and gap-junctions, was not available until recently.

Physiological role of anisotropic propagation

On the whole organ level, the heart is designed for efficient contraction and blood pumping. The optimal mechanical properties are achieved by integration of vectors of force generated by specifically aligned cardiac bundles. During systole, the left ventricle volume decreases by 61% (from 52 to 20 mL) for only 13% decrease in muscle fibre length. This amplification of the local contractions occurs due to the complex alignment of cardiac fibers.

The fiber orientation is clearly visible on the macroscopic scale after removal of the fat and epicardial tissue. Dissections of the heart have shown that the fibers in the ventricular wall change their direction from endocardium to epicardium [10, 11], composing a right-handed helix in the epicardial layer and left-handed helix in the subendocardial layer. These two helixes merge at the apical vortex and form the structure called *vortex cordis* [10]. The controversy remains about the mechanism creating this architecture and about how this dual helical configuration influences function [12].

The angle between the fibers in epicardial and endocardial layers plays an important role in contraction, twisting of the chambers and resulting cardiac

output [13]. Subendocardial fibers are oriented at 60° to the circumferential direction, whereas subepicardial fibers are oriented at -60° . This alignment results in the $100\text{--}120^\circ$ change in fiber direction across the ventricular wall, which is called *rotational anisotropy*. During heart failure, the ventricles obtain more spherical shape, which also alters the rotational anisotropy angle, increasing the angles from 60° to 90° . As a result of this structural change, collective contraction efficiency decreases [13].

Many ideas have been proposed to represent ventricular architecture. A common one is the reduction of the complex architecture down to three discrete layers [12], which explain the overall mechanics of twisting of the heart. On the other hand, this simplified model neglects the intramural mechanical and electrical connections, which can be though important for understanding of arrhythmias. The fact remains that alignment of the anisotropic bundles results in the most efficient contraction, but at the same time this complexity affects electrical signal propagation and may lead to cardiac arrhythmias [14].

Fibrotic remodelling

The risk of having an arrhythmia increases substantially after 35 years, reaching the peak at 75 years [15]. This applies to both lethal ventricular arrhythmias and less dangerous atrial arrhythmias, bradyarrhythmia, and tachyarrhythmias. The increase in risks is associated with age-related changes in the cardiac tissue, both structural and functional.

One of the major changes accompanying aging is *fibrosis*, which is an excessive growth of the connective tissue in the heart. In fibrosis, a number of fibroblasts increases and collagen is deposited between cardiac bundles [16, 17]. The change in the extracellular matrix affects cells phenotype [18] and the distribution of ion channels in the cell membrane shifts towards their lateral localisation [17]. All these factors disturb normal signal propagation and may lead to arrhythmia.

In addition to fibrosis, cardiomyocytes tend to increase their volume with aging. It is usually caused by hypertension, which is common in older patients. These changes in structure (fibrosis and cardiomyocyte hypertrophy) taken together are called *cardiac remodeling*, and it is aimed to compensate the

increased pressure on cardiac walls. However, in the long-term perspective, it is considered to be one of the key factors of cardiac arrhythmogenicity [19, 20].

All of these gradual changes in tissue structure are hidden from observation, which complicates the studies of cardiac remodeling. There are currently no methods of non-invasive long-term *in vivo* imaging of the cardiac tissue at the cellular level [21]. Therefore, alternative approaches were needed to advance studying the principles of normal or abnormal cardiac tissue growth and development.

Such an alternative approach should employ mathematical modeling in combination with experiments on controlled cardiac tissue formation. The need for a model of this kind that would represent morphology of the cardiac tissue was expressed in a number of strategic publications reviewing the progress in the area [22, 23]. Despite the fact that such model was required, there was no morphological model for the cardiac tissue.

Analogous models already existed for many other tissues, and there were several well-established approaches in developmental biology for modelling of various tissue patterns. One of the most widely used models was inspired by theories of magnetism and is called the Cellular Potts Model (CPM) or, more specifically, the Glazier-Graner-Hogeweg (GGH) model [24–26]. With the use of this model, such processes as root growth [27], vascularisation [28], cardiac cell differentiation [29], life cycle of the *Dictyostelium discoideum* [30], vascular system development [31], etc. were studied. The strongest part of the CPM models is that this energy can be extended with the extra terms to include new forces or fields, which makes this approach so robust and widely used.

Computer modelling of cardiac arrhythmias

Computer simulations of the heart have progressed immensely during past decades. The very first attempts to model cardiac activity were undertaken in the 1920s and reproduced only the main feature of a cardiac cell: all-or-none response to stimulation. The modern state-of-art models have an enormous amount of biological details ranging from the microscopic level with individual ionic currents and their time and voltage dependences, to the macroscopic scale with the accurate representation of the cardiac anatomy. The multi-scale

approach is widely used nowadays, which is capable of predicting the global outcome of the alteration in the functioning of different subcellular elements. Such models typically include a hierarchy of different levels of organisation: 1) on the subcellular scale, the ionic currents were described; 2) on the scale of a single cell, the action potential and restitution properties of the cell are reproduced; 3) on the tissue scale velocities and spatiotemporal patterns such as spiral waves are reflected; and 4) finally on the organ scale realistic geometry of the heart is included. The personalised features from specific patients can also be taken into account on different levels, which makes this approach suitable for personalised medicine [32].

In this study, we have used both generic models, which reproduce the key aspects of signal propagation in cardiac tissues, and specifically designed detailed models for neonatal rat and adult human ventricular myocytes. We have also extended the electrical description of the heart cells with the realistic structural model, for the first time introducing the tools from the field of developmental biology to explain growth and development of cardiac tissue layers. Overall, the work presented with this thesis contributes to the major trend in a modern biophysical computer modeling which focuses on more integrative multi-scale models, which predict emerging behaviour on the tissue scale from processes on the lower levels of organisation.

Aims and Objectives

We aimed to study the role of the anisotropy and heterogeneity of the cardiac tissue in the emergence of cardiac arrhythmias. Therefore, the following aims were set:

1. To explain the mechanism of the unidirectional block in anisotropic cardiac tissue and to show the reentry onset in computer simulations of human cardiac tissue.
2. To study the range of parameters in which the unidirectional block in the human heart can occur, and how the ion channel blockers and ionic concentrations affect the probability of such block formation.

3. To develop a computational model for the cardiac tissue layer formation, which explains the origination of the morphological and functional anisotropy.
4. To apply the developed model to study the origins of the cardiac tissue anisotropy and arrhythmogenicity of the anisotropic tissue.
5. To explain the paradoxical wave propagation in samples with high fibrosis.

Thesis Outline

In **Chapter 1**, we suggest a new mechanism of the uni-directional block on the boundary between regions with different fiber directions. We have shown in a generic FitzHugh-Nagumo model [33, 34] that the uni-directional block occurs due to source-sink mismatch when the wave transits from the slow propagation across cardiac fibers to the fast propagation along them. We have compared the delays due to source-sink mismatch with the experimental data. We have proposed a specific architecture of cardiac tissue, which causes the onset of a reentry due to the uni-directional block in anisotropic tissue.

We further studied the conditions for the uni-directional block in **Chapter 2**. We have used a detailed ionic model of human cardiomyocytes (TNNP [35]) to find the probability of block formation in normal and pathological conditions in the human heart. We have shown that classical antiarrhythmic drugs are inefficient in this scenario of reentry formation and may even slightly increase the probability of uni-directional block. The model predictions suggested that anisotropy-induced block of propagation may occur in ventricles in hyperkalemia.

In **Chapter 3**, we demonstrate that the structure of cardiac tissue at the cellular level significantly affects the stability of wave propagation. An isotropic homogeneous sample of cardiac tissue and a sample with local anisotropy were compared. It was shown that local anisotropy causes blocks of propagation and increases arrhythmogenicity.

In **Chapter 4**, we propose a novel mathematical model for cardiac tissue formation. The process of model validation is described and the meaning

of parameters is discussed. The resulting tissue morphologies and electrical wave propagation in virtual tissues were compared with the experiment. All of the distinctive features of the real cardiac cells are reproduced. We have also applied the developed model of tissue growth to study morphological determinants of the anisotropy of electrical wave propagation.

In **Chapter 5**, we have applied the morphological model of cardiac tissue formation to explain the paradoxical wave propagation in the samples with high fibrosis. We suggested that the self-organisation of the cardiomyocytes may be explained with the mechanisms of cardiac syncytium formation. We have reproduced the branching pattern formed by cardiomyocytes that was observed in experiments. The model predicted the decay of the velocity with the increase in the percentage of fibroblasts, which reproduced the dependence measured in experiments.

Author's personal contribution

All computer modeling and experimental data processing were performed by the author herself. Experimental data were provided to the author by colleagues: the Laboratory of Biophysics of Excitable Systems.

References

- [1] World Health Organization, "World Health Statistics 2016," tech. rep., WHO, 2016.
- [2] R. Mehra, "Global public health problem of sudden cardiac death.," *Journal of electrocardiology*, vol. 40, pp. S118–22, 2007.
- [3] J. M. Davidenko, A. V. Pertsov, R. Salomonsz, W. Baxter, and J. Jalife, "Stationary and drifting spiral waves of excitation in isolated cardiac muscle.," *Nature*, vol. 355, pp. 349–51, 1992.
- [4] L. Yue, J. Xie, and S. Nattel, "Molecular determinants of cardiac fibroblast electrical function and therapeutic implications for atrial fibrillation.," *Cardiovascular research*, vol. 89, pp. 744–53, 2011.
- [5] A. G. Kléber, M. J. Janse, and V. G. Fast, "Normal and Abnormal Conduction

- in the Heart,” in *Comprehensive Physiology* (R. Terjung, ed.), Hoboken, NJ, USA: John Wiley & Sons, Inc., 2011.
- [6] C. Delgado, B. Steinhaus, M. Delmar, D. R. Chialvo, and J. Jalife, “Directional Differences in Excitability and Margin of Safety for Propagation in Sheep Ventricular Epicardial Muscle,” *Circulation Research*, 1990.
- [7] C. W. Zemlin and A. M. Pertsov, “Bradycardic onset of spiral wave re-entry: structural substrates,” *Europace*, vol. 9, no. suppl_6, pp. vi59–vi63, 2007.
- [8] A. Wit, S. Dillon, and J. Coromilas, “Anisotropic reentry as a cause of ventricular tachyarrhythmias in myocardial infarction,” *Cardiac Electrophysiology: From Cell to Bedside*, pp. 511–526, 1995.
- [9] N. Kudryashova, A. Teplenin, Y. Orlova, L. Selina, and K. Agladze, “Arrhythmogenic role of the border between two areas of cardiac cells alignment,” *Journal of Molecular and Cellular Cardiology*, vol. 76, pp. 227–234, 2014.
- [10] J. S. Robb and R. C. Robb, “The normal heart: anatomy and physiology of the structural units,” *American Heart Journal*, vol. 23, no. 4, pp. 455–467, 1942.
- [11] D. D. Streeter, “Gross morphology and fiber geometry of the heart,” *Handbook of physiology*, pp. 61–112, 1979.
- [12] G. Buckberg, J. I. E. Hoffman, A. Mahajan, S. Saleh, and C. Coghlan, “Cardiac mechanics revisited: the relationship of cardiac architecture to ventricular function,” *Circulation*, vol. 118, no. 24, pp. 2571–2587, 2008.
- [13] S. Nakatani, “Left ventricular rotation and twist: why should we learn?,” *Journal of cardiovascular ultrasound*, vol. 19, no. 1, pp. 1–6, 2011.
- [14] A. G. Kléber and Y. Rudy, “Basic mechanisms of cardiac impulse propagation and associated arrhythmias,” *Physiological reviews*, vol. 84, pp. 431–88, 2004.
- [15] G. V. Chow, J. E. Marine, and J. L. Fleg, “Epidemiology of arrhythmias and conduction disorders in older adults,” *Clinics in geriatric medicine*, vol. 28, pp. 539–53, 2012.
- [16] N. G. F. Anna Biernacka, “Aging and Cardiac Fibrosis,” *Aging and Disease*, vol. 2, pp. 158–173, 2014.
- [17] S. Dhein and S. B. Hammerath, “Aspects of the intercellular communication in aged hearts: effects of the gap junction uncoupler palmitoleic acid,” *Naunyn-Schmiedeberg’s archives of pharmacology*, vol. 364, pp. 397–408, 2001.
- [18] R. Rath, J. B. Lee, T.-L. Tran, *et al.*, “Biomimetic Microstructure Morphology

- in Electrospun Fiber Mats is Critical for Maintaining Healthy Cardiomyocyte Phenotype,” *Cellular and Molecular Bioengineering*, vol. 9, pp. 107–115, 2016.
- [19] S. F. A. Askar, B. O. Bingen, M. J. Schali, *et al.*, “Similar arrhythmicity in hypertrophic and fibrotic cardiac cultures caused by distinct substrate-specific mechanisms,” *Cardiovascular Research*, vol. 97, no. 1, pp. 171–181, 2013.
- [20] N. A. Trayanova, P. M. Boyle, H. J. Arevalo, and S. Zahid, “Exploring susceptibility to atrial and ventricular arrhythmias resulting from remodeling of the passive electrical properties in the heart: A simulation approach,” *Frontiers in Physiology*, vol. 5, no. Nov, p. 435, 2014.
- [21] J. R. Martina, P. H. Bovendeerd, N. de Jonge, *et al.*, “Simulation of Changes in Myocardial Tissue Properties During Left Ventricular Assistance With a Rotary Blood Pump,” *Artificial Organs*, vol. 37, pp. 531–540, 2013.
- [22] Z. Ma, J. Wang, P. Loskill, *et al.*, “Self-organizing human cardiac microchambers mediated by geometric confinement,” *Nature Communications*, vol. 6, p. 7413, 2015.
- [23] J. R. Hussan, M. L. Trew, and P. J. Hunter, “A Mean-field Model of Ventricular Muscle Tissue,” *Journal of Biomechanical Engineering*, vol. 134, no. 7, p. 071003, 2012.
- [24] F. Graner and J. Glazier, “Simulation of biological cell sorting using a two-dimensional extended Potts model,” *Physical review letters*, vol. 69, pp. 2013–2016, 1992.
- [25] J. Glazier and F. Graner, “Simulation of the differential adhesion driven rearrangement of biological cells,” *Physical review. E, Statistical physics, plasmas, fluids, and related interdisciplinary topics*, vol. 47, pp. 2128–2154, 1993.
- [26] N. J. Savill and P. Hogeweg, “Modelling Morphogenesis: From Single Cells to Crawling Slugs,” *Journal of Theoretical Biology*, vol. 184, no. 3, pp. 229–235, 1997.
- [27] V. A. Grieneisen, J. Xu, A. F. M. Marée, P. Hogeweg, and B. Scheres, “Auxin transport is sufficient to generate a maximum and gradient guiding root growth,” *Nature*, vol. 449, pp. 1008–13, 2007.
- [28] R. M. H. Merks, E. D. Perryn, A. Shirinifard, and J. A. Glazier, “Contact-inhibited chemotaxis in de novo and sprouting blood-vessel growth,” *PLoS computational biology*, vol. 4, p. e1000163, 2008.
- [29] M. A. Knewitz and J. C. M. Mombach, “Computer simulation of the influ-

- ence of cellular adhesion on the morphology of the interface between tissues of proliferating and quiescent cells.,” *Computers in biology and medicine*, vol. 36, pp. 59–69, 2006.
- [30] A. F. Marée and P. Hogeweg, “How amoeboids self-organize into a fruiting body: multicellular coordination in *Dictyostelium discoideum*.,” *Proceedings of the National Academy of Sciences of the United States of America*, vol. 98, pp. 3879–83, 2001.
- [31] R. M. H. Merks and J. A. Glazier, “Dynamic mechanisms of blood vessel growth.,” *Nonlinearity*, vol. 19, pp. C1–C10, 2006.
- [32] H. J. Arevalo, F. Vadakkumpadan, E. Guallar, *et al.*, “Arrhythmia risk stratification of patients after myocardial infarction using personalized heart models,” *Nature communications*, vol. 7, 2016.
- [33] R. FitzHugh, “Mathematical models of threshold phenomena in the nerve membrane,” *The Bulletin of Mathematical Biophysics*, vol. 17, pp. 257–278, 1955.
- [34] J. Nagumo, S. Arimoto, and S. Yoshizawa, “An active pulse transmission line simulating nerve axon,” *Proceedings of the IRE*, vol. 117, no. m V, pp. 2061–2070, 1962.
- [35] K. H. W. J. ten Tusscher, D. Noble, P. J. Noble, and a. V. Panfilov, “A model for human ventricular tissue.,” *American journal of physiology. Heart and circulatory physiology*, vol. 286, pp. H1573–89, 2004.

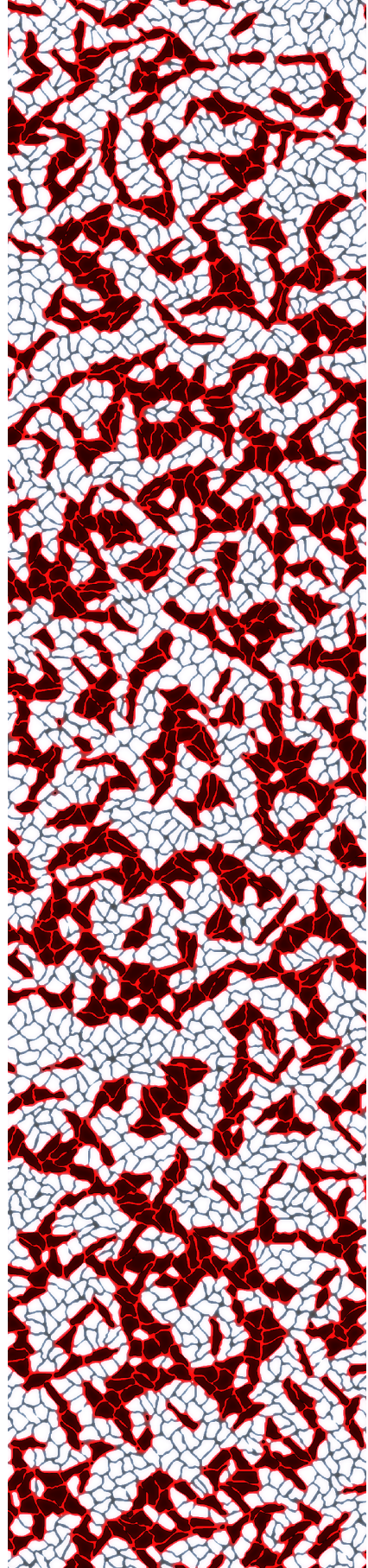
Chapter 1

Arrhythmogenic role of the border between two areas of cardiac cells alignment

NN Kudryashova¹, AS Teplenin¹, YV Orlova²,
LV Selina¹, and K Agladze¹

¹Moscow Institute of Physics and Technology, Dolgoprudny, Russia

²iCeMS Research Building, Yoshida Honmachi, Sakyo-ku, Kyoto 606-8501, Japan



Abstract

The goal of this study is to develop experimental and computational models of the excitation transition between areas of cardiac tissue with different anatomical anisotropy. Alignment of seeded neonatal rat cardiomyocytes was achieved with the aid of guiding polymer (PMGI) nanofibers, and two areas with orthogonal alignment were placed into a contact. It was found that the excitation wave crossing border between the areas with different alignment direction experiences substantial perturbation, up to the complete conduction block. In addition to the experimental study, this effect was analyzed computationally using generic FitzHugh-Nagumo reaction-diffusion model. It was shown that the non-monotonous changes of the excitation wave velocity on this boundary may be explained by the source/sink mismatch. Thus, the border may play pro-arrhythmogenic role.

Keywords: excitation, cardiomyocytes, tissue culture, optical mapping, FitzHugh-Nagumo model.

Published: Kudryashova, N.N., Teplenin, A.S., Orlova, Y.V., Selina, L.V., & Agladze, K. (2014). Arrhythmogenic role of the border between two areas of cardiac cells alignment. *Journal of Molecular and Cellular Cardiology*. <http://doi.org/10.1016/j.yjmcc.2014.09.003>.

Introduction

Bioengineered cardiac implants are believed to play very important role in a contemporary regenerative medicine of heart [1, 2]. In general, such an implant constitutes a cultured tissue patch based on a specific scaffold which provides structural and functional environment for the cardiac cells grown on it. Usually, scaffolds represent polymer matrices made of the non-toxic, biocompatible and, desirably, biodegradable materials. The polymer matrices may be as simple as sponge-like slabs, containing cells [3, 4], as well as highly ordered assemblies of the cell sheets [5]. Nowadays it is clearly understood that the architecture of the tissue patch greatly influences its functionality [6]. In designing scaffolds for the prospective implants, a lot of attention was paid to mechanical and structural matching of the cultured tissue patches to the genuine cardiac tissue [7, 8]. It was also shown that this mechanical matching increases efficiency of pluripotent cells differentiation into cardiomyocytes [9]. In this study, we attract attention to the important aspect of the implanted cardiac tissue: matching of AP conduction of the host tissue and the implant. The mechanical contraction of the heart tissue follows AP propagation and is orchestrated by it. The heterogeneities in the heart tissue may perturb propagation of AP and serve as the sources of re-entry formation – the most dangerous heart arrhythmia [10–12]. If the conduction properties of the host tissue and the implant are mismatching, the border zone may create problems for the excitation propagation. This mismatching may be based on the different physiological properties of the cells, constituting the tissue, such as activity of ion channels, coupling between cells (gap-junctions protein expression), and architectural differences between the tissue parts. In addition, it is known that the intact heart area with an abrupt change of the fiber orientation may be arrhythmogenic [13, 14] and development of the model representing such system would be of general interest in studies of the reentry formation.

We developed an experimental model for the study of the excitation propagation at the border zone between two areas with differently aligned cardiac cells. It was shown earlier, that propagation speed greatly depends on the cell alignment, being faster along cells than in the perpendicular direction [15–18]. The model is based on the polymer nanofibers, providing guiding support for

the cardiomyocytes seeded on them and controlling their elongation in the direction of fibers [18]. The matrix, representing two areas of nanofibers with the different directions of alignment (in extreme case, placed orthogonally), creates a template for the grown cardiomyocyte tissue with two parts where the cells are aligned in different directions and exhibit different anisotropy of the excitation propagation. The propagating front of excitation was observed by tracking fluorescent probes, i.e. optical mapping [19]. It was found that the border between two alignment zones serves as a perturbing feature for the excitation propagation, the more perturbing as the higher degree of misalignment was set. In general, the perturbation of the propagating wave front was either delay, or acceleration at the border, depending on the direction of the propagation. The progressing delay may lead to the conduction block and the re-entry (rotating wave) origination.

Materials and methods

1.2.1 Preparation of solid substrate with designed surface topography

Materials

An electrospinning ready solution of polymethylglutarimide (PMGI, viscosity 339 cst at 25 C) having a concentration of 13% being dissolved in a mixture of cyclopentanone and tetrahydrofurfuryl alcohols (9:1) was purchased from MICROCHEM Corp. (MA, USA). The ionic surfactant sodium dodecyl sulfate (SDS, obtained from Wako Chemicals Inc., Japan) dissolved in ethanol was admixed into the polymer solution to a final concentration of 1.44 g/L, to prevent beading and obtain smooth fibers during electrospinning.

Polydimethylsiloxane (PDMS) was prepared by the thorough mixing of two liquid components (purchased from Dow Corning Toray Corp., Japan) at a ratio of 1:10 in a flat Petri dish. After being kept at 80°C for 1 hour, the polymerized PDMS layer was separated from the dish, cut into 20 × 20 mm squares and cleaned with ethanol before use. The PDMS squares were used as temporary holders with PMGI nanofibers for preparation of glass cover slips

micro-imprinted with nanofibrous pattern.

All other chemicals were purchased from Wako Chemicals Inc., Japan.

Electrospinning of PMGI nanofibers

The prepared solution of PMGI polymer with SDS was electrospun using a high voltage power supply (Matsusada Precision Inc., Japan) with an 8 kV potential between the solution and the grounded collector. The solution was loaded into a 1 ml syringe and delivered through a 27 gauge blunt-tip needle at a flow rate of 0.8 mL/h using a programmable syringe pump (Fusion 100, Chemyx Inc., Japan). Fibers were deposited onto a grounded stationary collector at a distance of 10 cm from the syringe tip. The collector was round in shape (5 cm in diameter), made of 0.01 mm thick aluminium foil. The alignment of the nanofibers was ensured by the presence of a rectangular hole in the middle of the collector. The size of the hole was 20 mm in width and 25 mm in height. In compliance with the desired positioning density of the nanofibers as 50 fibers/mm spraying time was set to 1 minute.

Preparation of solid substrate with nanofibrous surface topography

Our primary task was to create nanofibrous pattern on the surface of the solid substrate (glass cover slips) in order to prepare anisotropic cardiac tissue cultures with abrupt change in cardiac fiber orientation by 90°. For this purpose collected PMGI nanofibers were transferred onto the above-mentioned PDMS square holders in two steps. At first collected nanofibers from the hole were transferred to PDMS square, than half of these fibers were orthogonally cut and removed from the PDMS. After that procedure was repeated prepared samples were stored for 24 hours to remove the solvent residues.

For our study was necessary to prepare substrates with the sharp changing of fiber direction (90 degrees). For the first step we prepared 10 mm long fibers and transferred them onto PDMS, and then we gently cut a half of the fibers in the orthogonal direction. For the second step we prepared 20 mm long fibers and transferred them onto the cleaned side of PDMS orthogonally to fibers which were transferred before (see Figure 1.1a). For cell seeding and cultivation, the electrospun PMGI nanofibers were transferred from the PDMS

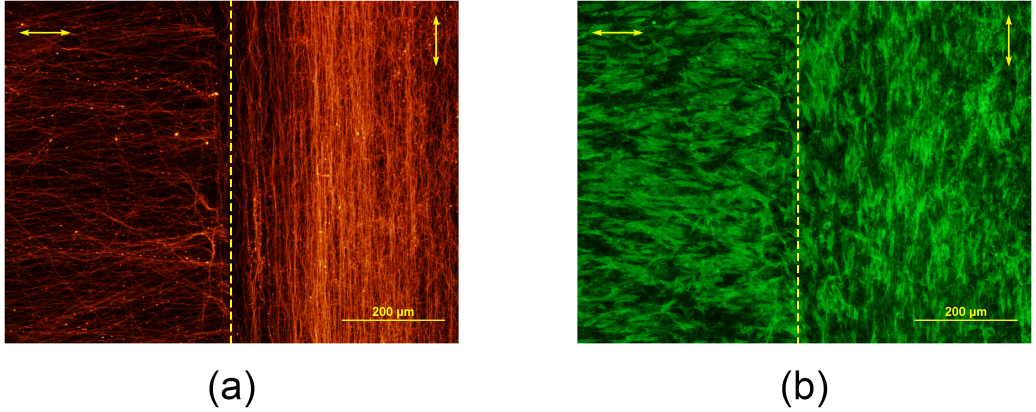


Figure 1.1: Cardiac tissue grown in two adjacent areas of nanofibers with orthogonal orientation. (a) Nanofibers stained with Rhodamine. (b) Actin staining of the cells grown on nanofibers.

onto 22 mm glass cover slips by micro-contact printing to fasten the fibers to a smooth glassy surface. After all, surface with fibers was coated with fibronectin (0.16 mg/ml) for better cell adherence.

For the studies of unidirectional block we have cut the samples and divided into narrow stripes (3-4 mm width) for better wave collimation. Cuts were made in perpendicular to the border direction using a sharp razor. Thus, we obtained several narrow specimens with short uniform borders instead of large one with long non-uniform border.

We have also added lidocaine to suppress spontaneous activity and to raise the threshold in order to make an effect more pronounced [20]. Lidocaine was diluted in Tyrode solution to 180-200 μ M concentration.

1.2.2 Cells

Cardiac cell isolation, seeding and cultivation performed according to Worthington protocol¹. Cardiac cells were isolated from the ventricles of 1-3 day old neonatal Wistar rats (SLC Inc., Japan).

All procedures were performed according to the institutional requirements for the care and use of laboratory animals. All studies conformed to the

¹<http://www.worthington-biochem.com/NCIS/default.html>

Guide for the Care and Use of Laboratory Animals, published by the United States National Institutes of Health (Publication No. 85-23, revised 1996) and approved by MIPT Life Science Center Provisional Animal Care and Research Procedures Committee, Protocol #A2-2012-09-02.

1.2.3 α -actin staining

α -actin staining of cells attached to nanofibers was performed as described at [18].

1.2.4 Optical mapping

Optical mapping was done in 5-6 day-old cell culture samples that were grown on glass cover slips covered with PMGI nanofibers. To monitor activity and visualize the excitation wave propagation, the cells were loaded with the Ca^{2+} sensitive indicator Fluo-4-AM (Invitrogen, USA) in Tyrode solution at room temperature. After staining (40 minutes), the medium was exchanged with fresh Tyrode solution (Sigma-Aldrich Co., USA) and kept at room temperature during the observations. The excitation waves were monitored using a high-speed imaging setup (an Olympus MVX-10 Microscope equipped with EM-CCD camera, Andor iXon3). Images were acquired at 250 fps. Cathodal point stimuli (1.5-1.7 threshold, 20 ms duration) were applied at a rate of 1-1.5 Hz using the tip of a 500 μm platinum wire placed about 0.5 mm above the surface at two different locations sequentially – over longitudinal and over transversal fibers, far from the border between these areas and near the dish wall. Looped platinum wire return electrode was placed along the dish wall about 10 mm away from the cover slip. Therefore, we stimulated wave series passing from the longitudinal fibers to the transversal fibers, and then replaced the electrode to stimulate the wave series on the same sample in the opposite direction.

The recorded movies were analyzed using ImageJ Software (NIH, Maryland, USA, <http://rsb.info.nih.gov/ij>). Time-space plots were created from the recorded movies along a scan line placed orthogonal to the edge of change in fiber direction. Spatial resolution of optical mapping was $75 \times 75 \mu\text{m}$ per pixel.

1.2.5 Computer modeling

In order to consider the source-sink mismatch effect, we use a generic FitzHugh-Nagumo model [21, 22]:

$$\frac{\partial u(\vec{x}, t)}{\partial t} = \nabla(D(\vec{x})\nabla u) + u(1 - u)(u - a) - v, \quad (1.1)$$

$$\frac{\partial v(\vec{x}, t)}{\partial t} = \epsilon(\beta u - \gamma v - \delta), \quad (1.2)$$

where a is the excitation threshold, which value varies between 5% and 20% in our study, $D(\vec{x})$ is a coupling coefficient related to space variables, $u(\vec{x}, t)$ is the normalized membrane potential and $v(\vec{x}, t)$ is a recovery variable. In the range of parameters that describes our experimental data, the inhibitor variable v could be neglected in detailed studies of the delay as its value is always much less than the duration of an action potential, so that the back wavefront is distanced from the area, where the effect takes place. The second equation is absolutely necessary for re-entry simulation. The parameter values used in this study are $a = 0.05 \pm 0.2$, $\beta = 0.5$, $\gamma = 1$, $\delta = 0$, $\epsilon = 0.01$, while tensor $D(\vec{x})$ is varied. No-flux boundary conditions were imposed:

$$\frac{\partial u(\vec{x}, t)}{\partial \vec{n}} = 0, \quad \vec{x} \in \Gamma, \quad t \in [0, T],$$

where Γ is a border of a considered set, \vec{n} – normal vector to the border Γ , and T is the total time of simulation.

Since we are interested in the velocity change only in orthogonal direction to the border, for the computer simulation we used quasi one-dimensional model. Also, since the cells in the different areas of the tissue culture are the same and vary only by the direction of alignment, the kinetics of action potential in computer simulation must be the same on both sides of the boundary. The only parameter which can be changed in order to simulate the acceleration or deceleration transition of the excitation wave is the diffusion tensor (or, coupling coefficient between cells in a more broad sense). According to experimental data, propagation along the fibers relates to higher coupling coefficient than across them.

Table 1.1: Parameters used in simulations.

Description	Variable	Value
Space interval	$[0, L]$	$[0, 30 - 240]$
Border coordinate	x_c	20
Diffusion coefficient	D_1	0.5
Anisotropy ratio (AR)	$\log D_2/D_1$	$[-3, 3]$
Space step	h	0.05
Time step	t	10^{-4}
Total simulation time	T	150, 250

We assume the edge, where cells are changing their direction, much more narrow than the characteristic dimension of the excitation wave. Indeed, the transversal propagation speed is approximately 10 cm/s, typical size of cardiomyocytes in this direction is 10 μm and duration of the rising phase of action potential is about 2 ms. Hence, there are about 20 cells, involved in rising phase, which is more than 5-10 cells on the edge (see Figure 1.1b).

Therefore, we approximated $D(x)$ with a Heaviside function:

$$D(x) = \theta(x - x_c)(D_2 - D_1) + D_1,$$

where x_c is a coordinate of the border, and solving equations with constant D_1 and D_2 in two areas, connected through the current flow conservation equation:

$$J_1 = D_1 \left. \frac{\partial u}{\partial x} \right|_{x=x_c-0} = D_2 \left. \frac{\partial u}{\partial x} \right|_{x=x_c+0} = J_2.$$

The coordinates of the border, the diffusion coefficient in the first area and the excitation threshold were fixed during computations with various coupling coefficients D_2 , so that the excitation wave in the area before the border forms a stable traveling pulse that could be used as an initial condition for further simulations with the same parameters, except the coupling coefficient after the border.

Space interval was optimized for every combination of D_2 and a , to minimize computation time. The size of the simulated tissue before the border (x_c) was minimal, but enough to form a stable travelling pulse. We accounted from 5% to 20%, and D_2 from $1/20D_1$ to $20D_1$. The FitzHugh-Nagumo model use dimensionless variables, but the voltage may be mapped onto physiological

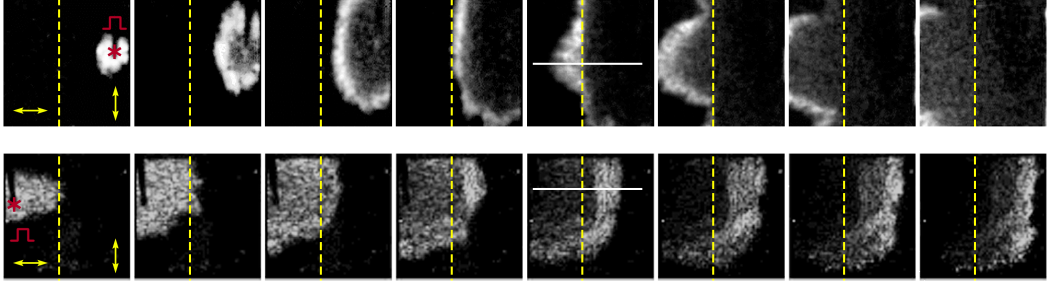


Figure 1.2: The camera report obtained from the experiment. Stimuli were applied in a region of transversal fibers (a) and produced a wave with elliptical front, and in a region of longitudinal fibers (b). White segments were used for time-space plot creation.

interval (-80 mV, 20 mV) using linear scaling [23]. In this case, the threshold was varied between -75 mV and -60 mV. For all computations explicit Euler schemes were used with time step equal to 10^{-4} and space step equal to 0.05 . All parameter values used in the simulations are represented in Table 1.1.

After computation of a transmembrane potential, an integral of the potential overall considering intervals was calculated. During propagation of the progressing wave in an area with constant coupling coefficient, the integral is growing linearly. When the wave reaches the edge, integral is equal to I_c – amplitude of action potential (1 in our computation), multiplied with x_c (coordinate of the edge). After that we extrapolated linear parts of the plot and measured the distance between points of intersection with I_c , like we did for all experimental data (see Section 1.3.7 and Figure 1.3a and 1.3b). Measuring the delay using the dynamics of the integral is more precise than finding the velocity of any phase of the wave, because the interpolation of the wave front is needed for the front detection.

1.2.6 Re-entry simulation

Let the preferential direction orientation of the diffusion tensor be a function of space variables, like:

$$\varphi = \frac{\pi}{2} S \left(\frac{x - x_c}{\alpha + S((y - y_c)/\beta)} \right),$$

where $\alpha = 0.01$, $\beta = 0.2$, $x_c = 0.5$, $y_c = 1.5$ and $x \in [0, 2]$, $y \in [0, 2]$ and $S(t) = (1 + \exp(-t))^{-1}$ is a sigmoid function. In this case, the border zone, where fibers are changing their direction, is wider for bigger values of y . The stimulation was applied in $x = 0$. The anisotropy ratio in terms of velocities (V_2/V_1) was equal to 4.5 and the threshold a was 15%, that corresponds to -65 mV [23].

Results

1.3.7 Experimental results

The samples for the study of excitation propagation across the boundary between the areas with different direction of cell alignment were prepared by imprinting aligned PMGI nanofibers separately to left and right parts of the glass substrate in perpendicular directions (T-shaped array shown in Figure 1.1a), and seeding cardiac cells on them. In each part of the sample the cells aligned in the direction of the fibers and fluorescent microscopy of stained α -actin filaments showed a high level of cell ordering along the fiber directions (Figures 1.1a, 1.1b). Only tissue cultures in which high level of structural anisotropy was obtained were used further to study the excitation propagation. It was also checked that the boundary zone between two areas of alignment did not show any discontinuity, observed by the phase contrast microscopy.

We have measured the position of the wave front using calcium upstroke, which follows the transmembrane potential upstroke with the delay of 5.3 ± 1 ms [24]. This delay should not depend on fiber orientation. Figure 1.2 shows propagation of excitation across the border zone. The stimulating electrode was placed to the right from the border between areas of alignment. Since excitation wave accelerates in the direction of alignment [18] the front shape was elliptical, extended in the vertical direction. When wave crossed the border the wave accelerated in the horizontal direction and the front shape changed accordingly.

The more detailed study of the wave propagation in the border zone reveals the fact that it did not exhibit just a switch in the propagation speed. Depending on the transition between the zones direction, the wave approaching the

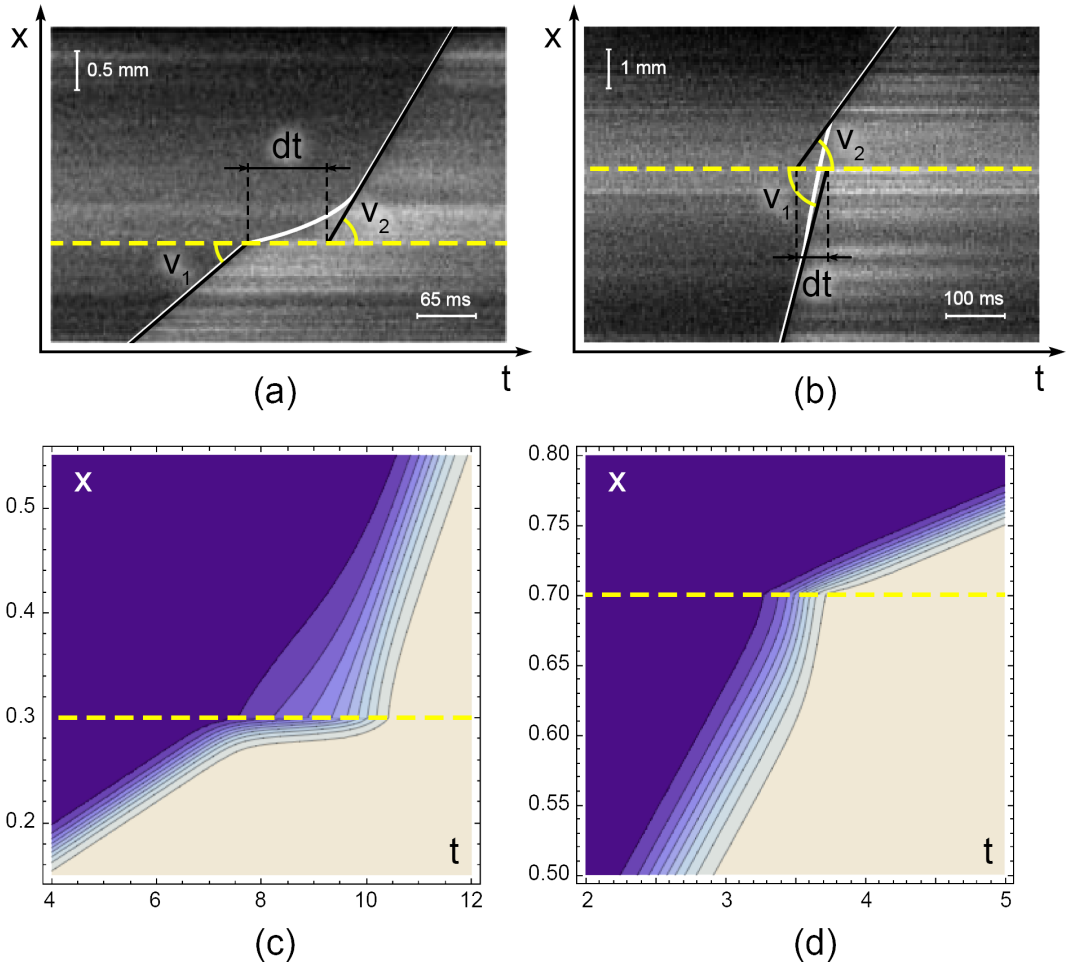


Figure 1.3: Border-induced perturbation of the wave propagation. Experimental time-space plots (a), (b) for one sample stimulated from the opposite sides, and corresponding simulations (c), (d). The origin of coordinates was placed in a stimulation point. Additional lines illustrate measurements of a delay (a) or a leap (b) and a ratio of the velocities. Black lines show the edge and two asymptotes to the wave front before and after the border, where angles from the horizontal axis correspond to the velocities and the distance on the border constrained by the asymptotes is equal to the absolute value of a delay or a leap. In the area just before the border (≈ 0.5 mm) the wave propagates much slower (a), (c) or accelerates (b), (d), depending on the direction of propagation. Figures (c) and (d) show the time-space plots, obtained from computer simulations using FitzHugh-Nagumo equations.

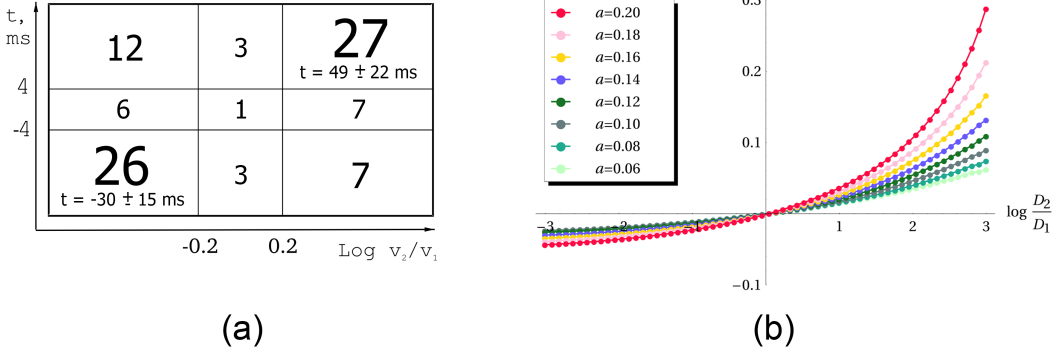


Figure 1.4: Results for the delay in relation to the anisotropy ratio, obtained from experiment (a) and from simulation (b). Experimental data, gathered from a large amount of the samples with various anisotropy ratios, was arranged into a table (a) by separation of definitely positive, approximately zero and definitely negative values. Horizontal axis corresponds to the anisotropy ratio, vertical axis – to the magnitude of the delay. Leaps are considered to be negative values of the delay. Simulation results (b) cover approximately the same range of the anisotropy ratios that was observed in experiment. Time is represented in arbitrary units.

border showed either delay or leap in propagation. Counterintuitively, it delayed before acceleration and leaped before the deceleration [25]. Details of the wave propagation across the border were analyzed with the aid of time-space plots build along the scan line perpendicular to the border. Figure 1.3 shows typical time-space plots build along a line x crossing the boundary between two zones of alignment. While far from the border in both parts wave propagates with constant speed which results in a straight line in time-space plot ($v = dx/dt$), in the border zone the wave velocity undergoes the non-monotonic transition. Thus, while passing from the part with slower propagation to the part with faster propagation, wave slows down before the acceleration, Figure 1.3a, and accelerates in the opposite transition, Figure 1.3b. By continuing straight lines corresponding to the constant speed propagation until crossing the border, it is possible to measure dt : the corresponding delay (Figure 1.3a) or the corresponding leap (Figure 1.3b).

The time shift dt , either negative or positive, appeared larger when a larger change in the wave speed occurs. However, the variability of the experimental

data did not allow us to reasonably plot this dependence, but we have counted all experiments with various propagation directions, in which delay or leap occurred (Figure 1.4a). We have divided the data into groups by anisotropy ratio and by the effect observed: a delay, an insignificant effect or a leap. Therefore, we have 27 evidences of the delay, 26 – of the leap and also $12 + 7 = 19$ negative results corresponding to inhomogeneities in the tissue, curvature effects and other methodological problems, that we were striving to avoid. The raw data, obtained from 92 samples is presented in the [26], Appendix A.

We have conducted Fisher's exact test with the data in the table in Fig. 1.4a to disprove the null hypothesis that leap or delay occurs independently from the direction of propagation:

$$p = \frac{\binom{12 + 27}{12} \binom{26 + 7}{26}}{\binom{12 + 27 + 26 + 7}{12 + 26}} = 4.2 \times 10^{-5},$$

which refers to extremely unlikely case.

Moreover, one of our samples has shown conduction block instead of a delay for every third wave in a sequence (see Figure 1.5). In this particular experiment, first wave propagates with a relatively small delay, next one with a much longer delay, and third one dies out after the edge. The impact of a previous wave refractory zone on the next wave can also be seen in a first area only: the velocity of every consequent wave in a series slightly decreases.

It should be noted that the lengthy border between areas with different cell orientation may have slightly dissimilar regions, which makes it more difficult to accurately determine the conduction block, occurring in some regions while not in others. Therefore, we've changed the proportions of the samples for better collimation and avoidance of the curvature effects. In such narrow samples unidirectional conduction block was observed in 8 of 12. Usually, we observed the blockage of every second or every third wave in a sequence.

As it was discussed in Section 1.2.5, the problem can be considered as one dimensional, where the only coupling coefficient differs. In this representation the conduction block and its dependence on a frequency of stimulations was already studied by C. Zemlin and A. Pertsov [27]. Unidirectional conduction

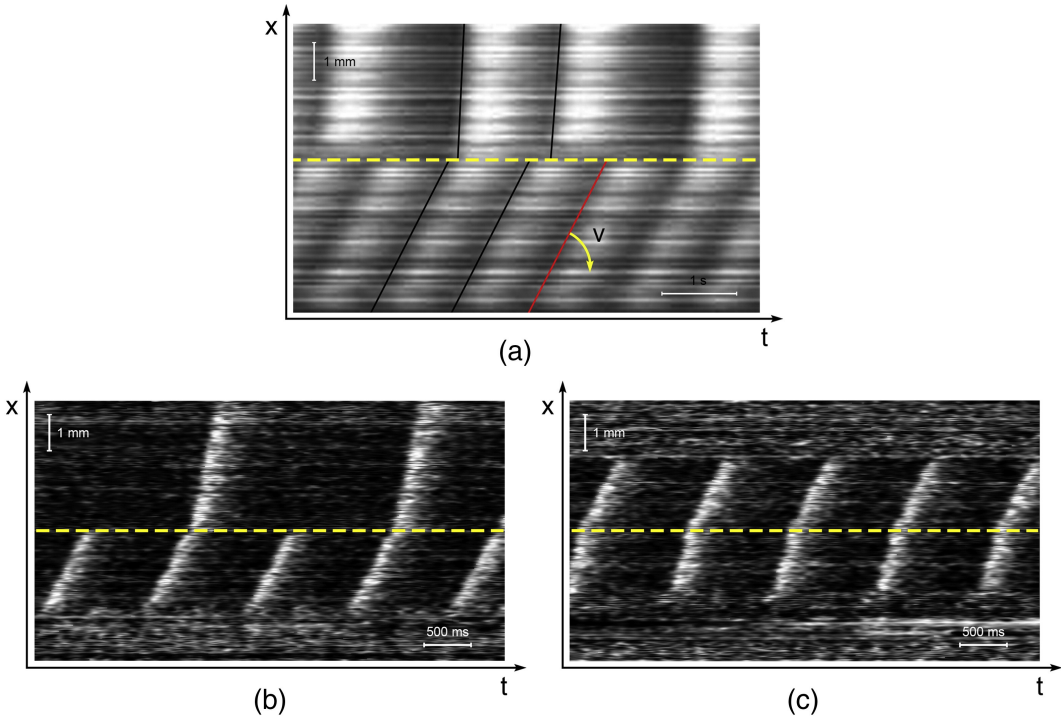


Figure 1.5: Block of conduction for every third (a) or second (b–c) excitation wave in a sequence. Images (b) and (c) show propagation through the border in the same sample in two opposite directions.

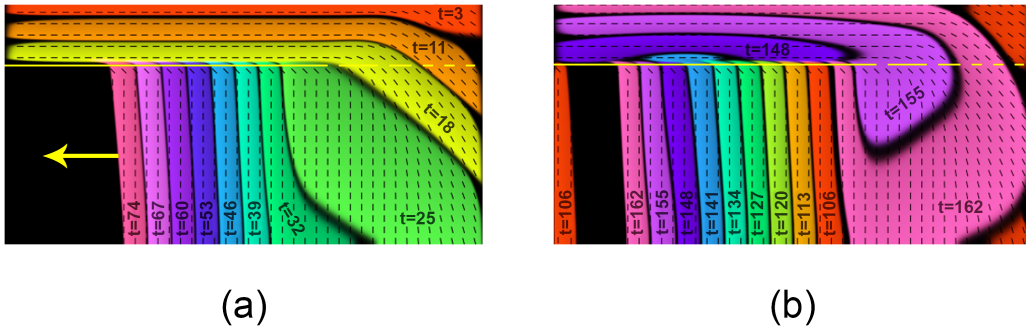


Figure 1.6: The scenario of re-entry formation (a) and further spiral wave rotation (b). The left side of the border has a sharp fiber direction change, whilst the right side has a wide area with gradual orientation change.

block in a heart leads to a symmetry breaking in excitation propagation and may give a rise to a rotating wave (re-entry) and result in fibrillation.

1.3.8 Re-entry simulation

We provide a simulation of a re-entry formation scenario on the sample, described in Section 1.2.6. The stimulation was applied in that half of the sample, where fibers are parallel to the border, so the one-directional conduction block occurred in the narrow border zone and broke the symmetry in wave propagation. Consequently, the excitation wave reaches the area of longitudinal fiber direction through the wide border zone, and continues to propagate along the border, until the transversal area, where the stimulation was applied, stays in the refractory state (see Figure 1.6a). After the refractory period ends, the excitation wave crosses the border in the narrow border zone, but only in longitudinal-transversal direction. One period of the spiral wave is shown in figure 6b.

1.3.9 Computer simulations

Figure 1.2 represents a comparison of the time-space plots for one sample stimulated from the opposite sides obtained from the experiment (Figures 1.2a and 1.2b) and from the computer simulation (Figures 1.2c and 1.2d). Wave approaching the border slowed down, if propagated from the side with lower diffusion coefficient (across the fibers) and accelerated propagating in opposite direction (along the fibers). The effect becomes more pronounced when the ratio of diffusion coefficients rises (Figure 1.4b).

In terms of activating and inhibiting variables dynamics in FitzHugh-Nagumo equations, the acceleration during the transition from longitudinal to transversal areas belongs to accumulation of an activator, and deceleration in an opposite direction — to an excessive flow through the boundary. Therefore, the wave undergoes non-monotonous velocity change in a boundary zone.

The dependence of the delay on the ratio of coupling coefficients is shown in the Figure 1.4b. Positive value of dt corresponds to the delay caused by the source mismatch and negative — to the leap caused by sink mismatch. It appears, that the value of the delay is bigger than the value of the leap,

occurred on the same sample during propagation in the opposite direction, and this difference increases with the rise of the anisotropy ratio. It leads us to the hypothesis, that the presence of the borders in a tissue is resulted in retarding effect in general.

Discussion

The anisotropic structure of the heart is important for understanding of both normal propagation and arrhythmogenic one, since it produces the conduction heterogeneity and may lead to the source-sink mismatch, slow conduction up to the conduction block, and, finally, the formation of the reentry. There are a number of conduction block formation scenarios caused by tissue structure, and three the most frequently studied [28] are: a simple linear connective tissue structure with the sharp end, that creates a pivot point for a turning wavefront [29–32]; a small “gate” connected to a large excitable area with the same conduction properties [10, 15, 16, 33], and abrupt change of tissue geometry [15, 25, 34–36]. In addition, the conduction asymmetry in the scenarios above can be enhanced by application of the external stimuli with relatively high frequency [37]. In this case the excitation front interacts with the repolarization phase (tail) of a preceding wave and unidirectional block can develop [38–40].

All these scenarios have similar underlying fundamental biophysical laws, including two-dimensional curvature effects, whereas in this article we consider a quasi-one dimensional phenomenon, based on a source-sink mismatch in the initial subthreshold phase. We did not add any unexcitable regions deliberately and set high requirements to the cell culture homogeneity in order to obtain entirely excitable samples with uniform electric properties. Thus, we were able to observe a distinct effect, caused by an abrupt change of the fiber direction, different from branching and “gate” effects, caused by the presence of unexcitable obstacles in the two dimensional tissue. However, the curvature of the wavefront, stimulated with the point-stimulation electrode, may also play a minor role in the studied effect and add bias error. Therefore, we have added collimation into the samples to minimize curvature effects.

We considered only the border between orthogonal fiber directions as the

extreme and the most pronounced case, whereas the delay dependence on the angle between fiber directions lies beyond this study. We have proposed a scenario of a reentry formation *in silico*, but the duplication of the same fiber orientation *in vitro* is complicated. However, we have shown a one-direction block for every second or third wave, which is enough for symmetry breaking and reentry formation, according to our theoretical studies.

The simulations employing FitzHugh-Nagumo model reproduce the delay, the leap and the uni-directional block qualitatively, however the parameters, used in simulations, can not be adjusted to the experiments quantitatively. Nevertheless, both experimental samples and computer simulations show, that the delay is always longer than acceleration in opposite direction.

Conclusions

Our study shows that the wave speed undergoes non-monotonic change in transition between the two areas of alignment and the wave propagation may delay up to the complete conduction block. In terms of the corresponding cardiac tissue, it may mean that the abrupt change in the direction of tissue fibers may serve as the source of the wave-breaks, i.e. play the arrhythmogenic role. Moreover, the presence of multiple domains with the edges where fiber directions in the tissue sharply change leads to the overall slower propagation of excitation waves, since in transition through the border between domains the delay is always more significant than the acceleration.

Computer simulations employed very generic FitzHugh-Nagumo model and the effect of misalignment was simulated by the difference in diffusion coefficients. The simulations allowed us to prove that the effect observed experimentally is a generic one and may be explained in terms of general features of excitation propagation. We have also proposed one of the possible scenarios of re-entry formation.

Acknowledgements

We would like to thank Dr. Arkady Pertsov for useful discussions. The research was partially supported by Federal “5top100” Program.

Disclosures

None

References

- [1] R. E. Horch, U. Kneser, E. Polykandriotis, *et al.*, “Tissue engineering and regenerative medicine—where do we stand?,” *Journal of Cellular and Molecular Medicine*, vol. 16, pp. 1157–1165, 2012.
- [2] K. Miki, H. Uenaka, A. Saito, *et al.*, “Bioengineered myocardium derived from induced pluripotent stem cells improves cardiac function and attenuates cardiac remodeling following chronic myocardial infarction in rats,” *Stem Cells Translational Medicine*, vol. 1, no. 5, pp. 430–437, 2012.
- [3] C. V. C. Bouten, P. Y. W. Dankers, A. Driessen-Mol, *et al.*, “Substrates for cardiovascular tissue engineering,” *Advanced drug delivery reviews*, vol. 63, no. 4, pp. 221–241, 2011.
- [4] T. Eschenhagen, C. Fink, U. Remmers, *et al.*, “Three-dimensional reconstitution of embryonic cardiomyocytes in a collagen matrix: a new heart muscle model system,” *The FASEB Journal*, vol. 11, no. 8, pp. 683–694, 1997.
- [5] C. Williams, Y. Tsuda, B. C. Isenberg, *et al.*, “Aligned cell sheets grown on thermo-responsive substrates with microcontact printed protein patterns,” *Advanced Materials*, vol. 21, no. 21, pp. 2161–2164, 2009.
- [6] N. Bursac, “Cardiomyocyte Cultures With Controlled Macroscopic Anisotropy: A Model for Functional Electrophysiological Studies of Cardiac Muscle,” *Circulation Research*, vol. 91, pp. 45e–54, 2002.
- [7] D. Kai, M. P. Prabhakaran, G. Jin, and S. Ramakrishna, “Guided orientation of cardiomyocytes on electrospun aligned nanofibers for cardiac tissue engineering,” *Journal of biomedical materials research. Part B, Applied biomaterials*, vol. 98B, pp. 379–86, 2011.
- [8] M. P. Prabhakaran, D. Kai, L. Ghasemi-Mobarakeh, and S. Ramakrishna, “Electrospun biocomposite nanofibrous patch for cardiac tissue engineering,” *Biomedical Materials*, vol. 6, no. 5, p. 55001, 2011.
- [9] Z. Li, X. Guo, A. F. Palmer, H. Das, and J. Guan, “High-efficiency matrix modulus-induced cardiac differentiation of human mesenchymal stem cells inside

- a thermosensitive hydrogel,” *Acta biomaterialia*, vol. 8, no. 10, pp. 3586–3595, 2012.
- [10] C. Cabo, A. M. Pertsov, W. T. Baxter, *et al.*, “Wave-front curvature as a cause of slow conduction and block in isolated cardiac muscle,” *Circulation research*, vol. 75, pp. 1014–28, 1994.
- [11] K. Agladze, J. Keener, S. Müller, and A. Panfilov, “Rotating Spiral Waves Created by Geometry,” *Science*, 1994.
- [12] S. Kadota, M. W. Kay, N. Magome, and K. Agladze, “Curvature-dependent excitation propagation in cultured cardiac tissue,” *JETP letters*, vol. 94, no. 11, pp. 824–830, 2012.
- [13] F. J. Vetter, S. B. Simons, S. Mironov, C. J. Hyatt, and A. M. Pertsov, “Epicardial fiber organization in swine right ventricle and its impact on propagation,” *Circulation research*, vol. 96, pp. 244–51, 2005.
- [14] S. Y. Ho, R. H. Anderson, and D. Sánchez-Quintana, “Atrial structure and fibres: morphologic bases of atrial conduction,” *Cardiovascular research*, vol. 54, no. 2, pp. 325–336, 2002.
- [15] V. G. Fast and A. G. Kléber, “Cardiac tissue geometry as a determinant of unidirectional conduction block: assessment of microscopic excitation spread by optical mapping in patterned cell cultures and in a computer model,” *Cardiovascular research*, vol. 29, pp. 697–707, 1995.
- [16] M. S. Spach, W. T. Miller, P. C. Dolber, *et al.*, “The functional role of structural complexities in the propagation of depolarization in the atrium of the dog. Cardiac conduction disturbances due to discontinuities of effective axial resistivity,” *Circulation Research*, vol. 50, no. 2, pp. 175–191, 1982.
- [17] N. Bursac, Y. Loo, K. Leong, and L. Tung, “Novel anisotropic engineered cardiac tissues: studies of electrical propagation,” *Biochemical and biophysical research communications*, vol. 361, pp. 847–53, 2007.
- [18] Y. Orlova, N. Magome, L. Liu, Y. Chen, and K. Agladze, “Electrospun nanofibers as a tool for architecture control in engineered cardiac tissue,” *Biomaterials*, vol. 32, pp. 5615–24, 2011.
- [19] K. Agladze, M. W. Kay, V. Krinsky, and N. Sarvazyan, “Interaction between spiral and paced waves in cardiac tissue,” *American Journal of Physiology-Heart and Circulatory Physiology*, vol. 293, no. 1, pp. H503–H513, 2007.
- [20] A. Isomura, M. Hörning, K. Agladze, and K. Yoshikawa, “Eliminating spiral

- waves pinned to an anatomical obstacle in cardiac myocytes by high-frequency stimuli,” *Physical Review E*, vol. 78, no. 6, p. 66216, 2008.
- [21] R. FitzHugh, “Impulses and Physiological States in Theoretical Models of Nerve Membrane,” *Biophysical Journal*, vol. 1, pp. 445–466, 1961.
- [22] J. Nagumo, S. Arimoto, and S. Yoshizawa, “An active pulse transmission line simulating nerve axon,” *Proceedings of the IRE*, vol. 117, no. m V, pp. 2061–2070, 1962.
- [23] R. R. Aliev and A. V. Panfilov, “A simple two-variable model of cardiac excitation,” *Chaos, Solitons & Fractals*, vol. 7, pp. 293–301, 1996.
- [24] V. G. Fast and R. E. Ideker, “Simultaneous optical mapping of transmembrane potential and intracellular calcium in myocyte cultures,” *Journal of cardiovascular electrophysiology*, vol. 11, no. 5, pp. 547–556, 2000.
- [25] Y. Wang and Y. Rudy, “Action potential propagation in inhomogeneous cardiac tissue: safety factor considerations and ionic mechanism.,” *American journal of physiology. Heart and circulatory physiology*, vol. 278, pp. H1019–29, 2000.
- [26] N. Kudryashova, A. Teplenin, Y. Orlova, L. Selina, and K. Agladze, “Arrhythmogenic role of the border between two areas of cardiac cells alignment,” *Journal of Molecular and Cellular Cardiology*, 2014.
- [27] C. W. Zemlin and A. M. Pertsov, “Bradycardic onset of spiral wave re-entry: structural substrates,” *Europace*, vol. 9, no. suppl_6, pp. vi59–vi63, 2007.
- [28] A. G. Kléber and Y. Rudy, “Basic mechanisms of cardiac impulse propagation and associated arrhythmias.,” *Physiological reviews*, vol. 84, pp. 431–88, 2004.
- [29] S. M. Dillon, M. A. Allesie, P. C. Ursell, and A. L. Wit, “Influences of anisotropic tissue structure on reentrant circuits in the epicardial border zone of subacute canine infarcts.,” *Circulation research*, vol. 63, pp. 182–206, 1988.
- [30] M. J. Schaliij, *Anisotropic conduction and ventricular tachycardia*. PhD thesis, Maastricht university, 1988.
- [31] M. J. Schaliij, W. J. Lammers, P. L. Rensma, and M. A. Allesie, “Anisotropic conduction and reentry in perfused epicardium of rabbit left ventricle.,” *The American journal of physiology*, vol. 263, pp. H1466–78, 1992.
- [32] A. Wit, S. Dillon, and J. Coromilas, “Anisotropic reentry as a cause of ventricular tachyarrhythmias in myocardial infarction.,” *Cardiac Electrophysiology: From Cell to Bedside*, pp. 511–526, 1995.
- [33] C. Cabo, A. M. Pertsov, J. M. Davidenko, *et al.*, “Vortex shedding as a precursor

- of turbulent electrical activity in cardiac muscle.,” *Biophysical journal*, vol. 70, pp. 1105–11, 1996.
- [34] V. G. Fast and A. G. Kléber, “Block of impulse propagation at an abrupt tissue expansion: evaluation of the critical strand diameter in 2- and 3-dimensional computer models.,” *Cardiovascular research*, vol. 30, pp. 449–59, 1995.
- [35] S. Rohr and B. M. Salzberg, “Characterization of impulse propagation at the microscopic level across geometrically defined expansions of excitable tissue: multiple site optical recording of transmembrane voltage (MSORTV) in patterned growth heart cell cultures.,” *The Journal of general physiology*, vol. 104, pp. 287–309, 1994.
- [36] S. Rohr and B. M. Salzberg, “Multiple site optical recording of transmembrane voltage (MSORTV) in patterned growth heart cell cultures: assessing electrical behavior, with microsecond resolution, on a cellular and subcellular scale.,” *Biophysical journal*, vol. 67, pp. 1301–15, 1994.
- [37] C. de Diego, F. Chen, Y. Xie, *et al.*, “Anisotropic conduction block and reentry in neonatal rat ventricular myocyte monolayers.,” *American journal of physiology. Heart and circulatory physiology*, vol. 300, pp. H271–8, 2011.
- [38] W. Quan and Y. Rudy, “Unidirectional block and reentry of cardiac excitation: a model study.,” *Circulation research*, vol. 66, pp. 367–82, 1990.
- [39] R. M. Shaw and Y. Rudy, “The vulnerable window for unidirectional block in cardiac tissue: characterization and dependence on membrane excitability and intercellular coupling.,” *Journal of cardiovascular electrophysiology*, vol. 6, pp. 115–31, 1995.
- [40] C. F. Starmer, V. N. Biktashev, D. N. Romashko, *et al.*, “Vulnerability in an excitable medium: analytical and numerical studies of initiating unidirectional propagation.,” *Biophysical journal*, vol. 65, pp. 1775–87, 1993.

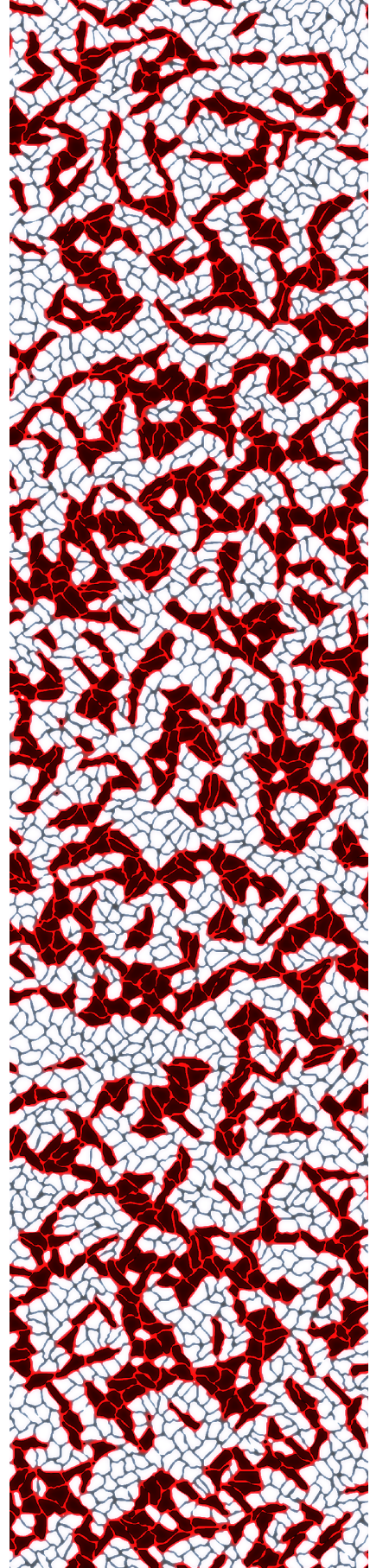
Chapter 2

Conditions for uni-directional block due to anisotropy in a model of human ventricular tissue

NN Kudryashova^{1,2}, IV Kazbanov¹, AV Panfilov^{1,2},
and K Agladze¹

¹Moscow Institute of Physics and Technology, Dolgoprudny, Russia

²Department of Physics and Astronomy, Ghent University, Ghent, Belgium



Abstract

Waveblock formation is the main cause of reentry. Here we perform a comprehensive numerical modeling study of block formation due to anisotropy in Ten Tusscher and Panfilov (2006) ionic model for human ventricular tissue. We consider a border between the areas of different myocardial fiber alignment and show that block can occur for a wave travelling from an area of transverse fiber direction to the longitudinal one. Such block occurs for reasonable values of the anisotropy ratio: from 2.4 to 6.2 with respect to the velocities of propagation. This critical anisotropy ratio decreases by suppression of I_{Na} , I_{Ca} , slightly decreases by suppression of I_{Kr} and I_{Ks} , and substantially increases by suppression of I_{K1} . Hyperkalemia affects the block formation in a complex bi-phasic way. We provide examples of reentry formation due to studied effects and conclude that suppression of I_{K1} should be the most effective way to prevent waveblock at the areas of abrupt change in anisotropy.

Keywords: uni-directional block, reentry, ten Tusscher-Panfilov model of human ventricular cardiomyocyte, hyperkalemia, channel blockers.

Published: Kudryashova, N.N., Kazbanov, I.V., Panfilov, A.V., & Agladze, K.I. (2015). Conditions for Waveblock Due to Anisotropy in a Model of Human Ventricular Tissue. *PLoS One*, 10(11), e0141832.

<http://doi.org/10.1371/journal.pone.0141832>.

Introduction

Cardiac arrhythmias are one of the largest cause of death in the industrialized world [1]. In most cases the lethal cardiac arrhythmias arise from abnormal wave propagation and are driven by reentrant sources of excitation, or vortices [1]. Such vortices occur as a result of blocks of wave propagation [2–4]. Thus, understanding the conditions of block formation is one of the central issues in theory of cardiac arrhythmias.

There are several mechanisms of waveblock formation. Historically, the first one was *S1S2* stimulations when a block occurred as a result of additional stimulation of the tissue at the tail of the propagating wave [5]. Later, two main classes of unaffected break formation mechanisms were identified. The first class deals with the wavebreaks which occur at the heterogeneity of cardiac tissue which can be due to the different properties of cardiac cells in different regions [6, 7] or due to dynamical instabilities [8–10]. The second class deals with geometrical heterogeneities, and the wavebreak can occur as a result of detachment of a wave from a boundary with a sharp end [11–13] or be formed around obstacles [14, 15]. Another widely studied geometrical structure is called “gate” or isthmus, where the waveblocks can be formed at the places of abrupt tissue expansion [16, 17].

In all cases involving the geometrical heterogeneity the wavebreak occur as a result of so-called current-to-load mismatch. The wave propagation is blocked as the density of the current produced by a wavefront at given region is not sufficient to initiate excitation in the adjacent tissue. In the cases listed above the current-to-load mismatch occurred either due to curvature of the wavefront, or as a result of the abrupt extension of the domain ahead of the wavefront. In all these cases the length of the wavefront abruptly increases, resulting in decrease in the current density and block of propagation.

There is also another possibility for the current-to-load mismatch: it occurs if the local resistivity of cardiac tissue changes. Indeed, if a wave propagates from a region with high resistivity to a region with low resistivity, the same current will produce a lower voltage gradient, making propagation of a wave through the boundary more difficult. Such change of resistivity naturally occurs due to tissue anisotropy. Indeed, change in anisotropy results in change

of the resistivity, meaning it can potentially result in a block of propagation. This was demonstrated in our previous study [18] in experiments in a cell culture of neonatal rat myocytes and numerically in a low dimensional model for cardiac tissue. Here we extend the theoretical study to a detailed ionic model of a human cardiac cells. We find the conditions for the waveblock formation, study, how the conditions depend on the conductivities of main ionic currents in cardiac tissue, and provide examples of formation of ectopic beats and reentry due to abrupt changes in anisotropy. We discuss possible importance of this effect to the onset of cardiac arrhythmias.

Materials and Methods

2.2.1 Electrophysiological model

We used ten Tusscher and Panfilov cell model (TP06) for human ventricular cardiomyocyte [19, 20]. In this model cardiac electrophysiology is described with the monodomain equation:

$$\frac{\partial V}{\partial t} = \nabla (\sigma(\vec{x}) \nabla V) - \frac{I_{ion}(V, \dots)}{C_m}, \quad (2.1)$$

$$\sigma(x < x_c) = \begin{pmatrix} \sigma_{\perp} & 0 \\ 0 & \sigma_{\parallel} \end{pmatrix}, \quad \sigma(x > x_c) = \begin{pmatrix} \sigma_{\parallel} & 0 \\ 0 & \sigma_{\perp} \end{pmatrix}, \quad (2.2)$$

where V is a transmembrane potential, σ is a tensor of coupling coefficients, x_c is a coordinate of the border and I_{ion} is a sum of ionic currents given by the following equation:

$$I_{ion} = I_{Na} + I_{K1} + I_{to} + I_{Kr} + I_{Ks} + I_{CaL} + I_{NaCa} + I_{NaK} + \\ + I_{pCa} + I_{pK} + I_{bCa} + I_{bNa}. \quad (2.3)$$

For the most of the parameters of the TP06 model describing the normal conditions we used values listed in Tables 1 and 2 of [20] corresponding to epicardial cells. We also decreased conductivity of the ionic channels to 75%, 50%, 25% percent of its normal value to study the effect of the channel blockers on the unidirectional block formation. To model hyperkalemia we varied $[K^+]_o$ from 5.4 mM to 20 mM.

2.2.2 Numerical methods

To solve the differential equations (2.1) in 2D (and 1D) we used an explicit Euler scheme:

$$\frac{V_{k+1}^{i,j} - V_k^{i,j}}{\tau} = \frac{1}{h^2} \left(J_{+\frac{1}{2},0} - J_{-\frac{1}{2},0} + J_{0,+\frac{1}{2}} - J_{0,-\frac{1}{2}} \right) - \frac{I_{ion}(V_k^{i,j}, \dots)}{C_m},$$

where the time step $\tau = 0.005$ ms, space step $h = 125$ μm and flow $J_{di,dj} = \sigma_{di,dj}^{i,j} (V_k^{i+di,j+dj} - V_k^{i,j})$. In 2D simulations we used ($\tau = 0.02$ ms, $h = 250$ μm), which within the widely accepted values for the ionic models [21]. We also checked important results of our paper in simulations with $\tau = 0.0008$ ms, $h = 50$ μm and showed that all results of our study on waveblock formation also hold for this spatial resolution.

We applied Neumann ('no flux', $J = 0$) boundary conditions in all simulations.

The model was implemented using C and CUDA programming languages. Results were obtained with NVIDIA Tesla K20 GPU.

2.2.3 Computational setup

We considered the extreme case of a border between two areas with orthogonal fiber alignment, shown in fig. 2.1. Fibers in one part was parallel to the border and in another part perpendicular to the border. Anisotropy ratio (AR) was assumed to be the same in the whole sample. Thus, this fiber orientation provides the greatest jump in velocity on the border, so the effects caused by this border would be the most pronounced.

First, we studied plane wave propagation across the border. In this case, the wave front is parallel to the border, and the whole system can be reduced to the one-dimensional case due to translational symmetry along the vertical y -axis (the solution does not depend on y).

Second, we returned to the two-dimensional representation to study non-symmetrical wave propagation, such as point stimulation and re-entry formation.

Both in 1D and 2D simulations the equations were first integrated with-

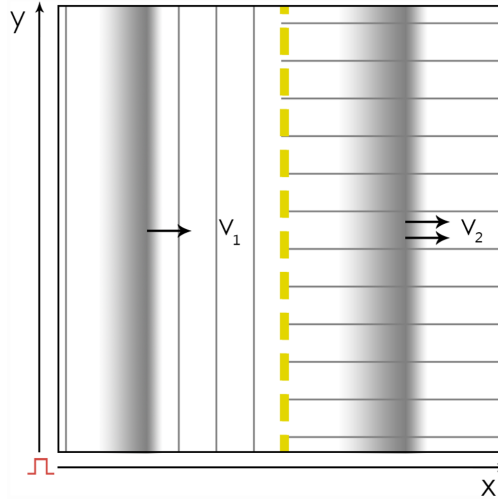


Figure 2.1: **Schematic representation of the computational setup in 2D** The tissue is divided into two parts with orthogonal fiber orientation. The boundary is shown by the yellow dashed line. In the left part the fibers (represented by thin lines) are parallel to the boundary, in the right part the fibers are orthogonal to the boundary. Two propagating waves are schematically shown as a greyscale images. Stimulation was applied at the left border. In that case wave propagation is translationally symmetric along the y axis and can be studied in 1D simulations.

out stimulation for 50 seconds in order to obtain spatially uniform steady state values which were saved and used further as the initial conditions for all simulations. In studies of periodic wave propagation we ignored the waves obtained by the first three stimulations to minimize possible effects of transient processes. Stimulation was applied in a rectangle 6 px width along the left border of the sample. In this rectangle transmembrane potential was immediately set to 50 mV.

The key parameter, that characterizes the probability of waveblock formation is the anisotropy ratio (AR) — the ratio of the velocities parallel and perpendicular to the fibers. It could be derived from coupling coefficients as follows:

$$AR = v_{\parallel}/v_{\perp} = \sqrt{\sigma_{\parallel}/\sigma_{\perp}}. \quad (2.4)$$

In simulations, where AR was varied, σ_{\parallel} was fixed and equal to $0.154 \text{ mm}^2/\text{ms}$ [19] and σ_{\perp} was set to $\sigma_{\parallel}/(AR \cdot AR)$.

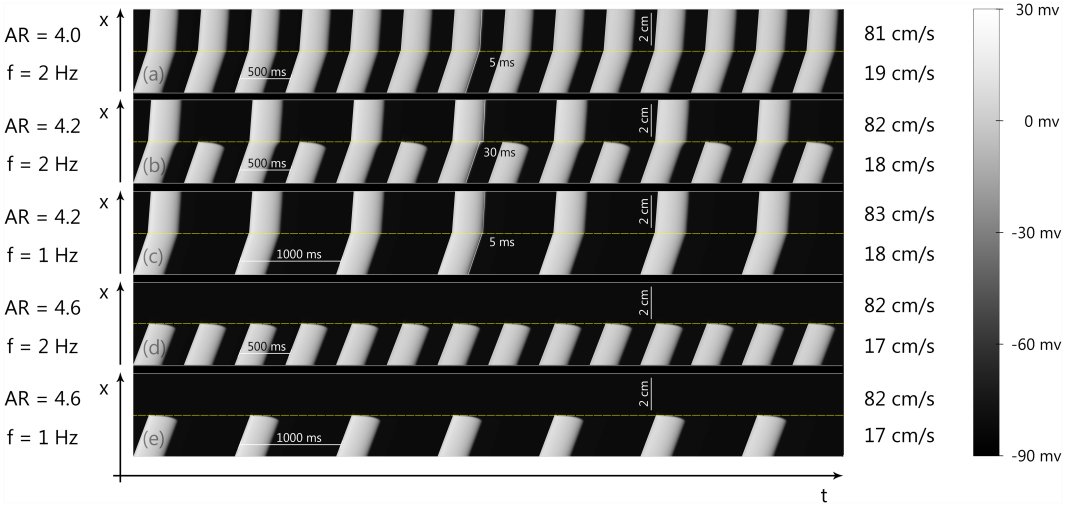


Figure 2.2: Wave propagation through the boundary of abrupt change of anisotropy in cardiac tissue for various anisotropy ratios (AR) and frequencies of stimulation (f). Figure shows space(x) – time(t) plots of wave propagation along 1D cable with abrupt change of conductivity, representing abrupt change of fiber directions in 2D cardiac tissue. The details of the computational setup are represented in Fig.1 and in section 2.2.3. (a,c) no block occurs (b) 1: 2 block, (d,e) complete block at the boundary.

Results

Figure 2.2 shows a typical process of wavebreak formation. We see that in case of relatively small anisotropy ($AR = 4.0$, see fig.2.2a) the wave passes through the boundary of heterogeneity with only a small delay at the border of an approximately 5 ms. However, if the anisotropy ratio is increased to $AR = 4.2$ (fig.2.2b), every second wave is blocked at the border, and those waves that pass are delayed for 30 ms. The decrease in stimulation frequency eliminates the block (fig.2.2c). If, however, we increase the anisotropy ratio to $AR = 4.6$ each wave will be blocked at the boundary regardless of the frequency of stimulation (fig.2.2d and 2.2e).

Overall, we found that we can always obtain the waveblock at some critical anisotropy ratio, and its value decreases with an increase in a frequency of stimulation. In addition to frequency, other factors can also affect block formation. In the next section we study, how conductivities of main ionic channels and external conditions, such as elevation of the outer potassium concentration

($[K^+]_o$), typical for ischemia, affect the formation of block at the anisotropic boundary.

2.3.4 Channel blockers

Here as in the previous simulations, we considered two areas with orthogonal fiber directions and stimulated a plane front propagation through the boundary from the transverse to the longitudinal fiber direction. The wave front was parallel to the border between these areas. We decreased the conductivities of various ionic currents to 75%, 50%, 25% of their normal values and calculated the dependence of the basic cycle length (BCL) on critical anisotropy ratio. In Fig. 2.3 we present the data on how such changes in conductivities of ionic currents and other parameter used in our simulation affect duration of action potential.

Sodium current I_{Na} . Fig. 2.4a demonstrates how frequency and I_{Na} affect the critical anisotropy ratio. We see that at low frequency and normal I_{Na} (the blue line) the critical ratio is 3.7, however, if the frequency increases to 2.5 Hz, the ratio decreases to 3.3. The minimal stimulation period in normal conditions in TP06 is about 300 ms, and for the high frequencies the critical anisotropy ratio decreases dramatically to approximately 2.9 and becomes heavily dependent on the stimulation rate. We also see that decrease in G_{Na} to 75%, 50%, 25% progressively decreases the critical anisotropy ratio, and it occurs for all frequencies of stimulation. For short period we also see that block of I_{Na} result in a decrease of the critical anisotropy ratio and the curves for lower value of I_{Na} are slightly above the curves corresponding to higher I_{Na} values. Quantitatively for 75% of I_{Na} the critical anisotropy ratio changes to 3.6 for long period (3% decrease) and to approximately 2.7 for short period (7%). If the G_{Na} is further decreased to 50%, the ratio progressively decreases to 3.4 (9%) and 2.4 (17%) for longer and shorter periods respectively, and for 25% of G_{Na} the typical change is around 26% and 32%.

Therefore, one can see that both frequency and G_{Na} decrease the critical anisotropy ratio and consequently increase the probability of block formation. All these results can be easily explained as the decrease in sodium current I_{Na} causes the decrease of the excitability of cardiac cells and eases block formation.

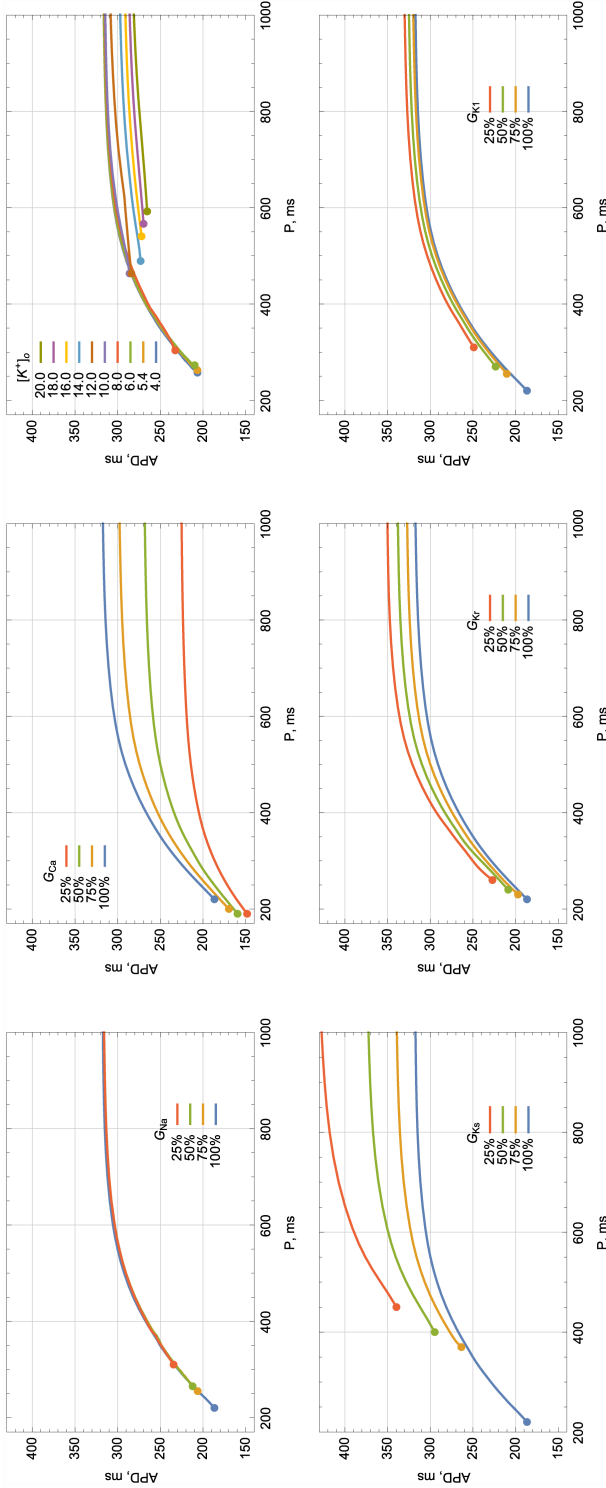


Figure 2.3: **APD₉₀ restitution curves** for various conductivities of ionic currents and external $[K^+]_o$ concentration: (a) Inhibition of I_{Na} ; (b) Inhibition of I_{Ca} ; (c) Hyperkalemia. (d) Inhibition of I_{Ks} ; (e) Inhibition of I_{Kr} ; (f) Inhibition of I_{K1} ; The graphs show dependency of APD₉₀ on the period of stimulation. The blue line on each graph corresponds to the normal parameter values. Different colors show the curves for decreased values of the various ionic conductivities or external $[K^+]_o$ concentration, marked in the frame of each sub-figure. Frequencies higher than 2.7 Hz were obtained by gradual decrease of the period by 5 ms per cycle.

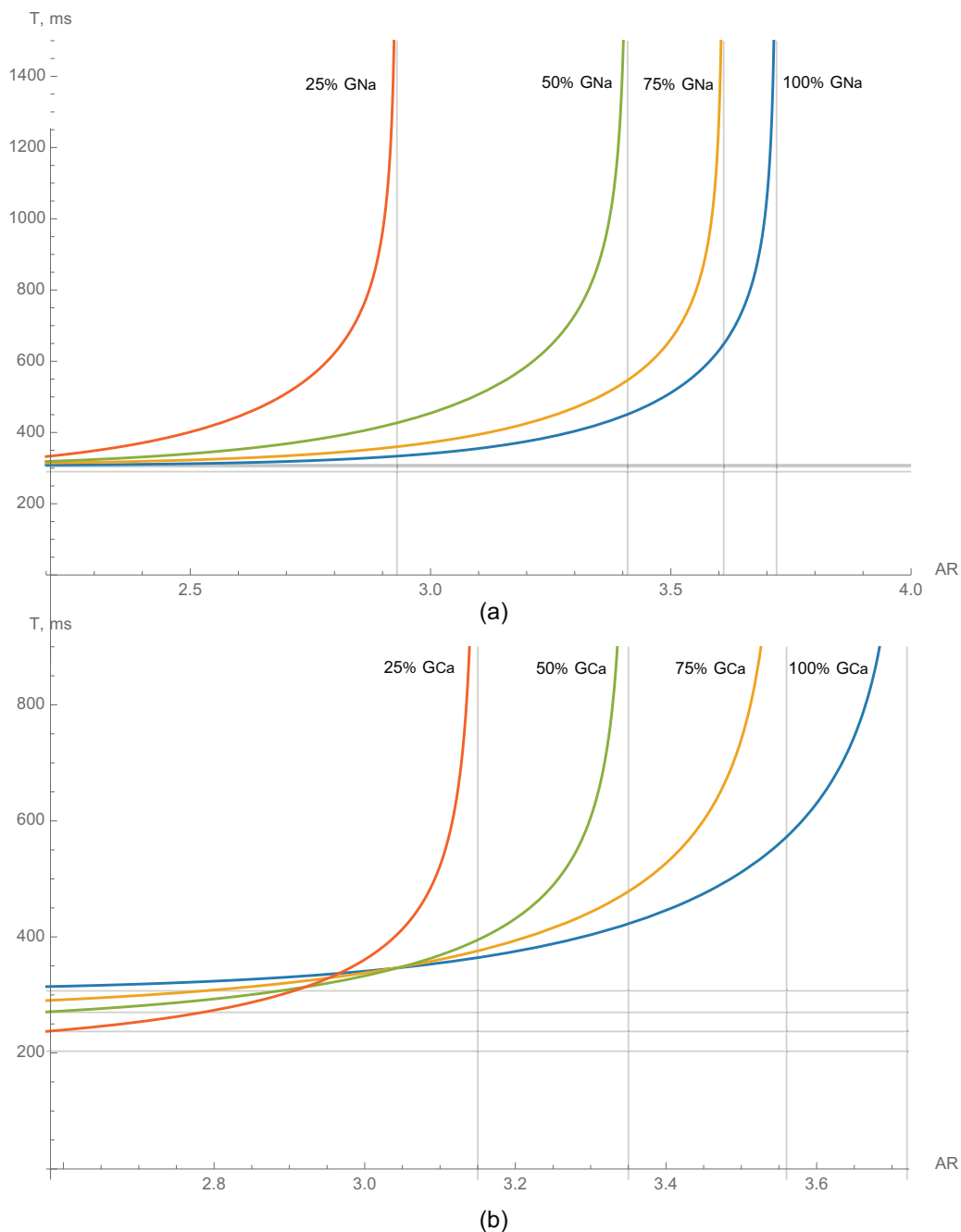


Figure 2.4: The dependencies of the critical period of stimulation on the anisotropy ratio for normal cardiomyocytes (blue line) and with addition of various channel blockers. Inhibition of (a) – I_{Na} , (b) – I_{Ca} .

Calcium current I_{CaL} . Next we studied how decrease in I_{CaL} affects block formation (fig. 2.4b). Similar to the block of I_{Na} , we can see change of vertical asymptote position, that corresponds to a decrease of the critical anisotropy ratio for a long stimulation period. However, for short period the situation is different. Here we see that at short period of stimulation the critical ratio decreases with increased block of I_{CaL} and the curves shown in fig. 2.4b intersect each other around a point (3.0, 340).

We can explain such behavior as follows: shifting of a vertical asymptote is caused by the effect of I_{CaL} on the wavefront: decrease in I_{CaL} reduces the excitability of the tissue inducing the block at smaller anisotropy ratio. Additional effect of block of I_{CaL} is shortening of APD (fig. 2.3). For long stimulation period this effect is not essential, as there is a sufficient time for the cells to recover their properties before the next wave arrives. However, at short period of stimulation this shortening becomes essential and as a result the tissue with lower I_{CaL} for the same short period of stimulation is better recovered and thus wavefront is more stable. Therefore, one can see that at high frequency (short period) critical anisotropy ratio increases with block of I_{CaL} .

Potassium delayed rectifier currents I_{Kr} , I_{Ks} . We have also studied how inhibition of various potassium currents affects the block formation (fig. 2.5). We have decreased I_{Kr} and I_{Ks} separately to 75%, 50% and 25% of their normal values. Rapid delayed rectifier current I_{Kr} (fig. 2.5a) has almost no impact on the block formation. The critical anisotropy ratio slightly changes from 3.72 at normal conditions to 3.74 when only 25% of G_{Kr} is available (0.5% change) and APD slightly elongates (APD₉₀ at 1 Hz becomes 8% longer, see fig. 2.3). Slow delayed rectifier current I_{Ks} (fig. 2.5b) does not change the asymptote position, which means, that at long period of stimulation this current does not affect block formation. However, at high frequencies (short period) critical anisotropy ratio slightly decreases. We explain that similarly to what we saw for block of I_{CaL} : I_{Ks} inhibition elongates APD (fig. 2.3) and thus at high frequency waveblock occurs for a lower anisotropy ratio.

Hence, both I_{Kr} and I_{Ks} does not influence the upstroke directly and have almost no effect on block formation at low frequencies. Whereas at high fre-

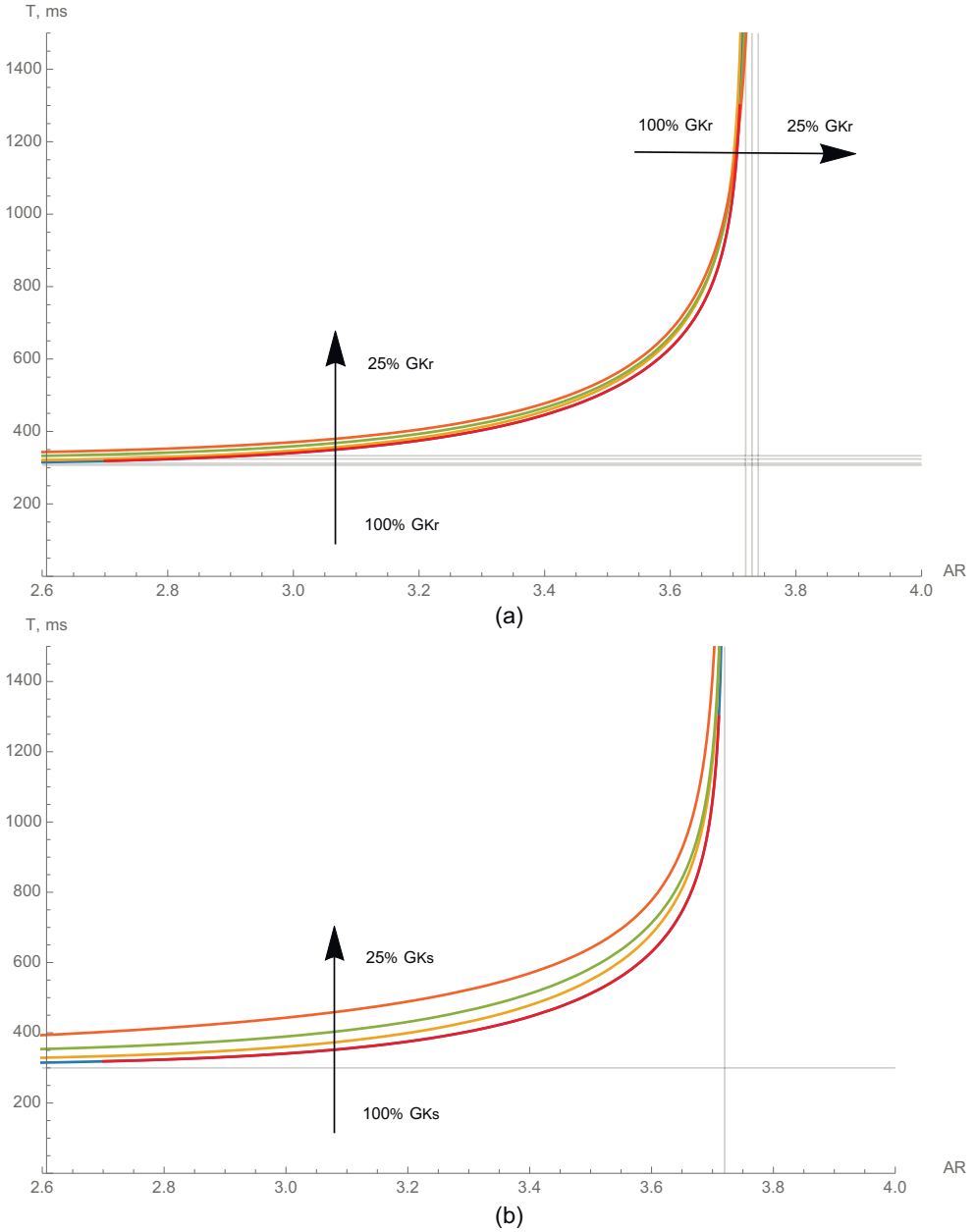


Figure 2.5: The dependencies of the critical period of stimulation on the anisotropy ratio for normal cardiomyocytes (red line) and with various potassium currents suppressed. Inhibition of (a) – I_{Kr} and (b) – I_{Ks} . The vertical asymptotes to these plots correspond to the critical anisotropy ratio for a single travelling pulse.

quencies all the changes are based on the interaction with the refractory tail, which is mainly determined by effect of these channels on the APD (fig. 2.3).

Inward rectifier current I_{K1} . With the decrease of I_{K1} (fig. 2.6) we see a significant change of asymptote position, that shifts from 3.72 for normal conditions to 3.90, 4.32 and 6.20 for 75%, 50% and 25% of G_{K1} respectively. Therefore we can conclude that reduction of conductivity of I_{K1} substantially reduces ability of the wave block formation. Indeed, for anisotropy 3.7 the block occurs at 0.9 Hz stimulation at normal conditions, whereas for reduced I_{K1} it occurs at 1.9 Hz for 75%, 2.5 Hz for 50% and 2.7 Hz for 25% of G_{K1} .

The major difference between inward rectifier current I_{K1} and other potassium currents I_{Kr}/I_{Ks} is that I_{K1} not only influence the repolarization, but also has a significant effect on the upstroke of the action potential. Moreover, I_{K1} does not have a time-dependant gate variables and works as an outward current between -70 mV and 0 mV with a peak at -50.86 mV [22] and TP06 model accurately mimics the current-voltage characteristics of this current [19].

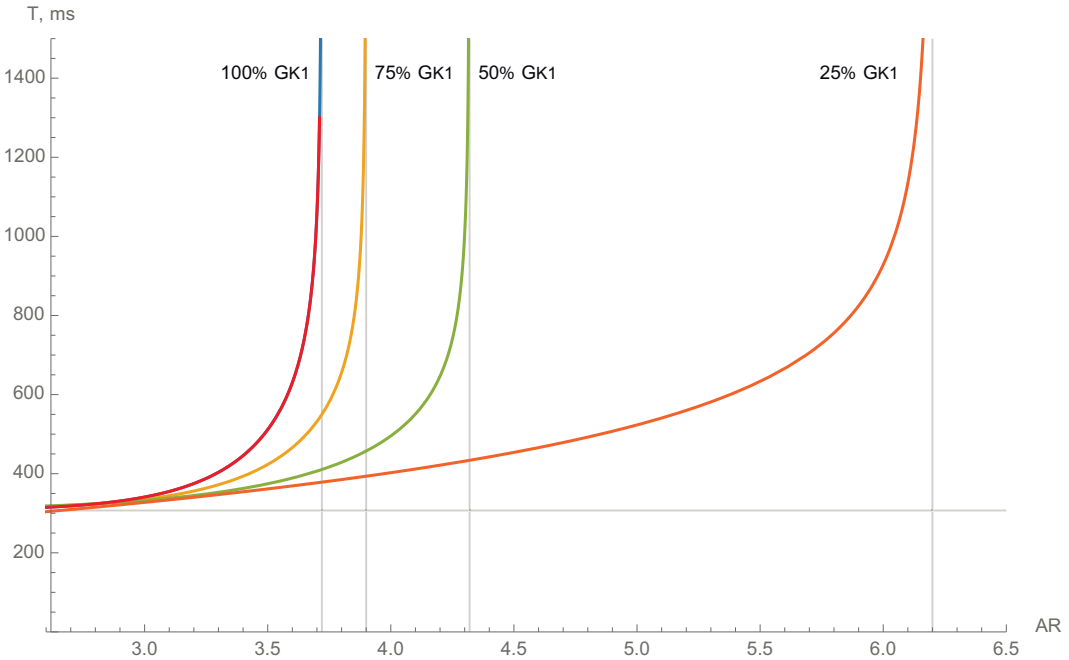


Figure 2.6: The dependencies of the critical period of stimulation on the anisotropy ratio for normal cardiomyocytes (red line) and with inward rectifier potassium current I_{K1} suppressed.

Consequently, I_{K1} affects the APD by two mechanisms: first during the wavefront, and second — in the repolarization phase, restoring action potential.

Hence, the decrease of I_{K1} , on the one hand, rises the excitability and eliminates the block, due to its decreased impact on the wavefront. On the other hand, it depolarises the cell, resulting in a lower availability of sodium channels and provoking a block. In our simulations the first effect was more pronounced, and if G_{K1} was between 15% and 100% of its normal value, AR rose with the decrease of G_{K1} . If G_{K1} was further decreased (below 10%), the cells were depolarised and showed self-oscillations. However, in this research we limit our study to moderate changes of the ionic current, and we conclude that moderate inhibition of I_{K1} to 15–50% prevents block formation at low frequencies of stimulation and does not notably affects block formation at high frequencies of stimulation.

In order to investigate why inhibition of I_{K1} changes the critical anisotropy in unexpected way we performed additional simulations which highlight effects of I_{K1} . In particular, we switched off I_{K1} at different phases of action potential formation and observed if such modification eliminates the effects of I_{K1} change. As we can see in fig.2.6 the critical AR ≈ 6.0 at 1 Hz and 25% G_{K1}), while at 100% G_{K1} and 1 Hz the block occurs at AR ≈ 3.7 .

First, we blocked I_{K1} only at the wavefront (set its conductance 25% G_{K1} for $dV/dt > 0$), while for all other phases we used 100% G_{K1} . We found that the critical anisotropy ratio at 1Hz was AR ≈ 6.0 . However, if we did the same for the repolarization phase only (25% G_{K1} for $dV/dt < 0$ and 100% G_{K1} for $dV/dt > 0$), the effect of partial block of I_{K1} completely disappeared, and the block occurred at AR ≈ 3.7 as for the normal conductance of I_{K1} . Hence, we concluded the change of AR occurs due to effects of I_{K1} during the upstroke of the action potential. To locate the exact phase of the upstroke, where effect of I_{K1} is important, we blocked it separately either before activation of I_{Na} or after activation of I_{Na} . In our model, I_{Na} is activated if $V > -50$ mV. Therefore, we did similar simulations in which we either blocked I_{K1} on the upstroke when $I_{Na} \approx 0$ ($V < -50$ mV), or did it for nonzero I_{Na} when $V > -50$ mV. We found that in the first case, when I_{K1} blocked before activation of I_{Na} the critical anisotropy ratio AR ≈ 6.0 , while in the second case when I_{K1} blocked after activation of I_{Na} AR ≈ 3.7 . Hence, we conclude that the main

effects of I_{K1} occurs because it makes more difficult reaching the threshold of excitation of tissue. This can also explain, why I_{K1} current, which value is small compared to I_{Na} , can still have a substantial effect on wave propagation.

Hyperkalemia. Finally, we studied effect of hyperkalemia (fig. 2.7) — one of the most important consequences of ischemia. As most of cardiac arrhythmias occur under ischemic conditions, the influence of such conditions on the block formation is important. We have found that increase of the extracellular K^+ concentration results in a complex, nonmonotonous change in critical anisotropies (fig. 2.7a). Before we analyze the curves shown in this figure, let us consider a more simple representation shown in Fig. 2.7b — dependency of critical anisotropy ratio (AR) vs. the potassium concentration ($[K^+]_o$) for several stimulation frequencies. (0.5 Hz, 1 Hz, 2 Hz and 2.5 Hz).

One can see, that at low frequencies (0.5 Hz or 1 Hz) the critical anisotropy ratio starts growing from 3.72 in normal conditions to maximal value of around 4.8 at $[K^+]_o = 8$ mM for 0.5 Hz and 4.6 for 1 Hz. Further increase of $[K^+]_o$ until approximately 12 mM results in a steep decline of the critical AR until approximately 2.3 for 0.5 Hz and 2.2 for 1 Hz, which is even lower than in normal conditions. Additional increase of $[K^+]_o$ does not influence the block formation significantly. At high frequencies of stimulation (2.5 Hz) the critical anisotropy ratio is 3.4 in normal conditions and monotonically decreases to 1.6 with increase of $[K^+]_o$.

This complex behavior can be explained as follows: the increase of $[K^+]_o$ shifts the resting potential to less negative values. That, on the one hand, brings the resting potential closer to the threshold of excitations. On the other hand, such depolarization results in partial inactivation of the sodium channels. As a result, we see an increase of the critical anisotropy ratio. However, further increase in $[K^+]_o$ substantially decreases the availability of sodium channels, that decreases the excitability of cardiac cells and results in a decrease of critical anisotropy ratio. These effects are apparent at low stimulation frequency. At high stimulation frequency, however, the sodium current is already partially suppressed, and thus, the first phase of increase in AR is absent.

Now we can explain the results presented in fig.2.7a. The vertical asymptote, first, shifted right to $AR = 4.7$ at $[K^+]_o = 8$ mM, whereas the horizontal

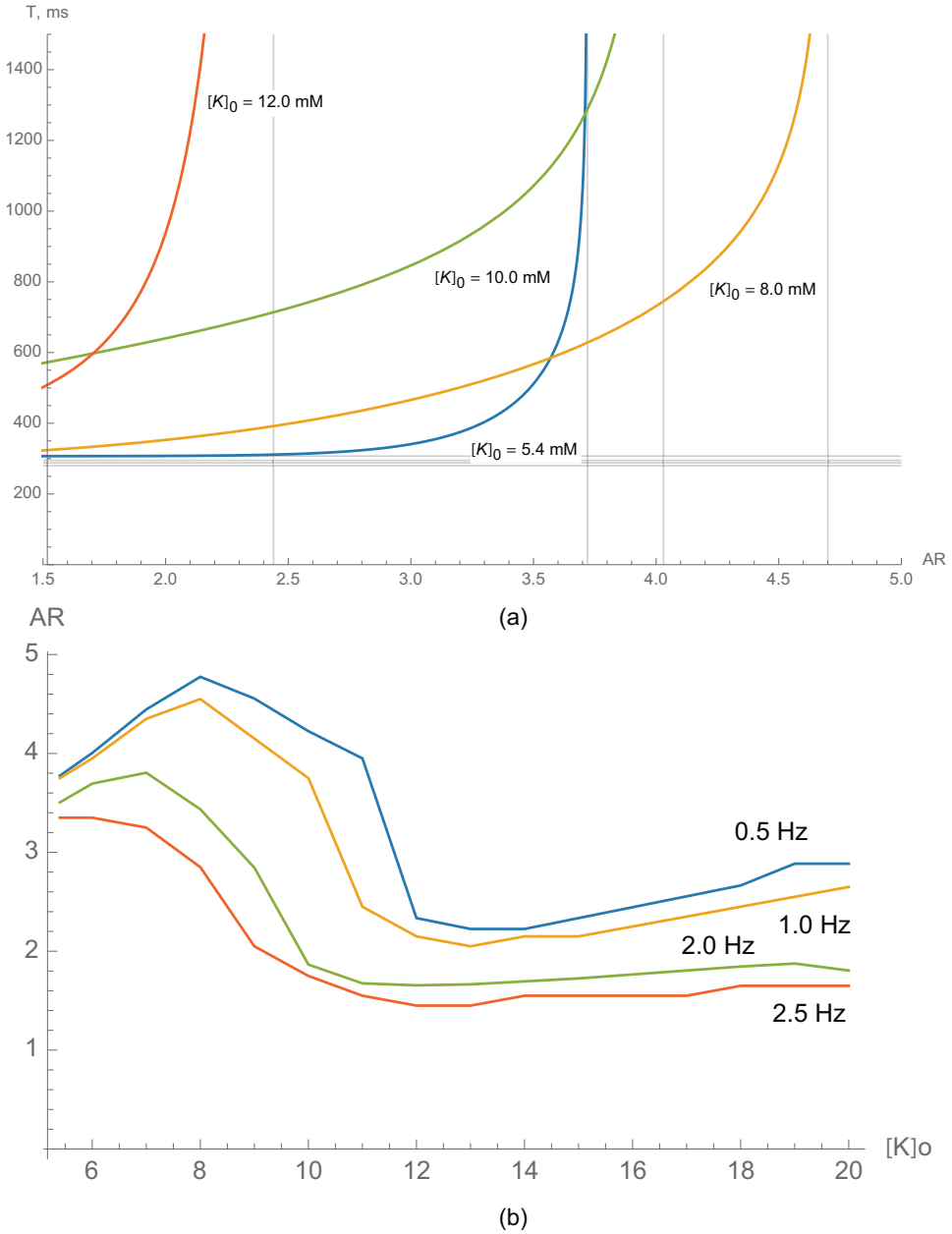


Figure 2.7: **Conditions for waveblock formation in hyperkalemia.**

a) The dependence of critical period of stimulation on anisotropy ratio (AR) for various potassium concentrations outside of the cell $[K^+]_o$. Blue line shows critical period of stimulation at normal conditions ($[K^+]_o = 5.4$ mM).
 b) The dependence of critical anisotropy ratio on potassium concentration outside of the cell $[K^+]_o$ for various stimulation frequencies.

Table 2.1: Critical anisotropy ratio and fitting parameters.

Conditions		AR_1	a	b	c	d
Normal		3.72	307	0.0014	9.09	0.333
Na (fig. 2.4a)	75%	3.61	310	0.013	7.56	0.333
	50%	3.41	304	0.1	6.31	0.333
	25%	2.93	290	0.3	6.15	0.333
Ca (fig. 2.4b)	75%	3.56	264	0.05	6.34	0.429
	50%	3.35	246	0.06	6.20	0.432
	25%	3.15	203	0.09	6.00	0.463
Kr (fig. 2.5a)	75%	3.72	312	0.0018	8.89	0.362
	50%	3.73	324	0.0026	8.54	0.410
	25%	3.74	333	0.0066	7.74	0.484
Ks (fig. 2.5b)	75%	3.72	318	0.0037	8.40	0.347
	50%	3.72	339	0.011	7.56	0.349
	25%	3.72	350	1.0	3.96	0.448
K1 (fig. 2.6)	75%	3.90	310	0.004	7.94	0.333
	50%	4.32	308	0.07	5.42	0.333
	25%	6.20	207	44.95	1.25	0.333
$[K^+]_o$ (fig. 2.7)	8.0 mM	4.70	295	15.50	2.33	0.300
	10.0 mM	4.03	288	340	0.46	0.403
	12.0 mM	2.44	281	189	0.19	1.360

asymptote does not change significantly. This change corresponds to increase of excitability with no change in APD (fig. 2.3). During further increase of $[K^+]_o$ the vertical asymptote shifts left to $AR = 2.44$ for $[K^+]_o = 12$ mM, as there are less sodium channels available. The APD in hyperkalemia slightly shortens (fig. 2.3), which results in a vertical downward shift of the horizontal asymptote from 307 ms in normal conditions to 281 ms at $[K^+]_o = 12$ mM.

All the dependencies above were fitted with the function:

$$T(AR) = a + \frac{bAR^c}{(AR_1 - AR)^d},$$

where AR_1 is a critical anisotropy for a single travelling pulse and a the refractory period at high frequency (short period) and b, c and d are free parameters. The values of the parameters for all curves shown in fig. 2.4–2.7 are presented in Table 2.1.

2.3.5 Block of propagation and reentry formation

In previous sections we have shown that the waveblock can occur at the border between areas with orthogonal fiber orientation. Here we study how this waveblock can result in sustained patterns of excitation.

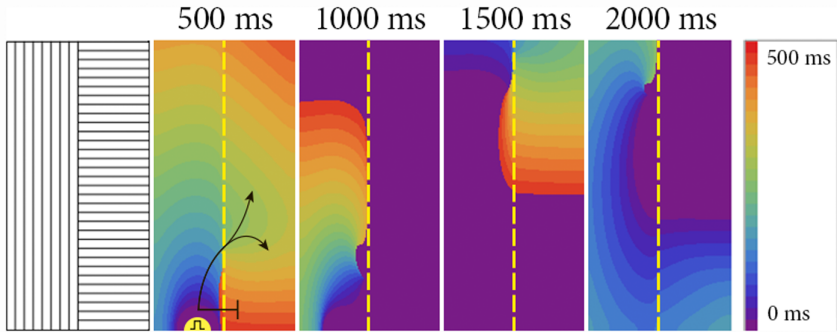


Figure 2.8: **Formation of transient reentry (ectopic beats)** at the border between areas with orthogonal fiber direction. Two stimuli were applied 6 mm from the border with delay of 500 ms. The anisotropy ratio is 2.0 and $[K^+]_o$ is 10 mM. Size of the tissue : 6.4 cm \times 3.2 cm.

Fig. 2.8 shows formation of transient reentrant source as the result of point stimulation. We see that initially elliptic wavefront reaches the boundary and is blocked there (marked by \perp symbol in fig. 2.8 at 500 ms). However, the distal parts of the front have an incidence angle larger than zero, and thus, changes of the resistance in the incidence direction become smaller, and consequently it penetrates into the right part of the medium in a place about 1 cm away from stimulation point (shown by arrows in fig. 2.8 at 500 ms). Eventually, a reentrant pattern is formed. This pattern, however, is not stable and drifts upwards. To illustrate this drift we performed the same simulations in a domain, which has the same thickness, but is 4 times longer in the vertical direction. We see that the drift continues and the wave finally annihilates at the upper boundary of the tissue (fig. 2.9). Such drift is a result of anisotropy change of cardiac tissue and can be understood from simple geometrical considerations: faster propagation along the border in the left part than in the right part of the medium results in overall shift upwards for the given direction of rotation (see also [23]). To limit the drift in the next simulation we add an isotropic area around the border fig. 2.10. In this case, reentry, which occurs via similar

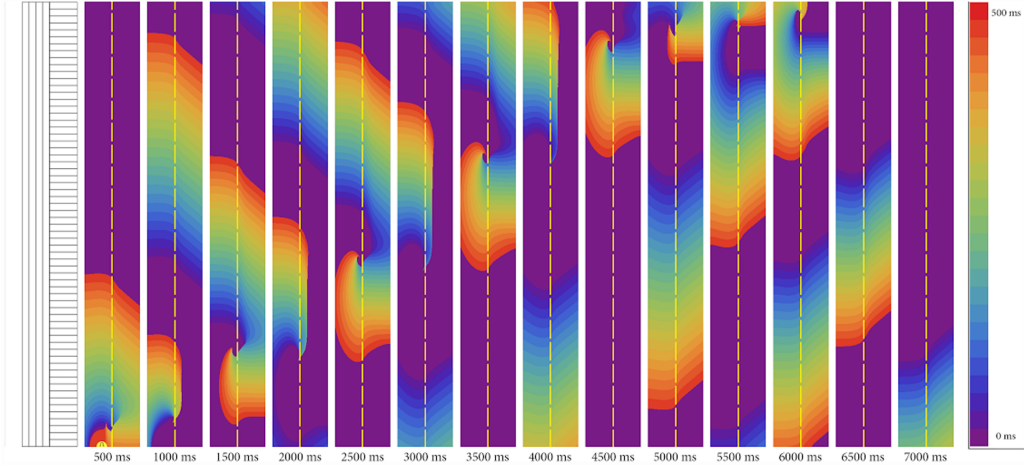


Figure 2.9: **Drift of the re-entry.** The same simulation as in fig. 2.8 in the tissue with the size $25.6 \text{ cm} \times 3.2 \text{ cm}$.

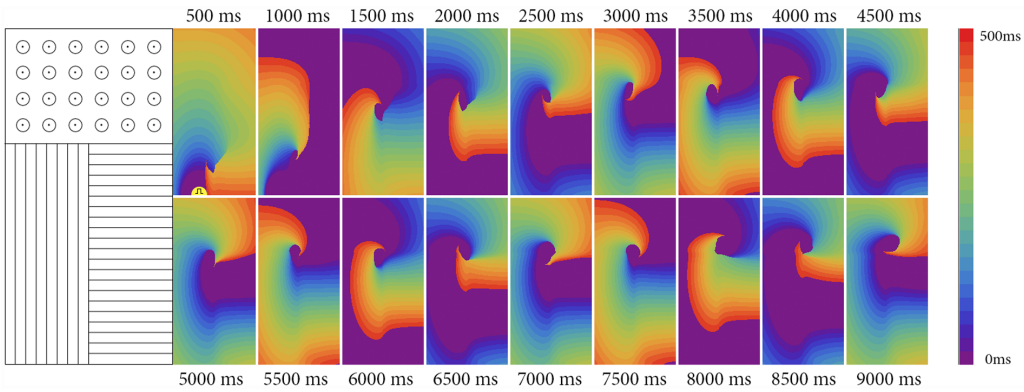


Figure 2.10: **Reentry formation** at the border between areas with orthogonal fiber direction, stabilized at the isotropic area. Two point stimuli were applied 6 mm from the border with delay of 500 ms. The anisotropy ratio is 2.0 and $[K^+]_o$ is 10 mM. Fibers alignment is shown in the left figure. Size of the tissue: $6.4 \text{ cm} \times 3.2 \text{ cm}$.

mechanism, reaches the isotropic area and stabilizes there. Therefore, we see that the stable reentrant pattern can be formed at the anisotropic boundary due to the waveblock formation mechanism studied in this paper.

All the results above were obtained in conditions of severe hyperkalemia ($[K^+]_o = 10 \text{ mM}$). It is possible to initiate the reentry in similar systems in normal conditions, but the anisotropy ratio should be two times higher (see fig. 2.7b for 2 Hz).

Discussion

In this paper we performed a detailed study of the waveblock formation at the anisotropic boundary. Although this system was already studied using low dimensional model of cardiac cell [18], here we use an ionic model for human cardiac tissue for the first time for describing such sistem of abrupt change of fiber direction. In addition, we studied in details how formation of the waveblock depends on the period of simulation and on conductivity of different ionic currents.

Our main conclusion is that such block is possible and it occurs for reasonable values of the anisotropy ratio (between 2.4 and 6.2 with respect to the velocities of propagation). Changes of conductivity of ionic currents have a substantial effect on the critical anisotropy ratio. From the results, explicated above, I_{K1} had the greatest effect on block formation. Suppression of I_{Na} and I_{Ca} resulted in 21% and 15% changes in critical anisotropy ratio, respectively. If we assume that arrhythmias occur via sink-source mismatch mechanism, then the blockers of inward rectifier current (I_{K1}) should be most effective in arrhythmia prevention. On the contrary, antiarrhythmic agents of class I (blocking I_{Na}) and of class IV (blocking I_{Ca}) increase the probability of block formation, decreasing critical anisotropy and critical frequency. Antiarrhythmic drugs of class III (affecting I_{Kr}) play no effect in considered scenario of block formation.

Note, that the waveblock in this situation occurs only for the waves propagating from the region with lower propagating velocity to the region with faster propagating velocity, as at such boundary density of the current decreases. If the wave propagates to the opposite directions (not shown in fig. 2.2), it can always pass the boundary, as in that case the density of the current at the boundary increases. Therefore in this case we have formation of so-called uni-directional block, i.e. a situation when the wave is blocked in one direction, but can propagate into the opposite direction. Formation of uni-directional blocks important for the onset of the reentrant sources of excitation.

Propagation of the excitation wave across the border between areas with different coupling coefficients was previously studied by Zemlin and Pertsov [24, 25] using the Luo and Rudy model [26] for guinea pig ventricular tissue and

Ramirez et al. [27] model of canine atrial tissue. In these studies the transition between the regions with different coupling coefficients was smooth at some regions of the border and abrupt at another border regions. It was shown, that reentry can be formed in such system due to partial block of excitation. The scenario was related to the problem of onset of re-entry in a pulmonary veins regions during atrial fibrillation and bradycardiac onset of re-entry in ventricles. Although the setup of boundary, anisotropy and model used [24, 25] were different, the biophysical mechanism of waveblock observed in [24, 25] is similar to that studied in our paper. Therefore, it would be interesting to find out how the changes in ionic currents studied in our paper would effect the processes of reentry formation in the setup of [24, 25] and what potential effect it may have for atrial fibrillation.

It would be interesting to study the conditions for waveblock formation described in this paper also in experiment. One can do it using the neonatal cell cultures, grown on specific scaffolds, providing preferential direction for elongation of the cells, as we did in our previous work [18]. By varying the anisotropy ratio in the samples, it is possible to compare the probability of block formation in normal conditions and with suppressed I_{Na} (with TTX) and I_{Ca} (with nifedipine), or in hyperkalemia (in a media with higher K^+ concentration). For human cardiac cells relative study can potentially be done using IPS cells [28].

In this paper we have studied one of the effects of acute ischemia: hyperkalemia. Another effect of ischemia which has a pronounced influence on the dynamics of the reentrant patterns is hypoxia [29, 30]. In hypoxia the duration of APD can be substantially shorter due to opening of $I_{K_{ATP}}$, and, consequently, the wavelength of the reentry can be substantially reduced. As a result, the waveblocks formed at the boundary become stable and could be stabilized in media of smaller size.

We studied effect of block in 2D model of cardiac tissue, but, in many parts of the heart, e.g. ventricles, cardiac propagation is essentially 3D. Thus, it is interesting to understand the mechanisms of waveblock formation in 3D as well. From a general theoretical point of view, plane wave propagation in 3D is quasi 2D, thus in that situation simulations performed in our study can be applied for some 3D effects. For curved 3D wavefronts theoretical considerations indicate

that curvature effects there depend on the mean curvature of the wavefront [31, 32], meaning that the curvature effect on the wave propagation in 3D will be even more essential than in 2D. Thus, wave block formation in similar conditions in 3D is more feasible.

In this paper we studied block formation at the boundary of abrupt change of fibers in homogenous cardiac tissue. However, in addition to anisotropy other factors are important for block formation. One of them is heterogeneity of cardiac tissue [33]. Changes of conductances of various ionic channels in addition to the effects of block formation on the border between anisotropic areas studied in this paper may also result in change of heterogeneity of cardiac tissue. For example Colman et al. [34], showed that channel blockers for I_{K1} and I_{Kr} increase electrical heterogeneity and plays pro-arrhythmogenic role, in spite of the fact that they also increase the wavelength and in such a way display anti-arrhythmogenic effect. Increased heterogeneity also results in re-entry instability [34, 35]. In view of that it would be interesting to study a combined effect of reduction of ionic currents on the onset of arrhythmias in a setup which combines anisotropy changes with APD heterogeneity.

2.4.6 Limitations

We did not use a bidomain description for cardiac tissue. A recent study [36] showed that for normal propagation and recovery the monodomain and bidomain approaches give similar results. We expect this to be valid also for our studies of propagation block. However, this statement needs to be validated in the subsequent studies. We studied the effects for a simple geometry of the boundary only: an anisotropy change along a straight line. It would be interesting to also study similar effects for a more complex boundary, which has a curvature, and find out, if this has any effect on the conditions for the block formation. We performed our simulations using a TP06 model of cardiac tissue. It will be interesting to study similar phenomenon for other models of human and animal cardiac cells, such as [37–39]. We also performed simulations in 2D models for homogeneous cardiac tissue. It would be interesting to conduct similar studies in 3D and anatomically accurate geometries and also in the presence of ionic heterogeneities of cardiac tissue.

Acknowledgments

The research was fully supported by two sources: the Ministry of Education and Science of the Russian Federation (Federal Program “5top100”) and FWO-Flanders.

References

- [1] D. P. Zipes and H. J. Wellens, “Sudden cardiac death.,” *Circulation*, vol. 98, pp. 2334–51, 1998.
- [2] Y. Watanabe, “Reassessment of parasystole.,” *American heart journal*, vol. 81, pp. 451–66, 1971.
- [3] P. F. Cranefield, A. L. Wit, and B. F. Hoffman, “Conduction of the Cardiac Impulse III . Characteristics of very slow conduction,” *The Journal of general physiology*, vol. 59, pp. 227–246, 1972.
- [4] B. P. F. Cranefield, D. Ph, A. L. Wit, and B. F. Hoffman, “Genesis of Cardiac Arrhythmias,” *Circulation*, vol. XLVII, no. January, 1973.
- [5] A. G. Mayer, “Further Studies of Nerve Conduction in Cassiopea,” *Proceedings of the National Academy of Sciences of the United States of America*, vol. 2, no. 12, pp. 721–726, 1916.
- [6] G. K. Moe and J. A. Abildskov, “Atrial fibrillation as a self-sustaining arrhythmia independent of focal discharge.,” *American heart journal*, vol. 58, pp. 59–70, 1959.
- [7] V.I. Krinsky, “Self-Organization: Autowaves and Structures Far from Equilibrium,” 1984.
- [8] A. Karma, “Spiral breakup in model equations of action potential propagation in cardiac tissue,” *Phys. Rev. Lett.*, vol. 71, pp. 1103–1106, 1993.
- [9] Z. Qu, J. N. Weiss, and A. Garfinkel, “Cardiac electrical restitution properties and stability of reentrant spiral waves: a simulation study,” *American Journal of Physiology-Heart and Circulatory Physiology*, vol. 276, no. 1, pp. H269–H283, 1999.
- [10] A. Panfilov and A. Holden, “Self-generation of turbulent vortices in a two-dimensional model of cardiac tissue,” *Physics Letters A*, vol. 151, no. 1-2, pp. 23–26, 1990.

- [11] A. V. Panfilov and A. M. Pertsov, “Mechanism for the appearance of spiral waves in active media, associated with the phenomenon of critical curvature(in damaged myocardium tissues),” *Biofizika*, vol. 27, pp. 886–889, 1982.
- [12] V. G. Fast and G. Kleber, “Role of wavefront curvature in propagation of cardiac impulse,” *Cardiovascular research*, vol. 33, pp. 258–271, 1997.
- [13] C. Cabo, A. M. Pertsov, J. M. Davidenko, *et al.*, “Vortex shedding as a precursor of turbulent electrical activity in cardiac muscle.,” *Biophysical journal*, vol. 70, pp. 1105–11, 1996.
- [14] K. Agladze, J. Keener, S. Müller, and A. Panfilov, “Rotating Spiral Waves Created by Geometry,” *Science*, 1994.
- [15] R. Majumder, R. Pandit, and A. V. Panfilov, “Turbulent electrical activity at sharp-edged inexcitable obstacles in a model for human cardiac tissue,” *American Journal of Physiology-Heart and Circulatory Physiology*, vol. 307, no. 7, pp. H1024–H1035, 2014.
- [16] C. Cabo, A. M. Pertsov, W. T. Baxter, *et al.*, “Wave-front curvature as a cause of slow conduction and block in isolated cardiac muscle.,” *Circulation research*, vol. 75, pp. 1014–28, 1994.
- [17] S. Rohr, J. P. Kucera, and V. G. Fast, “Paradoxical Improvement of Impulse Conduction in Cardiac Tissue by Partial Cellular Uncoupling,” *Science*, vol. 275, no. February, 1997.
- [18] N. Kudryashova, A. Teplenin, Y. Orlova, L. Selina, and K. Agladze, “Arrhythmogenic role of the border between two areas of cardiac cells alignment,” *Journal of Molecular and Cellular Cardiology*, 2014.
- [19] K. H. W. J. ten Tusscher, D. Noble, P. J. Noble, and a. V. Panfilov, “A model for human ventricular tissue.,” *American journal of physiology. Heart and circulatory physiology*, vol. 286, pp. H1573–89, 2004.
- [20] K. H. W. J. ten Tusscher and a. V. Panfilov, “Alternans and spiral breakup in a human ventricular tissue model.,” *American journal of physiology. Heart and circulatory physiology*, vol. 291, pp. H1088–100, 2006.
- [21] R. H. Clayton, O. Bernus, E. M. Cherry, *et al.*, “Models of cardiac tissue electrophysiology: progress, challenges and open questions.,” *Progress in biophysics and molecular biology*, vol. 104, pp. 22–48, 2011.
- [22] A. S. Dhamoon and J. Jalife, “The inward rectifier current (IK1) controls cardiac

- excitability and is involved in arrhythmogenesis.,” *Heart rhythm : the official journal of the Heart Rhythm Society*, vol. 2, pp. 316–24, 2005.
- [23] A. V. Panfilov, “Theory of Reentry,” in *Cardiac Electrophysiology: From Cell to Bedside 5th edition* (D. Zipes and J. Jalife, eds.), pp. 329–337, 2009.
- [24] C. W. Zemlin and A. M. Pertsov, “Bradycardic onset of spiral wave re-entry: structural substrates,” *Europace*, vol. 9, no. suppl_6, pp. vi59–vi63, 2007.
- [25] C. W. Zemlin, B. G. Mitrea, and A. M. Pertsov, “Spontaneous onset of atrial fibrillation.,” *Physica D. Nonlinear phenomena*, vol. 238, pp. 969–975, 2009.
- [26] G. M. Faber and Y. Rudy, “Action potential and contractility changes in $[\text{Na}^+]_i$ overloaded cardiac myocytes: a simulation study,” *Biophysical journal*, vol. 78, no. 5, pp. 2392–2404, 2000.
- [27] R. J. Ramirez, S. Nattel, and M. Courtemanche, “Mathematical analysis of canine atrial action potentials: rate, regional factors, and electrical remodeling,” *American Journal of Physiology-Heart and Circulatory Physiology*, vol. 279, no. 4, pp. H1767–H1785, 2000.
- [28] P. Lee, M. Klos, C. Bollensdorff, *et al.*, “Simultaneous voltage and calcium mapping of genetically purified human induced pluripotent stem cell-derived cardiac myocyte monolayers.,” *Circulation research*, vol. 110, pp. 1556–1563, 2012.
- [29] E. Carmeliet, “Cardiac Ionic Currents and Acute Ischemia : From Channels to Arrhythmias,” *Physiological reviews*, vol. 79, no. 3, pp. 917–1018, 1999.
- [30] I. V. Kazbanov, R. H. Clayton, M. P. Nash, *et al.*, “Effect of Global Cardiac Ischemia on Human Ventricular Fibrillation: Insights from a Multi-scale Mechanistic Model of the Human Heart.,” *PLoS computational biology*, vol. 10, p. e1003891, 2014.
- [31] J. P. Keener, “A Geometrical Theory for Spiral Waves in Excitable Media,” *SIAM Journal on Applied Mathematics*, vol. 46, pp. 1039–1056, 1986.
- [32] H. Dierckx, O. Bernus, and H. Verschelde, “Accurate Eikonal-Curvature Relation for Wave Fronts in Locally Anisotropic Reaction-Diffusion Systems,” *Physical Review Letters*, vol. 10, no. 2, p. 107, 2011.
- [33] J. Han and G. K. Moe, “Nonuniform recovery of excitability in ventricular muscle,” *Circulation Research*, vol. 14, no. 1, pp. 44–60, 1964.
- [34] M. A. Colman, M. Varela, J. C. Hancox, H. Zhang, and O. V. Aslanidi, “Evo-

- lution and pharmacological modulation of the arrhythmogenic wave dynamics in canine pulmonary vein model,” *Europace*, vol. 16, no. 3, pp. 416–423, 2014.
- [35] F. H. Samie, O. Berenfeld, J. Anumonwo, *et al.*, “Rectification of the background potassium current,” *Circulation research*, vol. 89, no. 12, pp. 1216–1223, 2001.
- [36] M. Potse, B. Dubé, J. Richer, A. Vinet, and R. M. Gulrajani, “A comparison of monodomain and bidomain reaction-diffusion models for action potential propagation in the human heart,” *IEEE Transactions on Biomedical Engineering*, vol. 53, no. 12, pp. 2425–2435, 2006.
- [37] E. Grandi, F. S. Pasqualini, and D. M. Bers, “A novel computational model of the human ventricular action potential and Ca transient,” *Journal of molecular and cellular cardiology*, vol. 48, no. 1, pp. 112–121, 2010.
- [38] Y. Rudy and T. O. Hara, “Simulation of the Undiseased Human Cardiac Ventricular Action Potential : Model Formulation and Experimental Validation,” *PLOS Computational Biology*, vol. 7, no. 5, 2011.
- [39] C. H. Luo and Y. Rudy, “A dynamic model of the cardiac ventricular action potential. I. Simulations of ionic currents and concentration changes,” *Circulation Research*, vol. 74, pp. 1071–1096, 1994.

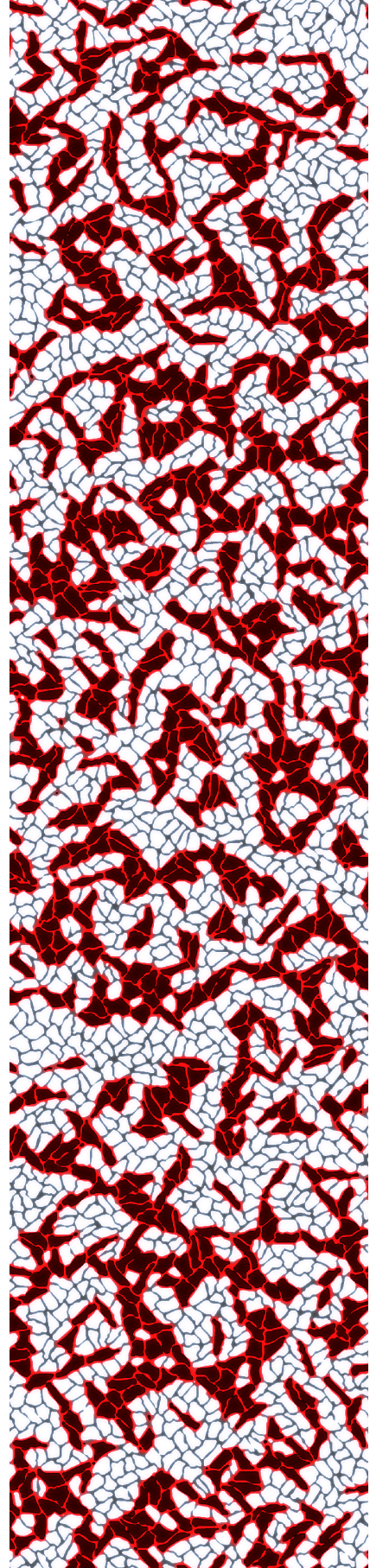
Chapter 3

Excitation wave propagation in a patterned multi-domain cardiac tissue

NN Kudryashova¹, AS Teplenin¹, YV Orlova², and
K Agladze¹

¹Moscow Institute of Physics and Technology, Dolgoprudny, Russia

²iCeMS Research Building, Yoshida Honmachi,
Sakyoku, Kyoto 606-8501, Japan



Abstract

Electrospun fibrous mats are widely used in the contemporary cardiac tissue engineering as the substrates for growing cardiac cells. The substrate with chaotically oriented nanofibers leads to the growth of cardiac tissue with randomly oriented, but internally morphologically anisotropic clusters or domains. The domain structure affects the stability of the excitation propagation and we studied the stability of the propagating excitation waves versus the average size of the domains and the externally applied excitation rate. In an experimental model based on neonatal rat cardiac tissue monolayers, as well as in the computer simulations we found that increase of domain sizes leads to the decrease of the critical stimulation frequencies, thus evidencing that larger domains are having a higher arrhythmogenic effect.

Published: Kudryashova, N.N., Tepenin, A.S., Orlova, Y.V., & Agladze, K.I. (2015). Excitation wave propagation in a patterned multidomain cardiac tissue. *JETP Letters*, 101(11), 772–775.

<http://doi.org/10.1134/S0021364015110089>.

Introduction

Electrospun fibrous mats are widely used in the contemporary cardiac tissue engineering [1–3]. They make versatile and handy scaffolds for the growing cultured tissue with relatively easy control of the tissue architecture [4]. However, a deep understanding of the correlation between the cardiac patches morphology and its functional properties is required in order to avoid a dangerous mismatch of the created implant and the host tissue. For example, it is now recognized that the border between areas with different cell alignment may have a profound arrhythmogenic effect [5]. From the other hand, the electrospun fibrous mats made from the randomly applied polymer nanofibers often give rise to the patterned, multi-domain cardiac tissue, in which within each small domain the cells are essentially aligned, while the direction of the alignment sharply changes in the neighboring domains [4].

In the present work we analyzed the propagation of excitation in the multi-domain excitable medium both computationally and in the *in vitro* model of cardiac tissue. We studied the stability of the propagating excitation waves versus the average size of the domains and the externally applied excitation rate. As an experimental model we used neonatal rat cardiac tissue monolayers grown on the flat substrates covered with the oriented in random directions electrospun nanofibers [4].

As described earlier the single nanofiber leads to the elongation of cardiomyocytes situated in its proximity in the fiber direction [4, 6, 7]. The substrate with chaotically oriented nanofibers leads to the growth of cardiac tissue with randomly oriented, but internally morphologically anisotropic clusters or domains. Varying the positioning density of nanofibrous scaffold we achieved morphologically patterned cardiac monolayers with different average size of domains. Then we applied external electrical stimulation with different frequencies to the tissue layers with various clusters scales and observed their functioning with the aid of the optical mapping [8]. We determined highest (critical) frequency at which one-to-one response to external stimuli occurs for each type of cultures with different domain size. After optical mapping experiments all samples were actin stained the exact sizes of the clusters were determined.

Experimental setup

In order to eliminate natural variations from sample to sample, the experimental system was designed in a way, shown in Figure 3.1. Half of the glass cover slip was covered by the polymer nanofibers and another half was set free of fibers. Cells were seeded on the entire cover slip and cultured for 3-5 days. After that, electric stimulation was applied to the both parts of the cover slip with cultured tissue, as shown in Figure 3.1. Since the cells and the conditions for culturing were identical for both halves of the glass substrate, the only difference in excitation propagation was due to the nanofibers defined architecture of the tissue versus fiber-free uniform distribution of the cultured cardiac cells. In order to avoid mutual interference of the wave patterns formed in the different parts of the cell monolayer, immediately before the experiment they were separated by thin cut made along the border between two areas. Frequency of stimulation was raised from 1 Hz to 10 Hz, until frequency is captured in fiber-free part, but propagation in fiber-covered part is broken.

Simulation

We consider two-variable Aliev-Panfilov model for simulation of excitation waves propagation in a cardiac tissue:

$$\begin{aligned} \dot{u} &= \nabla(D(\vec{x})\nabla u) + cu(1-u)(u-a) - u, \\ \dot{v} &= \left(\epsilon_0 + \frac{\mu_1 v}{\mu_2 + u} \right) (cu(1+a-u) - v), \end{aligned} \quad (3.1)$$

where u is a membrane potential, v is a recovery variable, $D(\vec{x})$ is a coupling coefficients matrix that will be described precisely below, c is an excitability, a is an excitation threshold, and finally parameters μ_1 , μ_2 and ϵ_0 are specific for this model and optimized for fitting the cardiac action potential [9]. This model was chosen for this study, because in spite of its simplicity, it accurately describes the trailing edge, which is quite important for simulation of wave series, stimulated with high frequency. Detailed ionic models [10–12] provide better approximation of action potential, but require more computational time, than two-variable models [13, 14].

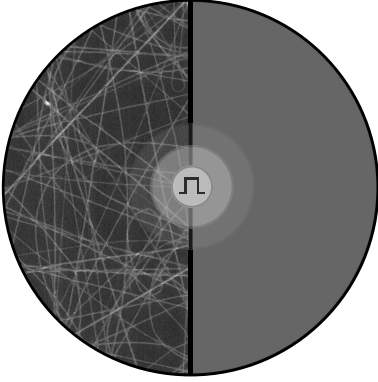


Figure 3.1: Experimental setup. Right half of the glass cover slip was covered by randomized polymer nanofibers. Two halves were separated by thin cut and stimulation was applied at the edge between two parts. We have measured a critical frequency that captured only in fiber-free part.

Defining coupling coefficients

One of the most important parts of current computer modelling is the generation of a map of anisotropic clusters, that reproduces main features of the real clusterized cardiac monolayer, such as: cluster size, anisotropy ratio in clusters and average coupling in the sample. First, we made a triangulation of a 2D sample with periodic boundary conditions. Thus, the characteristic size of the triangle determines a characteristic size of the domain. Then, we assign some random preferential direction (φ) to each network node. Therefore, we determine coupling coefficients matrix in all vertexes of a triangle as follows:

$$D = \begin{pmatrix} \lambda_1 \cos^2 \varphi + \lambda_2 \sin^2 \varphi & (\lambda_1 - \lambda_2) \sin \varphi \cos \varphi \\ (\lambda_1 - \lambda_2) \sin \varphi \cos \varphi & \lambda_1 \sin^2 \varphi + \lambda_2 \cos^2 \varphi \end{pmatrix},$$

where λ_1 and λ_2 are coupling coefficients along and across preferential direction.

Finally, we interpolate D within the triangle. Since two coefficients in D are equal, we can rewrite previous equation as

$$D = \begin{pmatrix} P & R \\ R & Q \end{pmatrix}$$

and interpolate (P, Q, R) . As a result of this operation, centers of the triangles will become less anisotropic, than nodes and edges (Figure 3.2). After adjustment of the parameters (distributions of λ_1 and λ_2 in Figure 3.3), we obtain a model of an excitable media relevant to the cells, clusterized on the nanofibrous net.

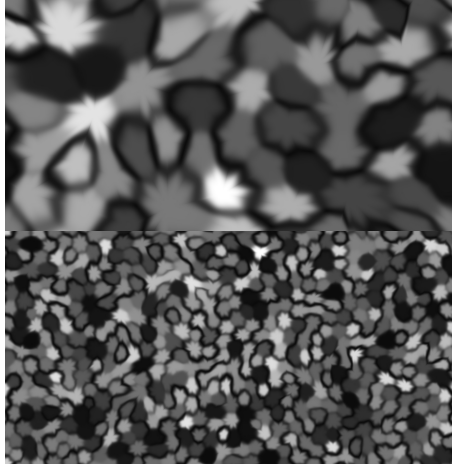


Figure 3.2: Anisotropy ratio (λ_1/λ_2) map with periodic boundary for different domain sizes. These maps were generated in computational studies using algorithm described in Section 4. As far as the interpolation has been done in (P, Q, R) space, some clusters are divided with low anisotropy areas (black) and in some neighbouring clusters the preferential direction was just rotated, without significant anisotropy change.

3.4.1 Electrophysiological simulation

After establishing different maps of $D(\vec{x})$ with various domain sizes, controlled by triangulation, we can find the dependence of excitation waves behavior on the frequency of stimulation. We found, that wave series demonstrate three different modes of propagation for the fixed domain size A) The frequency is too high: not all stimuli can give a rise to a wave according to refractory zone of the previous one. B) Waves are interacting by intersection with the refractory zone. Waves may break apart or even form spirals. C) The frequency is low. Waves are propagating almost independently, without any perturbations (Figure 3.4).

Results

Applying different rates of stimulation we determined the maximal captured frequency in the fiber-covered and fiber-free parts of the sample. The resulting graph is shown in Figure 3.5. We tested the range of domains 5–200 μm and

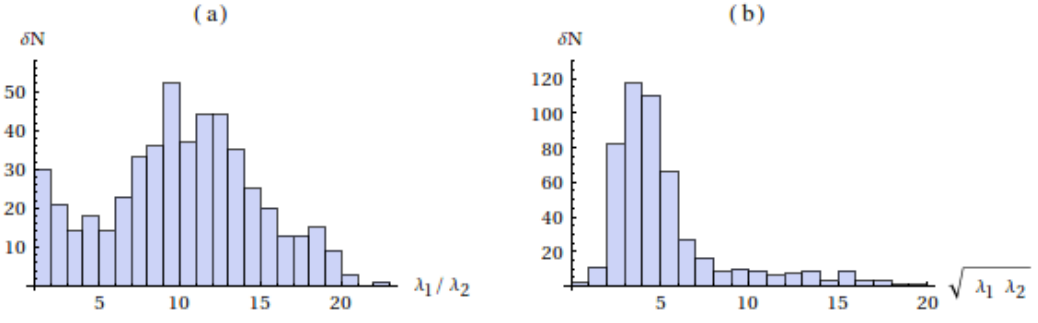


Figure 3.3: Distributions of (a) anisotropy ratio (λ_1/λ_2) and (b) average coupling ($\sqrt{\lambda_1\lambda_2}$).

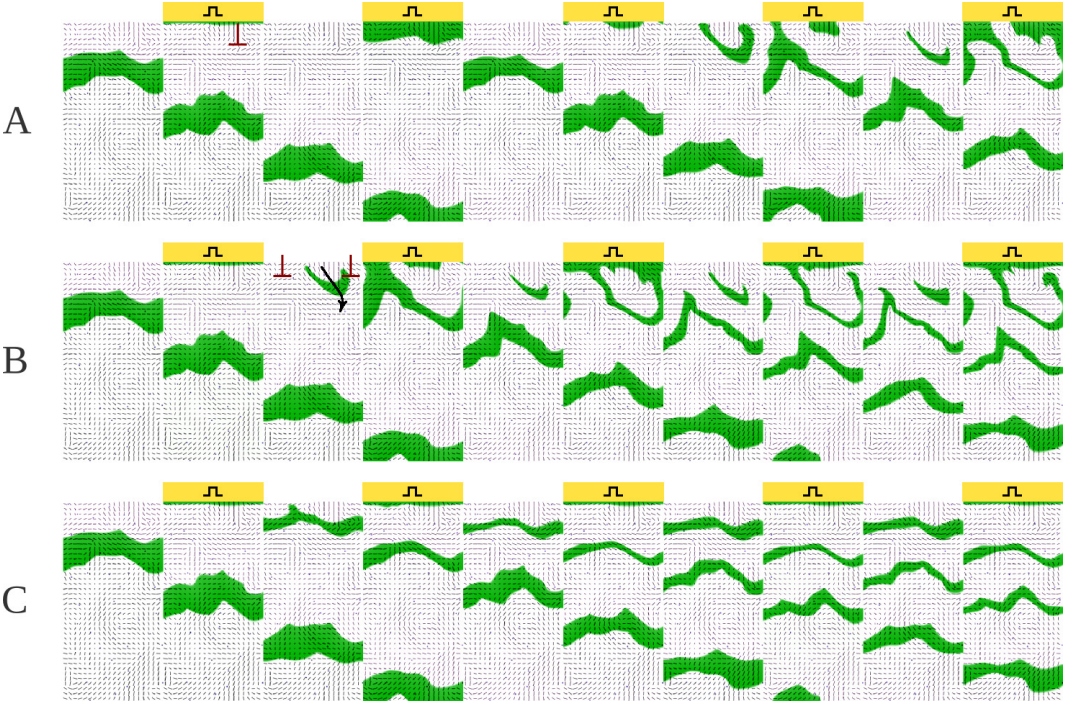


Figure 3.4: Modes of excitation waves propagation with different stimulation frequencies. The depolarized regions, where $u \neq 0$, are shown in grey. Stimulation was applied at the top borders of the samples at the moments of time marked with square pulse sign. A) The frequency is too high: not all stimuli can give a rise to a wave according to refractory zone of the previous one. B) Waves are interacting by intersection with the refractory zone. Waves may break apart or even form spirals. C) The frequency is low. Waves are propagating almost independently, without any perturbations.

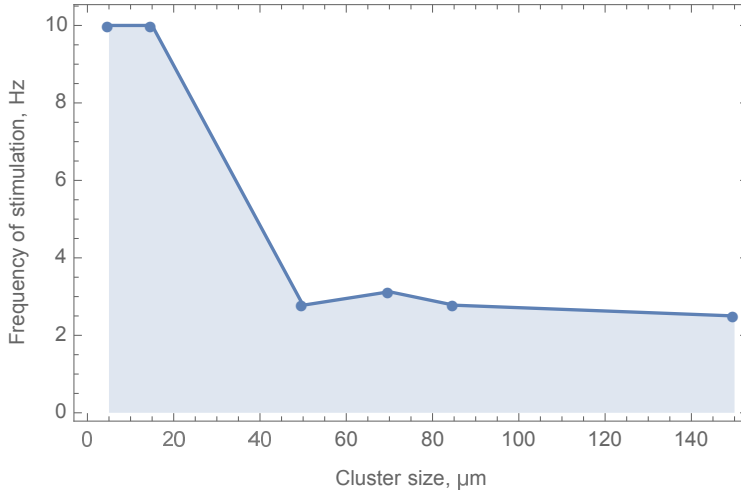


Figure 3.5: Critical frequency of stimulation for various domain sizes, measured in experiment.

found that larger domain sizes lead to the decrease of the critical frequencies. Thus, these results show that cardiac patches of varying morphology can behave in a different way in the host patient’s myocardium in the response to different pacing rhythms and when exceeding critical rate could be the possible sources of arrhythmias. We found the dependence of the critical frequencies on the size of the domains (Figure 3.6).

Conclusion

Our results show that in producing the scaffolds for the cardiac tissue engineering is very important to control the architecture of the electrospun nanofibrous mats in order to achieve less arrhythmogenic cardiac implants. The density of the deposited fibers may be calculated from the features of the propagating excitation waves, so that the resulting cells domains will be lower than the characteristic wavelength in the system.

Acknowledgements

The research was partially supported by Federal “5top100” Program.

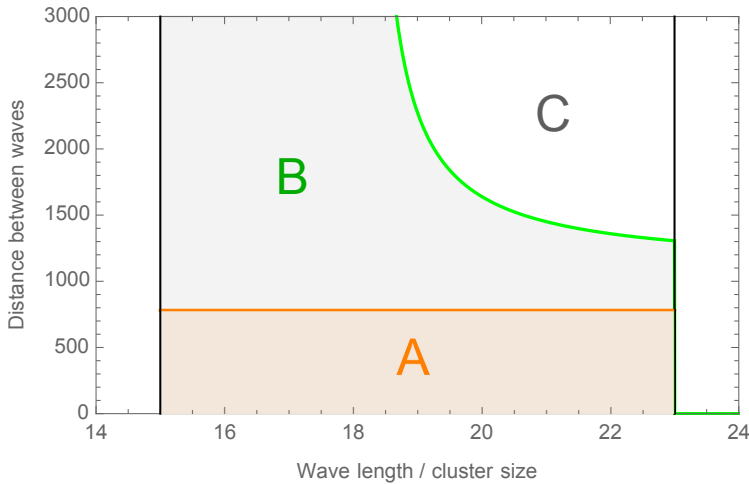


Figure 3.6: Critical distance between waves in a series for various domain sizes, obtained from simulation.

References

- [1] S. Heydarkhan-Hagvall, K. Schenke-Layland, A. P. Dhanasopon, *et al.*, “Three-dimensional electrospun ecm-based hybrid scaffolds for cardiovascular tissue engineering,” *Biomaterials*, vol. 29, no. 19, pp. 2907–2914, 2008.
- [2] M. Li, Y. Guo, Y. Wei, A. G. MacDiarmid, and P. I. Lelkes, “Electrospinning polyaniline-contained gelatin nanofibers for tissue engineering applications,” *Biomaterials*, vol. 27, no. 13, pp. 2705–2715, 2006.
- [3] J. L. Lowery, N. Datta, and G. C. Rutledge, “Effect of fiber diameter, pore size and seeding method on growth of human dermal fibroblasts in electrospun poly (ϵ -caprolactone) fibrous mats,” *Biomaterials*, vol. 31, no. 3, pp. 491–504, 2010.
- [4] Y. Orlova, N. Magome, L. Liu, Y. Chen, and K. Agladze, “Electrospun nanofibers as a tool for architecture control in engineered cardiac tissue.,” *Biomaterials*, vol. 32, pp. 5615–24, 2011.
- [5] N. Kudryashova, A. Teplenin, Y. Orlova, L. Selina, and K. Agladze, “Arrhythmogenic role of the border between two areas of cardiac cells alignment,” *Journal of Molecular and Cellular Cardiology*, 2014.
- [6] N. Bursac, Y. Loo, K. Leong, and L. Tung, “Novel anisotropic engineered cardiac tissues: studies of electrical propagation.,” *Biochemical and biophysical research communications*, vol. 361, pp. 847–53, 2007.

- [7] N. Bursac, “Cardiomyocyte Cultures With Controlled Macroscopic Anisotropy: A Model for Functional Electrophysiological Studies of Cardiac Muscle,” *Circulation Research*, vol. 91, pp. 45e–54, 2002.
- [8] K. Agladze, M. W. Kay, V. Krinsky, and N. Sarvazyan, “Interaction between spiral and paced waves in cardiac tissue,” *American Journal of Physiology-Heart and Circulatory Physiology*, vol. 293, no. 1, pp. H503–H513, 2007.
- [9] R. R. Aliev and A. V. Panfilov, “A simple two-variable model of cardiac excitation,” *Chaos, Solitons & Fractals*, vol. 7, pp. 293–301, 1996.
- [10] C. H. Luo and Y. Rudy, “A model of the ventricular cardiac action potential. depolarization, repolarization, and their interaction.,” *Circulation research*, vol. 68, no. 6, pp. 1501–1526, 1991.
- [11] C. H. Luo and Y. Rudy, “A dynamic model of the cardiac ventricular action potential. I. Simulations of ionic currents and concentration changes,” *Circulation Research*, vol. 74, pp. 1071–1096, 1994.
- [12] F. Fenton and A. Karma, “Vortex dynamics in three-dimensional continuous myocardium with fiber rotation: Filament instability and fibrillation,” *Chaos: An Interdisciplinary Journal of Nonlinear Science*, vol. 8, no. 1, pp. 20–47, 1998.
- [13] R. FitzHugh, “Mathematical models of threshold phenomena in the nerve membrane,” *The Bulletin of Mathematical Biophysics*, vol. 17, pp. 257–278, 1955.
- [14] J. Nagumo, S. Arimoto, and S. Yoshizawa, “An active pulse transmission line simulating nerve axon,” *Proceedings of the IRE*, vol. 117, no. m V, pp. 2061–2070, 1962.

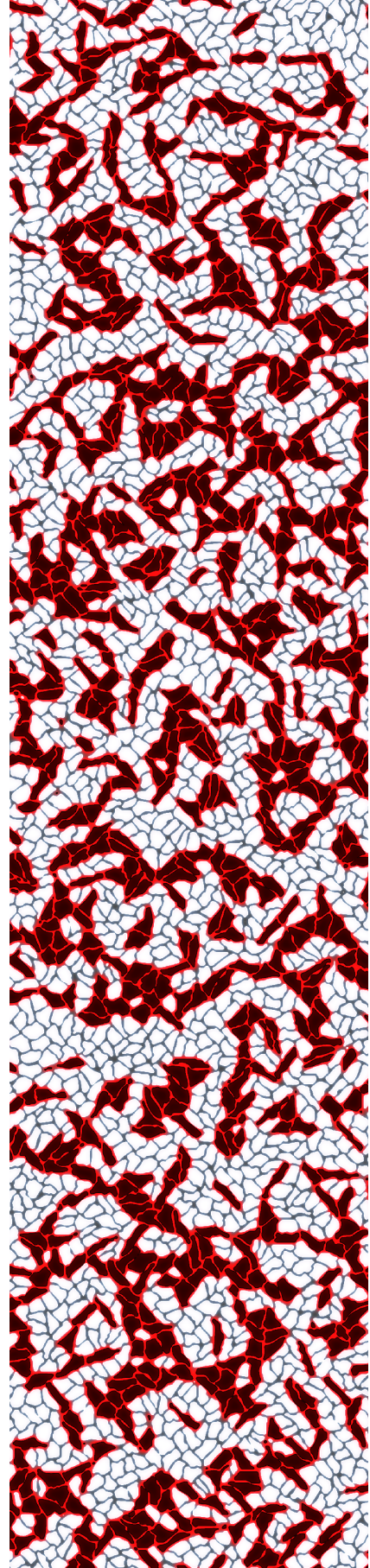
Chapter 4

Virtual cardiac monolayers for electrical wave propagation

N Kudryashova^{1,2}, V Tsvelaya¹, A V Panfilov², and
K Agladze¹

¹Moscow Institute of Physics and Technology, Dolgoprudny, Russia

²Department of Physics and Astronomy, Ghent University, Ghent, Belgium



Abstract

The complex structure of cardiac tissue is considered to be one of the main determinants of an arrhythmogenic substrate. This study is aimed at developing the first mathematical model to describe the formation of cardiac tissue, using a joint *in silico*–*in vitro* approach. First, we performed experiments under various conditions to carefully characterise the morphology of cardiac tissue in a culture of neonatal rat ventricular cells. We considered two cell types, namely, cardiomyocytes and fibroblasts. Next, we proposed a mathematical model, based on the Glazier-Graner-Hogeweg model, which is widely used in tissue growth studies. The resultant tissue morphology was coupled to the detailed electrophysiological Korhonen-Majumder model for neonatal rat ventricular cardiomyocytes, in order to study wave propagation. The simulated waves had the same anisotropy ratio and wavefront complexity as those in the experiment. Thus, we conclude that our approach allows us to reproduce the morphological and physiological properties of cardiac tissue.

Keywords: Cellular Potts Model, Glazier-Graner-Hogeweg model, cardiac tissue development, cardiac remodelling, cardiac arrhythmias

Published: Kudryashova, N., Tsvelaya, V., Agladze, K., & Panfilov, A.V. (2017). Virtual cardiac monolayers for electrical wave propagation. *Scientific Reports*, 7(1), 7887. <http://doi.org/10.1038/s41598-017-07653-3>

Introduction

Electrical waves of excitation propagate through the heart and initiate cardiac contraction. Abnormalities in wave propagation may result in cardiac arrhythmia. According to a report published by the World Health Organisation [1], cardiovascular diseases account for the highest number of deaths in the world, among which, around 40% occur suddenly and are caused by arrhythmias. Thus, understanding the principle of wave propagation is essential for decreasing cardiovascular mortality.

The electromechanical function of the heart is performed by excitable cells called cardiomyocytes (CMs), which are capable of generating an action potential, and, of mechanical contraction. In addition to CMs, cardiac tissue also contains other cells, the most abundant of these being fibroblasts (FBs). FBs are small inexcitable cells present in the heart in large numbers. Excess fibrous tissue, or fibrosis, can substantially affect wave propagation. In addition to FBs, there exist structural extracellular proteins (e.g. collagens), which form the extracellular matrix (ECM) and affect the CM phenotype [2]. The latter is essential for proper mechanical functioning of the heart [3] and for uninterrupted electrical signal propagation [4]. The interaction between CMs, FBs, and extracellular proteins results in the formation of a complex tissue texture. Such a texture changes substantially during most cardiac diseases, via a process called *remodelling*. Cardiac remodelling is considered to be one of the major determinants of arrhythmogenicity in cardiac tissue [5, 6]. However, gradual changes in tissue architecture that lead to remodelling are hidden from observation, and there exists no direct method to study it in patients [7]. Thus, an alternative approach to understand the principles of formation of normal and abnormal cardiac tissue, and, the possibility to predict their changes during remodelling, are of great interest.

The most logical way to approach this problem, is to represent knowledge about such processes in terms of a mathematical model of structural tissue formation. This model should be based on extensive experimental data, which can be used to explain the observed textures and to develop methods to control remodelling. Ideas related to the importance of such a model have been widely discussed in strategic papers on cardiac computer modelling [8, 9]. However,

this approach has not yet been realised. On the other hand, tissue growth models are extensively used in developmental biology. One of the most advanced approaches in this field is the Cellular Potts Model approach, or, in particular, the Glazier-Graner-Hogeweg (GGH) model [10–12]. Various processes of cell- and tissue morphogenesis, e.g, the process of root growth [13], angiogenesis [14], stem cell differentiation [15], morphogenesis of *Dictyostelium discoideum* [16], epidermal formation [17] and vascular system development [18], etc. have been described using this model.

The aim of this study is to introduce GGH models to the field of cardiac research and to develop a detailed tissue formation model for cardiac tissue. We develop this model for a classical experimental model system — cardiac cell culture [19]. Such cultures are widely used in stem cell- [20–22] and regenerative medicine research, as they can be expected to reproduce architectural properties close to those of real cardiac tissue. In addition, cell cultures provide a valuable tool to study the mechanisms of cardiac arrhythmias, especially rotors [23]. We are mainly interested in cells cultured on nanofibrous substrates that resemble the ECM of the heart. If these nanofibres are aligned, the tissue obtains structural and functional anisotropy [24], which is one of the main factors affecting wave propagation in the heart. This nanofibre-based experimental system is ideal for our purpose, because here, the electrical properties of the cardiac cultures are closely related to their morphology. Such a system can be directly monitored with optical recordings [23] that facilitate validation of the model at each step of its development. Therefore, we have developed GGH models for this particular experimental model.

Our paper is organised as follows. In the first section of the Results, we describe the experimental model for cardiac tissue formation and specify the cell shape acquisition procedure. In the second section, we focus on the mathematical GGH-type model for cardiac tissue, provide validated coefficients for the model and demonstrate its capabilities. In the third section, we demonstrate wave propagation patterns in isotropic and anisotropic samples. Next, we discuss our results in relation to other cell-based discrete models and available experimental data, and possible future work in this direction. Finally, we provide a detailed description of the methods and algorithms used in our study.

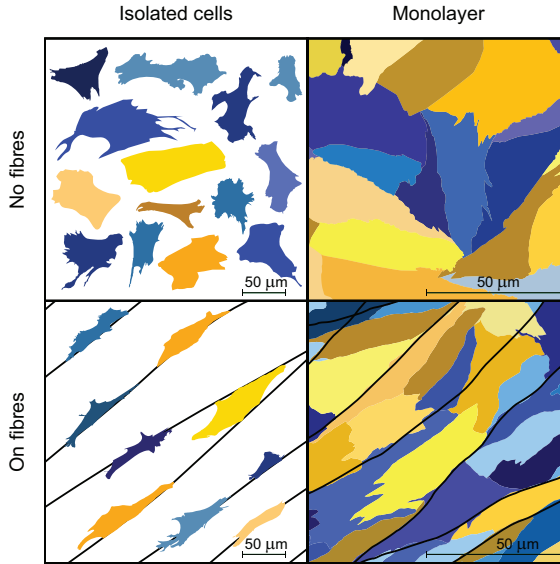


Figure 4.1: **Experimental cases considered in our study.** The first column shows isolated cells seeded at a low density to avoid cell-cell interaction. The second column represents cells in the monolayer. The substrate was isotropic in the upper row, whereas in the second row, nanofibres were added. Cardiomyocytes are shown in yellow tints, whereas fibroblasts are shown in blue tints. This image was based on immunohistochemical data but was refined for illustrative purpose.

Taken together, we show that GGH models can quantitatively reproduce cardiac cell shapes, explain their elongation along a fibrous substrate and reproduce the experimental data. We conclude that it is a valuable tool for studying the connection between the morphology and function of cardiac tissue.

Results

4.2.1 Experimental study of cell shapes in cardiac tissue

Simplified cases of cardiac morphogenesis. In computational studies, we reproduced the experimental setting of neonatal rat cells cultured on a polymer nanofibrous scaffold. Cell cultures grown on such an artificial ECM, which imitates the ECM of the heart, effectively reproduce the anisotropy of

cardiac tissue [24]. This engineered cardiac tissue has a complex structure resulting from cell–cell and cell–substrate interactions. During model development, we also considered simpler experimental situations that prevented cell–cell or cell–nanofibre interaction. To achieve this experimentally, we seeded the cells at a low density so that they could not touch one another. We also used a uniform scaffold without fibres, in which the cells spread equally in all directions.

As a result, we reproduced in an experiment, the following four different conditions: non-interacting cells with and without polymer nanofibres and monolayers with and without polymer nanofibres (see Fig. 4.1). Here, CMs and FBs are shown in different shades of yellow and blue, respectively. Finally, we developed a procedure for cell shape analysis, which we used to validate our mathematical model.

Identification of cell shapes in the experiment. We stained cell cultures with DAPI (DNA, blue), phalloidin (F-actin, green) and monoclonal anti- α -actinin antibody (α -actinin, red). From the α -actinin image, we were able to discriminate CMs from FBs (see Fig. 4.2). We used F-actin staining images for cell shape acquisition, and DAPI, for cell counting. Details of the cell shape acquisition procedure and further analysis can be found in Section 4.4.5. After the procedure, we collected the database of cell shapes for each of the four conditions that we studied.

We developed a custom code (in Wolfram Mathematica) for cell shape analysis (for details, see the Methods section 4.4.5). Using this code, we tested many standard morphological parameters and found the most valuable ones for the validation of the mathematical model. These parameters are cell spreading area, elongation, convex coverage, real number of focal adhesions (“protrusions”) and number of pronounced convexes of the cell periphery (“convexes”) for 2.5 μm resolution (for details, see Section 4.4.5).

Using this approach, we collected the data from 103 isolated cells on a uniform substrate, 77 isolated cells on fibres, 127 cells in the isotropic monolayer and 294 cells in monolayers on fibres.

Most of the cells were classified as CMs or FBs according to the level of α -actinin expression and actin cytoskeleton development. Some cells with

Table 4.1: Cell shape characteristics measured in the experiment.

	Isolated cells		Monolayer		
	CM	FB	CM	FB	
	$n = 36$	$n = 45$	$n = 67$	$n = 53$	
Area ($\cdot 10^3 \mu m^2$)	2.5 ± 1.0	2.1 ± 1.0	1.0 ± 0.4	0.9 ± 0.3	No fibres
Convex Coverage	$84 \pm 9\%$	$66 \pm 11\%$	$79 \pm 11\%$	$70 \pm 10\%$	
Elongation	1.7 ± 0.8	1.7 ± 0.6	2.1 ± 0.8	2.0 ± 0.8	
Protrusions ($1 \mu m$)	13.1 ± 5.8	16.1 ± 5.7	7.6 ± 3.2	8.2 ± 3.3	
Convexes ($2.5 \mu m$)	5.3 ± 1.5	6.4 ± 2.4	3.3 ± 1.3	4.0 ± 1.3	
	$n = 32$	$n = 40$	$n = 34$	$n = 27$	
Area ($\cdot 10^3 \mu m^2$)	1.4 ± 0.8	1.3 ± 0.8	0.6 ± 0.2	0.6 ± 0.2	On fibres
Convex Coverage	$80 \pm 9\%$	$63 \pm 12\%$	$81 \pm 9\%$	$60 \pm 13\%$	
Elongation	3.0 ± 1.4	2.2 ± 1.4	3.2 ± 0.9	2.6 ± 1.0	
Protrusions ($1 \mu m$)	6.8 ± 3.9	12.6 ± 6.0	4.6 ± 2.5	5.8 ± 2.3	
Convexes ($2.5 \mu m$)	2.8 ± 1.6	4.8 ± 2.5	2.4 ± 1.2	3.1 ± 1.6	

controversial characteristics (for example, α -actinin positive, but without developed cytoskeleton) were rejected. All measured parameters and statistics for the classified cells are presented in Table 4.1. These parameters serve as an important dataset to verify and tune our model.

One interesting observation is that some CMs can be distinguished from FBs, on the sole basis of cell shape, even in the absence of staining. The most important parameter for types specification is the convex hull coverage, which is the ratio of cell spreading area to the area of its convex hull. CMs normally occupy around 80% of a convex hull, whereas FBs cover only 60%–70%, and have much deeper concaves. Fig. 4.2 shows the distributions for the convex coverage of CMs and FBs. A substantial difference exists between the convex coverage of these two types of cells. Statistically, CMs and FBs have a considerably different median convex coverage ($p\text{-value} < 10^{-3}$, $n_{\text{CMs}} = 36$, $n_{\text{FBs}} = 45$) (see Fig. 4.2g). No CMs with convex coverage lower than 60%, and no FBs with convex coverage higher than 90%, were observed in experiment. Therefore, for 40% of FBs and for 30% of CMs, the cell type could be determined, relying only on the cell shape.

It is well known, that FBs have 15-30 times smaller volume than CMs [25, 26]. However, in cardiac monolayers (shown in Fig. 4.1) FBs occupy almost the same area as CMs. In our cell cultures, the height of the cells measured with the

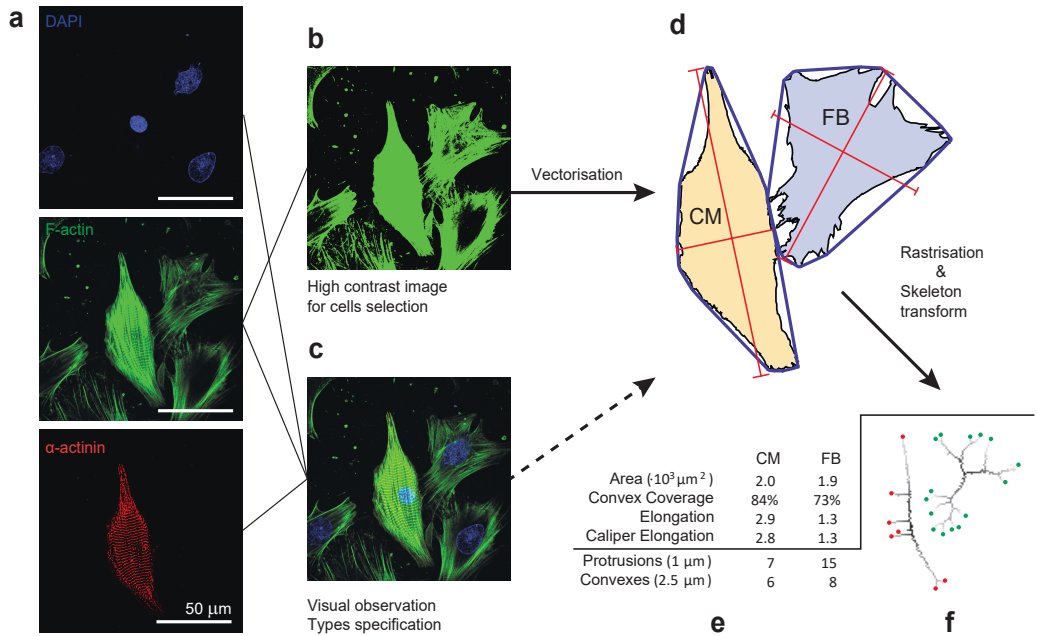


Figure 4.2: **Algorithm for cell shape analysis in the experiments.** Cardiac cells were observed experimentally with the use of immunohistochemical techniques. Panel (a) shows raw data on cells stained with DAPI (DNA, blue), phalloidin (F-actin, green) and monoclonal anti- α -actinin antibody (α -actinin, red). Sub-figures (b) and (c) show the processed data used for cell contour selection and cell type classification. In (b), the contrast of F-actin staining was enhanced for cell contour selection. In (c), three channels were merged to obtain better cell representation for classification (cardiomyocyte vs. fibroblast). Sub-figure (d) shows the cell images obtained after segmentation. The convex hull is shown as a blue line around each cell. These images were used to obtain parameters such as area, convex hull coverage and elongations. Cell images were then rasterised with two resolutions (1 μm and 2.5 μm), and skeleton transform was applied (f). The number of skeleton endpoints at a high resolution was considered as the number of protrusions. All the measured parameters are listed in (e). For details, see section 4.4.5. (g) **Distribution of the convex coverage for two cell types.** CM—cardiomyocyte ($n = 36$), FB—fibroblast ($n = 45$). The histogram shows that FBs cover a much smaller area within the convex hull than CMs. The cell shapes of the median samples in the experimental database are shown on the right.

confocal microscope was approximately $1\ \mu\text{m}$ for the FBs (everywhere, except for the nuclei), and $7\ \mu\text{m}$ for the CMs. Therefore, the volumes of the cells in two-dimensional cell cultures are still similar to those in three dimensions. The resulting spreading area is almost the same due to difference in spreading.

We also found that the cell area changes depending on the conditions involved. Cells in monolayers tend to be smaller than those that are isolated from one another. This is caused by the lateral pressure from the cells in monolayers, constraining planar spreading and pushing of cells into the third dimension. To reproduce this effect in our 2D study, we assigned different target areas to cells that were exposed to different conditions. The collected cell shape data were used for the development and validation of our model.

4.2.2 Mathematical model

Mathematical model statements. Our imaging studies clearly show that both CMs and FBs have a characteristic polygonal shape. Several studies explain the origin of such shapes as complex biophysical processes, which include formation–destruction of the attachments at the cell boundary, actin polymerisation and the subsequent migration of the cell body [27]. To describe such processes, we proposed the use of the Cellular Potts Model. More specifically, we used its extended version, which is the GGH model [10–12], as it is widely applied to reproduce correct cell shapes [28, 29] and their dynamics [30–32] in many morphogenetic processes. Our model proffers new rules for the formation and retraction of adhesion sites. We introduced a Hamiltonian with elastic, adhesive and stretching forces, while taking into account the proper description of the interaction between different types of cells and cells with a nanofibrous scaffold. The details of our approach are given below and in the methods section.

Basic GGH model. In GGH modelling (Glazier and Graner, 1992 [10]; Graner and Glazier, 1993 [11], Hogeweg, 1997 [12]), cells are represented as a cluster of subcells (see Fig. 4.3) in a regular lattice. Lattice representation allows researchers to efficiently reproduce shapes of the real cells and structures of real tissues. In a basic model, cells maintain their volume and interact with

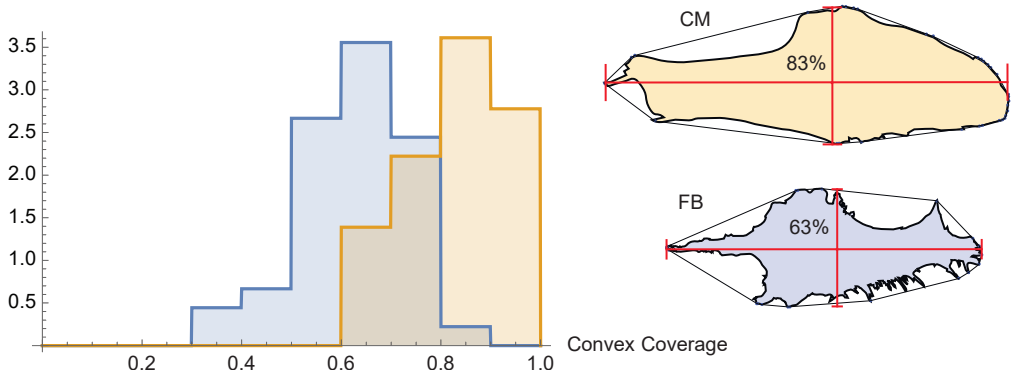


Figure 4.3: **Cells representation in GGH model.** Cells of type A are shown in yellow and of type B — in blue. Media around the cells is shown in white and denoted in the model with zero index. Cells interact via adhesion with the surface energy J . This energy depends on the cell types involved (shown in different colours and with different indexes).

each other via type-specific adhesion which is expressed in terms of the total energy of the system. The strongest part of GGH models is that this energy can be extended with the extra terms to include new forces or fields. The main idea is that cell is allowed to change its shape to minimise the total energy. The process of energy minimization is performed in a way, that it describes not only the static morphology of the cells but also their motility [33].

Each cell is allowed to change its shape to minimize the prescribed energy. At each time step one of the subcells in a lattice is selected. This subcell attempts to copy itself to a neighbouring position. If this change leads to the decrease of the total energy, it will be accepted. Otherwise, the copy attempts with smaller energy increase are accepted with a higher probability.

This energy-based approach reproduces many static and dynamic cell properties including cells proliferation and migration. Moreover, new phenomena, such as, for example, chemotaxis, could be easily included in a model as a new term in the total energy. In our study, we extended the total energy with the term, that describes cell spreading.

The implementation of GGH is normally organised as follows. Index 0 indicates the *medium*, and positive indices designate individual cells. In our model, we consider two cell types. Thus, τ has three possible values: 0 (medium), 1 (CM) or 2 (FB).

Cell formation is defined by the Hamiltonian of GGH, which has the following form:

$$H = H_{\text{adhesive}} + H_{\text{elastic}} = \sum_{\substack{(\vec{i}, \vec{j}) \\ \text{neighbours}}} J_{\tau_{\sigma_i}, \tau_{\sigma_j}} (1 - \delta(\sigma_i, \sigma_j)) + \sum_{\sigma} \lambda_{\tau_{\sigma}} (v_{\sigma} - V_{\tau_{\sigma}}^t)^2 \quad (4.1)$$

where i is summed over all lattice points or subcells, σ_i is the index assigned to the i^{th} subcell and τ_{σ} is a type of cell with index σ . J is the adhesion energy between cells with indexes σ_i and σ_j of types τ_{σ_i} and τ_{σ_j} , and δ is a Kronecker delta function. In the second term λ is the elasticity coefficient and $V_{\tau_{\sigma_i}}^t$ is the target volume that the cell σ_i maintains. The balance between these two energies determines the curvature of the concave parts of the cell [29]. To simulate the convex parts (or the protrusions), this expression was further extended.

The first two terms in (4.2) comprise the minimal GGH model, in which, the cells only maintain the target volume and interact via adhesion.

We describe cellular motility by using the iterative Markov chain Monte Carlo (MCMC) algorithm, which attempts to copy an index to a randomly selected lattice point \vec{i}_t from a random neighbouring cell \vec{i}_s . We calculate the change in Hamiltonian for this copy ΔH , and the new state is accepted with a probability:

$$p = \begin{cases} 1 & \text{if } \Delta \mathcal{H} \leq 0, \\ e^{-\frac{\Delta H}{T}} & \text{if } \Delta \mathcal{H} > 0, \end{cases}$$

where T corresponds to motility of the cells. In each Monte-Carlo step (MCS) we perform N copy attempts, where N is the total number of subcells of the lattice.

The resulting dynamic cell movements mimic the motility and spreading of cells. Questions regarding the time course in the model are addressed in Glazier et al. review [33].

Equations and parameters. In our formulation of the GGH model, cell formation is defined by the following Hamiltonian:

$$H = H_{\text{adhesive}} + H_{\text{elastic}} + H_{\text{protr}} + H_{\text{nuclei}}, \quad (4.2)$$

H_{protr} in (4.2) is an important new term that we introduced in our model to describe the protrusion at the attachment sites. Protrusion is a very complex biomechanical process that involves attachment, actin polymerisation and biochemical regulation of tension and assembly/disassembly of the actin cytoskeleton. These adhesion sites protrude further and further from the cell body, expanding as much as possible up to a certain length until they suddenly break apart and retract. This sequence of events can be clearly seen in video 7 in Doyle et al. [34]. To describe this protrusion process, we assume that the adhesion site repels from the centre of the cell and that the cells can detach from the substrate with some penalty in energy (P_{detach}).

We suppose that the cell has a limited number of adhesion sites with protrusive activity (N_{protr}); all of these repel from the centre of mass (cm). For spreading on the isotropic substrate, we used the simplest possible potential field (H_{protr}) to describe the expansion of the cell at the attachment sites.

$$H_{\text{protr}} = \sum_{\substack{\vec{i} \\ \text{focal contacts}}} \frac{G_{\tau_{\sigma_i}}}{\rho(\vec{i}, \vec{\text{cm}}_{\sigma_i})} + \sum_{\substack{\vec{i} \\ \text{focal contacts} \\ \text{detach from substrate}}} P_{\text{detach}}, \quad (4.3)$$

where $G_{\tau_{\sigma_i}}$ is the type-dependent constant regulating the amplitude of the protrusion force, and $\rho(\vec{i}, \vec{\text{cm}}_{\sigma_i})$ is the distance between the currently tested subcell i and the centre of mass of the cell. We have chosen the potential as $1/\rho$, which results in an expansion force that is strong close to the cell, but that decreases with increase in distance from the cell. At some distance, it is balanced by the elasticity term. We found that this representation produces a polygonal form with concave-free arcs in between protrusions (see the discussion related to Fig. 4.4 later in the text).

Further modifications were needed for the cell–fibre interaction. The fibres in our model occupy some subcells of the mesh and have an assigned orientation. The cells produce internal forces by constructing actin stress fibres from a focal contact towards the cell body. The stronger the response from the scaffold, the more the production of actin filaments, and the higher the total force applied by the cell to the substrate [35, 36]. Assuming that the polymer nanofibres produce a mechanical reaction force only in the direction along them, the energy term for cell–substrate interaction (4.3) becomes as

follows:

$$\begin{aligned}
 H_{\text{protr}} = & \sum_{\substack{\vec{i} \\ \text{focal contacts} \\ \text{with isotropic substrate}}} \frac{G_{\tau_{\sigma_i}}}{\rho(\vec{i}, \widehat{\text{cm}}_{\sigma_i})} + \\
 & + \sum_{\substack{\vec{i} \\ \text{focal contacts} \\ \text{with nanofibers} \\ \text{when on nanofiber}}} \frac{G_{\tau_{\sigma_i}}}{\rho(\vec{i}, \widehat{\text{cm}}_{\sigma_i})} \cos^{-1} \left(\varphi_{f_i} - (\widehat{\vec{i}, \text{cm}}_{\sigma_i}) \right) + \\
 & + \sum_{\substack{\vec{i} \\ \text{focal contacts} \\ \text{detach from substrate}}} P_{\text{detach}} + \sum_{\substack{\vec{i} \\ \text{focal contacts} \\ \text{from nanofiber}}} P_{\text{unleash}}, \quad (4.4)
 \end{aligned}$$

where for movements along the fibres, the projection of the force to the nanofibre is considered and $\cos^{-1}(x)$ denotes $1/\cos(x)$. Given that the cell builds up new actin filaments to counteract the tension along the nanofibre, the projection of the distance $r \cos(\alpha)$ instead of the distance r itself was used (see Section 4.4.6 for more details). $(\widehat{\vec{i}, \text{cm}}_{\sigma_i})$ denotes the direction of the vector from the centre of mass cm_{σ_i} to the currently examined subcell \vec{i} . The difference between this direction and fibre direction (α in the description above) is used for projection calculation.

To describe the interaction of the attachment sites with the nanofibre, we assume that movements from the isotropic substrate to the fibre require no energy change. In our experiments, we covered the isotropic and anisotropic monolayers with the same fibronectin solution, so that integrins at the cell surface bound to the fibronectin the same way. Therefore, we conclude, that there is no difference in adhesive properties between the nanofibres and the isotropic substrate. However, for movements from the fibre back to the isotropic substrate, we apply the penalty P_{unleash} . It is required because our experimental observations show that the cell builds up actin filaments during motion along the nanofibres. These filaments have to be aligned with the nanofibres. However, the motion from the fibre back to the isotropic surface is the motion aside from that in the actin filament direction that should be performed by a stress fibre not aligned with the nanofibre. Thus, such motion is energetically unfavourable in terms of our model. As a result, cell elongation occurs because

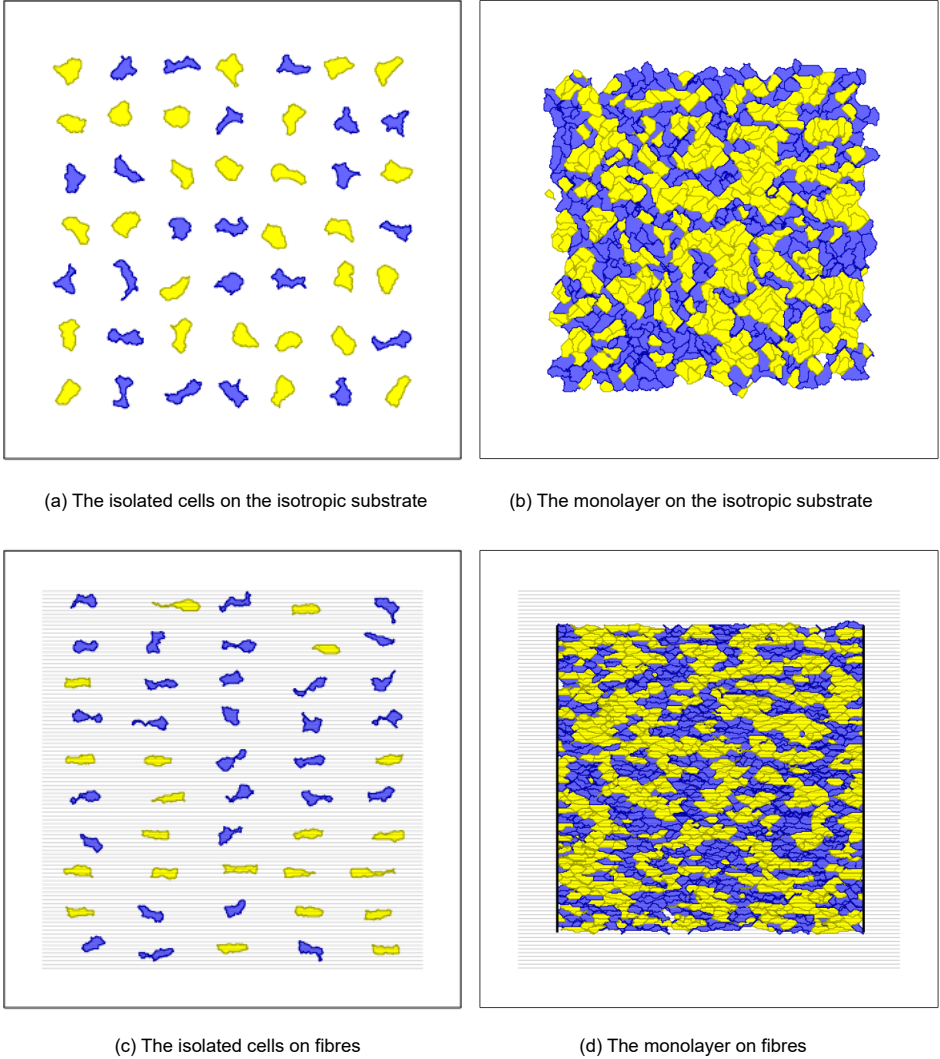


Figure 4.4: **Examples of simulations for four seeding conditions.** Cardiomyocytes are shown in yellow tints, whereas fibroblasts are shown in blue tints. Here the proportions of the cells of each type were 50%. Black lines in (d) show the borders that constrain the anisotropic monolayer. In (c) and (d), grey horizontal lines show nanofibres.

of actin strand reassembly, which is controlled by the direction-dependent mechanical reaction of the substrate. However, the same forces also create direction-dependent motility, which impose constraints on the monolayer from the sides because of the high motility along the fibres.

One more penalty term exists in our model:

$$H_{\text{nuclei}} = \sum_i P_N$$

for the invasion of the media (index 0) or the other cell deep into the current cell. We assume that the cell nucleus and the surrounding area have a higher stiffness than the remaining cell body. This penalty term P_N has a non-zero value for the medium subcells close to the nucleus.

Finally, three more rules for copy attempts in our model are not present in the energy equation. The copy is forbidden in three cases: if, as a result, a cell disappears; if the connectivity of the cell breaks; or if the protrusion spreads further than L_{MAX} from the cm.

The resulting model is described in detail in section 4.4.6.

Model validation. For each of the four conditions described above, we identified the best set of parameters that fit the experimental shape features. All the parameters for the model are listed in Table 4.2. The shape characteristics are compared with those in the experimental results in Fig. 4.5. One can see that most characteristics of the isolated cells almost precisely match the experimental data, except for a number of protrusion sites on the cell periphery. This number was slightly fewer in the simulations but was within the variability of the experimental measurements. For the CMs in monolayers, both with or without fibres, there was also some divergence in elongation, which stays within the deviations in the experiments.

Although the average values in the model and in the experiment are in good agreement, there is a substantial difference in the variability of most of the shape parameters: the variability in the experiments exceeds that in the simulations. The main reason is the homogeneity of the cell population considered. However, in the experimental samples, even adjacent cells may have different basic parameters, such as exclusive volume and generation of protrusion force. This discrepancy can be overcome by shifting beyond a single parameter set paradigm and applying the approach of experimentally calibrated populations of models; this approach is now under development in cardiac electrophysiology [37, 38]. However, in the first step, we decided not to include cell

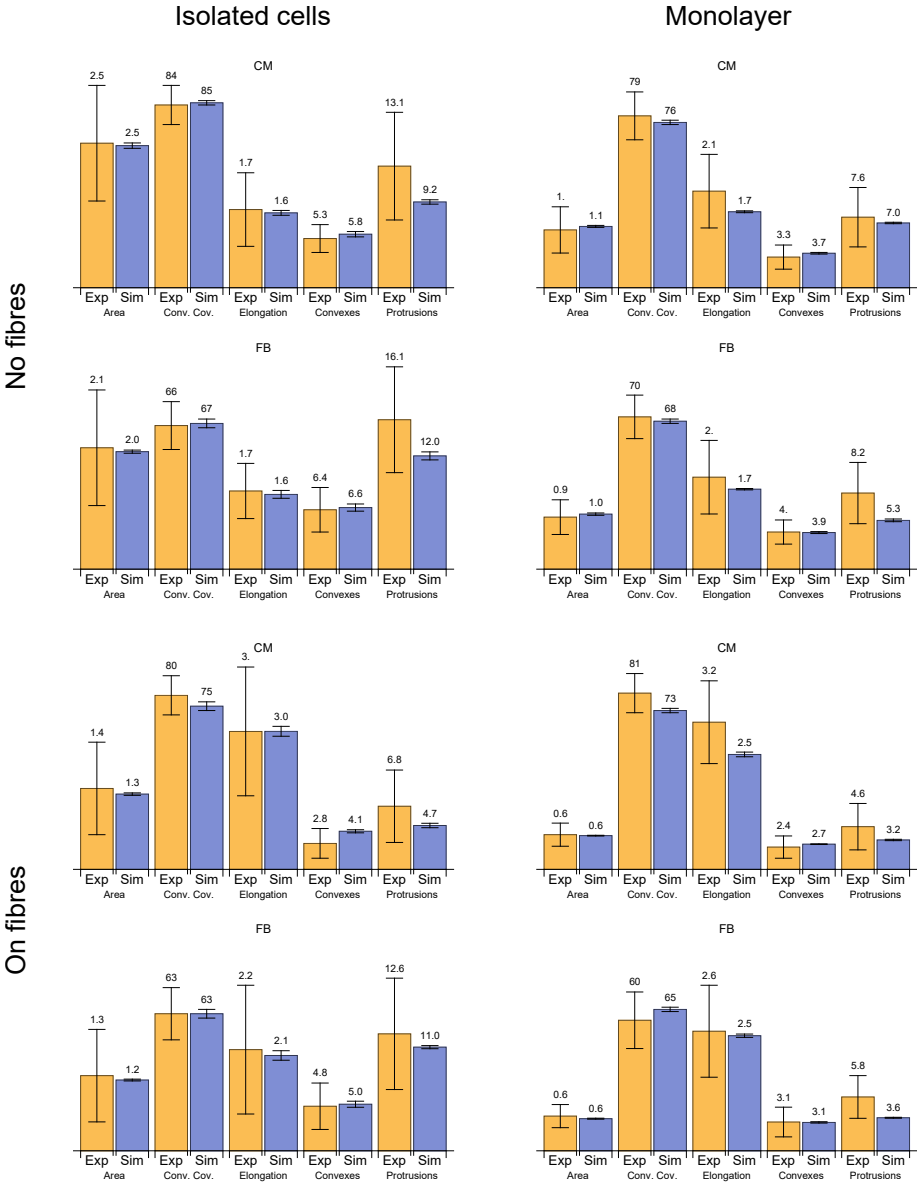


Figure 4.5: **Comparison of the parameters in the experiment and the simulation.** Yellow bars show experimental values, whereas the blue ones show computed values. The amount of cells studied in experiment and considered in this statistics are listed in Table 4.1, in simulations — in Table 4.2. Error bars indicate standard deviations.

Table 4.2: Parameters of the model

Parameter	Units	No fibres				On fibres			
		Isolated cells		Monolayer		Isolated cells		Monolayer	
		CM	FB	CM	FB	CM	FB	CM	FB
Temperature T	1.0	1.0		1.0		1.0		1.0	
G_N	mm	47.48	26.81	51.03	5.09	238.22	9.62	461.36	233.76
V_t	$\cdot 10^3 \mu\text{m}^2$	2.11	1.39	0.88	0.79	1.34	0.93	0.6	0.35
λ	mm^{-4}	151.37	70.71	62.32	17.91	69.88	68.05	26.42	14.24
P_{detach}		9.89	12.3	30.93	11.22	16.16	15.2	155.62	53.21
$J_{\text{Cell-MD}}$		427.82	306.96	1013.93	445.77	474.19	305.8	937.13	560.27
$J_{\text{Cell-Cell}}$	mm^{-1}	—	—	798.73	473.28	—	—	631.42	267.25
$J_{\text{CM-FB}}$		—	—	949.22		—		1152.05	
P_{unleash}		—	—	—	—	28.15	1.44	117.94	66.93
L_{MAX}	μm	66.64	76.7	81.41	73.62	42.31	48.72	62.37	65.05
N_{protr} (fixed)		21	24	12	13	10	22	8	9
Sample dim.	$\text{mm} \times \text{mm}$	1.0×1.0		0.8×0.8		1.0×1.0		0.8×0.8	
Simulation time	MCS	900		2000		2000		3000	
Number of cells	1	7×7		26×26		5×10		17×68	

variability. Overall, we conclude that our model has a good correspondence with the properties of the average cell measured in the experiment.

The resulting computed shapes of the cells for each of the cases are shown in Fig. 4.4. Visually, the shapes also correspond well with the experimental data, apart from the agreement found in the statistical evaluation.

4.2.3 Wave propagation in isotropic and anisotropic samples with fibrosis

Using the developed morphological models, we further studied wave propagation in fibrotic tissue. Here, we aimed to reproduce such properties of the experimental tissue as velocity, anisotropy and wavefront complexity. We tested wave propagation in isotropic and anisotropic virtual tissue and compared the results with those of the optical mapping of the experimental cardiac monolayers.

Initially, we measured the concentration of FBs in the experimental sample by using immunohistochemical data. Next, this number was used for virtual tissue generation with our GGH model. Finally, for the wave propagation simulations, we applied a monodomain ionic model of neonatal rat ventricular CM, developed by R. Majumder in 2016 [39]. This model is a modification of the Kohronen model with simplified calcium dynamics. We used the mesh generated by our GGH model for our electrophysiological simulations. Different coupling coefficients were assigned to propagation along the cell, end-to-end and side-to-side signal transmission between the cells. The difference between end-to-end and side-to-side connections was related to the uniform GJs and ionic channels distribution along the cell membrane. These coefficients were adjusted to fit the experimental velocities.

Figure 4.6 shows the activation maps for the experimental samples (left) and simulations (right). The yellow star indicates the place where the stimulations were applied, and the white arrow shows the nanofibre orientation. The arrival time is colour coded. One can see that both in the experiment and the simulation, the wavefronts have a similar shape complexity.

In isotropic tissue (without nanofibers) on the large scale, the velocity ratio was always 1 regardless of cell elongation and non-uniform channels distribution along the cell membrane. In the presence of nanofibres, we observed

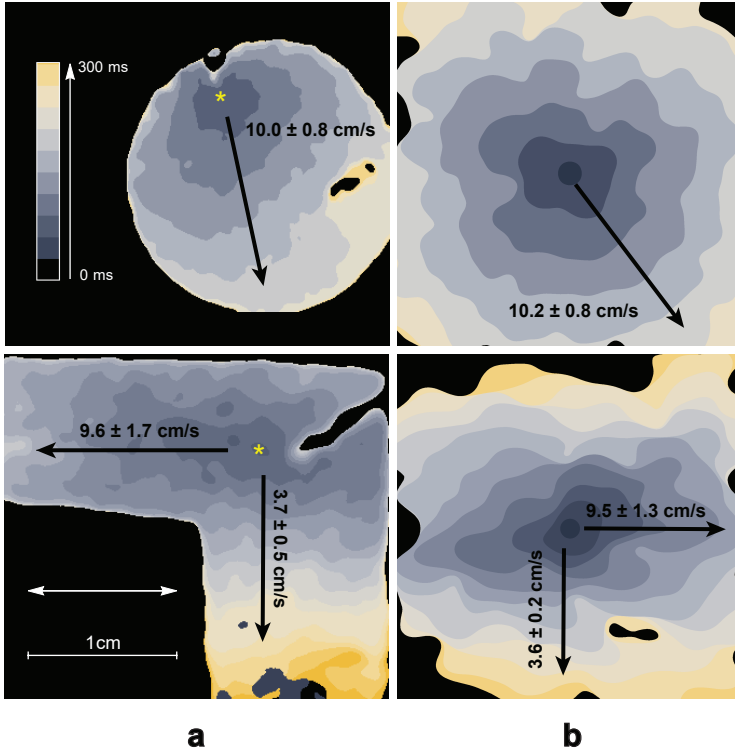


Figure 4.6: **Experimental results acquired with the optical mapping of isotropic and anisotropic samples compared to simulated ones.** (a) Activation maps for the isotropic sample (upper image) and the anisotropic sample on nanofibers (lower image). The yellow star shows the place where stimulation with an electrode was applied. The white arrow shows the preferred direction of the fibres in the sample. Activation time is colour coded (0 – 300 ms). (b) Corresponding simulations of the wave propagation in samples with 30% and 35% FBs in isotropic and anisotropic samples, respectively. The same filters with the same kernel size were applied to the simulated data, as for the experimental data in column (a). Corresponding video files and extended version of this figure could be found in Supplementary Materials.

anisotropy. To measure the anisotropy more precisely, we prepared L-shaped experimental samples. These samples were covered with nanofibres aligned along one of the arms of the L. We stimulated the corner of the L-sample and measured the longitudinal and transversal velocities in the corresponding arms. This shape of the sample allowed us to avoid the effects of curvature on wavefront velocity. The measured velocity ratio for the anisotropic samples

varied between 1.4 and 2.6 (in 8 samples, where 5 samples were made of the cells from one isolation). In figure 4.6 the sample with the highest anisotropy ratio is shown.

In the simulations with 35% of FBs, the velocity ratio stayed within a range between 1.5 and 2.7 depending on the parameters of the electrophysiological model. This range was determined by tissue morphology and was similar to the observed range of anisotropy ratios in experimental samples. Both in simulation and experiment, zig-zag propagation occurred along the transversal direction. This can be seen in the activation map: there are regions with the vertical wavefront direction, perpendicular to the overall propagation direction. The corresponding video of wave propagation could be found in Supplementary Material. This zigzag propagation resulted in high anisotropy ratio.

Taken together, using our approach, we reproduced the proper anisotropy for the samples on nanofibres, as well as a similar wave complexity for the wavefronts both in isotropic and anisotropic cases. Therefore, we have shown that our morphology-based model provides a detailed and accurate description of wave propagation and captures wavefront complexity.

Discussion

The morphology of cardiac tissue significantly influences its function. It is well known, for example, that with ageing, CMs become larger, and the number of FBs increases, filling the interstitial spaces between CM bundles. The conduction velocity then decreases, and the functional anisotropy increases [40], resulting in a proarrhythmic substrate. Thus, understanding the connection between these functional and morphological changes is important.

In this study, we developed a powerful tool to study the relation between morphology and electrical wave propagation in cardiac monolayers. Using our approach, we demonstrated the possibility to accurately reproduce cell shapes under various conditions, functional anisotropy and complexity of the wavefronts. We collected a database of cell shapes under different conditions: low density seeding, high density seeding, monolayers with and without nanofibres. We selected and measured the characteristic parameters for these shapes and found that FBs can be recognised in cardiac tissue by their shape alone. This

is due to the fact that FBs tend to have regions of deeper concavity on the cell boundary than CMs. We proposed a model to describe these features and adjusted to fit experimental data. Our model is based on the GGH model [10–12], which is widely used in tissue growth studies. After adjustments, our model could accurately reproduce cell shape parameters in four studied cases. Interestingly, the virtual cells on the isotropic substrate exhibited a slight elongation to the ratio of 1.7. Furthermore, our model does not include mechanisms for cell polarisation. Any observed polarisation was solely caused by the process of cell spreading at a discrete number of attachment sites.

We used the virtual cell culture generated with our model for electrophysiological simulations. A resulting wave propagation pattern accurately reproduced the experimentally observed behaviour for both isotropic and anisotropic cases. In the isotropic case, despite the high elongation of virtual cells, the resulting excitation propagation was also isotropic as in the experiment due to the lack of preferential direction [41–43]. For the anisotropic monolayer, a correct range of anisotropy ratios and wavefront complexity were achieved. An overview on our study is presented in Figure S1 in Supplementary Material.

Our GGH-type model for cardiac tissue describes discrete biological cells. Several groups have already proposed discrete models of different designs, which were mainly used to study the discontinuous nature of cardiac propagation. The first discrete model was proposed by Spach et al. [44] and contained 33 adult coupled cells, replicated directly from the experimental images. This model explained the fact that the maximum rate of rise of the transmembrane potential (\dot{V}_{max}) depends on the direction of propagation, which was previously found in the experiment [45]. Henriquez et al. [46] demonstrated the role of cellular shape irregularities in a conduction block and in re-entry formation; they also introduced FBs to the model [47] and studied how various coupling coefficients would affect wave propagation. In these studies, randomised cell forms were generated by a custom iterative growth algorithm [48] that was adjusted to fit length and width distributions. Since cell shapes in their studies were irregular, they were triangulated and FEM algorithm for electrical simulations was applied (in 2D [49] and 3D [50]). Other groups that encountered anisotropic and discontinuous effects also developed discretisation algorithms similar to Henriquez [51, 52]. From this perspective, we propose a discrete

model of a new kind; it combines both realistic cell shapes of the Spach model and the scalability of the models of Jacquemet-Henriquez [47], Lin-Keener [52] and Prudat-Kucera [51].

FBs are ubiquitous in cardiac tissue and are indispensable in engineered cardiac cell cultures [53]. Thus, we also included FBs into our morphological model. With additional improvements in our model describing the spatial distribution of FBs in a culture, it would be possible to study the arrhythmogenicity of different types of fibrosis. Depending on the parameters, samples with patchy, diffuse or interstitial fibrosis could be generated. Such modelling may provide some ideas on fibrosis development and possible ways of treatment.

Note that currently, our monolayer formation model is only at the first stage of development. However, various general scientific questions can already be addressed with it. For example, it can be applied to study the development of iPS cell cultures *in vitro* or cell clusters *in vivo*, which is one of the hottest topics in cardiac stem cell research [54]. It can be used to study percolation phenomena in cardiac tissue, which is considered an important determinant of atrial fibrillation [55]. More generally, such a model can be applied to describe the dynamic remodelling of cardiac tissue after myocardial infarction or during the development of heart failure. Additionally, the electrophysiological model may be further improved. Using our virtual tissues, one can study various types of cell-to-cell communications. It may include study of the role of the non-uniform distribution of ionic channels in cell membranes and non-junctional cell-to-cell signal transmission. However, the further development of our approach is needed to achieve all these goals.

Firstly, additional research related to cell migration and dynamics is required. The current version of our model, adjusted to the experiment, exhibits low motility of the cells. However, migration is a very important part of tissue development that provides cell sorting and clustering. Cell clustering may then substantially change propagation safety and anisotropy. Switching the migration on in our model is possible by increasing motility by decreasing the penalty for detachment and target spreading areas. As the result of this change, cells would be able to migrate and sort, but not able to spread properly. Probably, these parameters should evolve during monolayer formation, allowing migra-

tion at the first stage and spreading at the second stage. However, additional time-lapse data regarding monolayer formation are required to develop a valid dynamic model for monolayer formation.

Next, the cell shapes in experimental cell cultures vary greatly according to our experimental data. Our model, however, reproduces only the average cell, but not the ensemble of cells with a wide parameter distribution. The dynamics of the real cells observed in the experiment may be unique for each cell. The parameters of our model should be modified in a way that each cell has its own target volume, protrusion dynamics, and other parameters. This approach creates a family of models and was already successfully implemented in cardiac electrophysiology. It describes experimentally observed AP variability [38] and modulation [56] and can be also extended to describe morphological variations between the cells in the tissue.

In this paper we apply discrete modelling approach to reproduce the complexity of the cardiac microstructure. Alternatively, the heterogeneous tissues could be described with the modern continuous models [56–59]. In these models, the continuous diffusion term is substituted by a fractional Laplacian [56, 57] or porous-medium diffusion term [58] to account for high heterogeneity of the tissue. Discrete and continuous approaches could efficiently complement each other. For example, one could perform homogenisation for our discrete model and verify the resulting excitation patterns. The continuous model could be then used for large-scale 3D simulations of the real heart, still taking into account the discontinuous nature of the wave propagation in heterogeneous media.

Finally, the model can be extended to a third dimension to describe *in vivo* tissues. Doing so can allow us to reproduce the observed changes in the area of the isolated cells compared with the cells in cultures in terms of single parameter sets, and to generate proper cell elongation more easily. This is because in our model, cell extension was prevented by the pressure arising from the interaction of a given cell with its neighbouring cells. This effect will be absent in 3D because the cell would be able to move into the third dimension by increasing its height. Including real ECM [60] in a model and studying its guiding role in cardiac tissue formation would also be possible.

Methods

4.4.4 Experimental samples preparation

Neonatal cardiac cell isolation. All studies conformed to the Guide for the Care and Use of Laboratory Animals, published by the United States National Institutes of Health (Publication No. 85-23, revised 1996) and approved by the Moscow Institute of Physics and Technology Life Science Center Provisional Animal Care and Research Procedures Committee, Protocol #A2-2012-09-02. In this study, we used enzymes adapted to the existing two-day protocol selection from Worthington-Biochem¹. Cardiac cells were isolated from the ventricles of rat pups (*Rattus norvegicus*, Sprague Dawley breed) with different ages (1–4 days). Then, the isolated cells were seeded on the specimens covered with fibronectin (0,16 mg/ml, Gibco, USA, 33016015) at different concentrations before they were cultivated in DMEM culture medium (Gibco, USA, 11960) with 5% of FBS (foetal bovine serum, Gibco, USA, 10100147). For the study of the shapes of the isolated cells, the cells were seeded at $5 \cdot 10^3$ cells/cm². After 3 days of cultivation, the samples were fixated. The monolayers of primary culture cells were seeded at $30 \cdot 10^3$ cells/cm², and after 3–5 days, the monolayers were confluent, performed coordinated contraction activity and, therefore, were used in morphometrical studies and optical mapping.

Nanofibre preparation. The polycaprolactone (PCL) solution was prepared by dissolving PCL powder (Sigma-Aldrich, USA, 440744) in hexafluoroisopropanol at concentrations of 10%–15%. The prepared solution was electrospun with Nanon-01 electrospinning setup (MECC CO., LTD), with the applied voltage between the syringe tip and the grounded collector in the range of 5 kV to 10 kV. It was loaded into the 3 ml syringe and ejected through the 20 gauge blunt tip needle at a flow rate of 0.1–1 ml/h with the use of a programmable syringe pump (Fusion 100, Chemyx Inc., Japan). Nanofibres were electrospun directly onto the surface of a 15 mm-diameter cover glass deposited on the grounded collector. The angular velocity was 1,000 rpm. After the electrospinning process was completed, the non-adhesive PCL nanofi-

¹<http://www.worthingtonbiochem.com/NCIS/default.html>

brous substrates were coated with a solution of human plasma fibronectin (0.16 mg/ml in PBS, Gibco, USA, 33016015) to produce a cell adhesive matrix.

Note that only one fibre density was used in all experiments for both monolayer and isolated cell setups.

Immunohistochemical staining. The cells were fixated with 5% PFA (paraformaldehyde powder, 95%, Sigma-Aldrich, USA, 158127-100G), and nuclear staining was performed with DAPI (VECTASHIELD Mounting Medium with DAPI, Vector, USA, Cat. No. H-1200). In our work, we used anti- α -actinin (Sigma-Aldrich, USA, A7811) and alexa fluor 594 like Secondary Antibody (A-11020, Life Technologies) for CM-specific labelling, Alexa Fluor 488 phalloidin (Molecular Probes, USA, A12379) for F-actin non-specific staining and DAPI for labelling cell DNA. Pictures were taken with an inverted fluorescence microscope (Axio Imager with ApoTome optical sectioning module, Zeiss). Immunofluorescent staining of the CMs was performed with the use of secondary and primary antibodies according to a previously described protocol².

Optical mapping. To monitor activity and record the excitation patterns, the 3- to 5-day-old monolayers were loaded with the Ca^{2+} -sensitive indicator Fluo-4-AM (Molecular Probes, USA, F14201). After staining, the medium was exchanged with Tyrode's solution (Sigma-Aldrich Co., USA, T2145-10L) and kept at room temperature during the observations. The excitation waves were monitored with a high-speed imaging setup (Olympus MVX-10 Macro-View fluorescent microscope equipped with high-speed Andor EM-CCD Camera 897-U at 68 fps).

All videos were processed with ImageJ software. The experimental optical mapping signal was processed for noise reduction and better wavefronts representation. The Gaussian smoothing filter was applied with 250 μm and 300 μm kernel size for isotropic and anisotropic samples respectively. The same processing with the same kernel size was applied to the simulated waves (see Fig. 4.6).

²<http://www.abcam.com/protocols/immunocytochemistry-immunofluorescence-protocol>

Velocity ratio measurements for anisotropic tissue. The L-shaped samples were prepared for velocity ratio measurements (see Fig. 4.6). The nanofibres were spun parallel to one of the arms. The electrode was placed at the joint part, at the intersection of the middle lines of the arms. As a result, both arms were stimulated equally. The longitudinal and transversal velocities were measured for the plane wavefronts propagating along each of the arms.

4.4.5 Cell shape acquisition

Neonatal rat cells were stained with DAPI (DNA, blue), phalloidin (F-actin, green) and monoclonal anti- α -actinin antibody (α -actinin, red). Phalloidin staining was also compared with the optical images to ensure that F-actin fibres highlight the edge of the cell (not shown). From the α -actinin image, CMs were discriminated from FBs (see Fig. 4.2). For the F-actinin images, the contrast was enhanced so that the whole cells were coloured. Then, for the isolated cells, we selected the filled area and manually included all the small inner parts that were not enriched with F-actin and, therefore, not selected automatically. For CMs in monolayers surrounded by FBs, the same technique with α -actinin staining was used. As a result, each CM was highlighted separately. In the other context in monolayers, we had to outline the cell shape manually. Following this procedure, the database of cell shapes was collected for each of the four conditions that we studied (see Fig. 4.1). After the cell was selected, the contour was transferred to the vector form, and the obtained curve was then used in the shape analysis.

All processing was done with custom Wolfram Mathematica (WM) ³ code using a `ComponentMeasurements[]` tool. All possible parameters related to cell shape were checked. Those that are either necessary for the model or characteristic of one of the cell types were selected. Firstly, the total area and elongation were measured. Elongation here is the ratio between the largest and the smallest diameter of the convex hull ("Caliper Elongation"). In WM, the elongation is defined as $1 - w/l$, where w is the width and l is the length. We changed this definition to l/w , which is more useful in our study. Next, the

³<http://www.wolfram.com/mathematica/?source=nav>

cell was surrounded with a convex hull with the use of the “Convex Vertices” parameter of `ComponentMeasurements[]` in WM. The proportion of the convex hull occupied by the cell appeared to be an important parameter and was substantially different for CMs and FBs. Therefore, the ratio of the cell area and the area of the convex hull was also included in the list of parameters.

Cardiac cells have a characteristic polygonal shape because they have a discrete number of adhesion sites that are essential for the spreading process. The number of these adhesion sites can be found through observation of the F-actin image. Actin filaments are concentrated in these mature adhesion sites pulling the cell body towards this point. From the images, we could count the number of adhesion sites manually. However, we also developed an automatic algorithm to determine the quantity of adhesion points. It is based on the fact that protrusive activity at the adhesion sites results in convexity formation. To count the convex regions, we rasterised cell contours with a resolution of $1.0\ \mu\text{m}$ per pixel and applied skeleton transform to it (using `SkeletonTransform[]` in WM). The raw experimental data had a different but higher resolution (of $0.10\text{--}0.42\ \mu\text{m}/\text{px}$). Then, the central part of the skeleton transform was removed, and the number of tips was counted. This number of protrusions was compared with the number of adhesion sites, which were counted manually (for CMs $N_{\text{CM}}^{\text{pr}} = 18 \pm 4$ ($n_{\text{CM}} = 36$), for FBs $N_{\text{FB}}^{\text{pr}} = 21 \pm 5$ ($n_{\text{FB}} = 45$)), and the algorithm gave similar results (for CMs $N_{\text{CM}}^{\text{pr}} = 14 \pm 5$ ($n_{\text{CM}} = 36$), for FBs $N_{\text{FB}}^{\text{pr}} = 16 \pm 6$ ($n_{\text{FB}} = 45$)).

However, the space resolution of our model was chosen to be lower ($2.5\ \mu\text{m}$ instead of $1.0\ \mu\text{m}$). Such a space step of $2\text{--}2.5\ \mu\text{m}$ is standard in various GGH models for most eukaryotic cell simulations [13, 14, 61] and electrophysiological studies in discrete cellular models [51]. For this resolution, some of the protrusions average out and are not pronounced enough to be detected with the skeleton transform algorithm. As a result, the number of convexes in our model turned out to be less than that in the experiment. However, some parts of the discrete border of the cell in the simulation may also be recognised as an additional protrusion. Despite the possible misinterpretation of the results of this algorithm, we suggest that it is appropriate for the comparison of the computed cell shapes with the experimental cell shapes. However, the algorithm in both cases should be applied to the images rescaled to the same resolution.

Statistics for convex coverage. Data are expressed as mean \pm standard deviation (SD). Analysing the parameters listed in Table 4.1, it was found that FBs have much deeper concaves than CMs, resulting in a less convex coverage (see Fig. 4.2). CMs normally occupy around 80% of the convex hull, whereas FBs occupy only 60%–70% of it. The distributions of the convex coverage over the cell population were compared and Pearson’s chi-squared test was applied to determine whether the medians of these distributions are equal. The p -value for this hypothesis was $< 10^{-3}$ ($n_{\text{CMs}} = 36$, $n_{\text{FBs}} = 45$), which means that it is very unlikely that these distributions have the same median value. The outcome of other seeding conditions is analogous.

4.4.6 Mathematical model

Cell formation is defined by the Hamiltonian of the GGH model, which, in our model, is equal to the following:

$$\begin{aligned}
 H = & \sum_{\substack{(\vec{i}, \vec{j}) \\ \text{neighbours}}} J_{\tau_{\sigma_i}, \tau_{\sigma_j}} (1 - \delta(\sigma_i, \sigma_j)) + \sum_{\sigma} \lambda_{\tau_{\sigma}} (v_{\sigma} - V_{\tau_{\sigma}}^t)^2 + \\
 & + \sum_{\substack{\vec{i} \\ \text{focal contacts} \\ \text{with glass}}} \frac{G_{\tau_{\sigma_i}}}{\rho(\vec{i}, \vec{\text{cm}}_{\sigma_i})} + \sum_{\substack{\vec{i} \\ \text{focal contacts} \\ \text{with fibers}}} \frac{G_{\tau_{\sigma_i}}}{\rho(\vec{i}, \vec{\text{cm}}_{\sigma_i})} \cos^{-1} \left(\varphi_{f_i} - \widehat{(\vec{i}, \vec{\text{cm}}_{\sigma_i})} \right) + \\
 & + \sum_{\substack{\vec{i} \\ \text{focal contacts} \\ \text{detach from substrate}}} P_{\text{detach}} + \sum_{\substack{\vec{i} \\ \text{focal contacts} \\ \text{from nanofiber}}} P_{\text{unleash}} + \sum_i P_N \quad (4.5)
 \end{aligned}$$

where i is summed over all lattice points or subcells, σ_i is the index in the i^{th} subcell and τ_{σ} is a type of cell with index σ . In our model, we consider two cell types, so τ has three possible values: 0 (medium), 1 (CM) and 2 (FB). In the simplest GGH model, the cells are only maintaining the target volume and interacting via adhesion. The first term of the equation (5.1) is an adhesive energy term given by the following:

$$J = \begin{pmatrix} J_{\text{MD-MD}} & J_{\text{CM-MD}} & J_{\text{FB-MD}} \\ J_{\text{CM-MD}} & J_{\text{CM-CM}} & J_{\text{CM-FB}} \\ J_{\text{FB-CM}} & J_{\text{CM-FB}} & J_{\text{FB-FB}} \end{pmatrix},$$

where J_{X-Y} is the energy of interaction of the cell of type X with the cell of type Y. The value of J_{MD-MD} is irrelevant because the whole medium is one subcell with one index zero, and J s are applied only on the sub-domain boundaries. Let us then assume that $J_{MD-MD} = 0$. Five independent energies are left, and these determine the matrix J . Let us first discuss their relations.

Showing the connection between J and surface tension \mathfrak{s} is easy because it basically corresponds to the surface energy. For the cell medium, $\mathfrak{s}_{CM} = J_{CM-MD}$, and for the cell-cell surface, $\mathfrak{s}_{C-C} = J_{C-C}/2 - J_{C-MD}$, where C may be either CM or FB. If $J_{C-C} < 2J_{C-MD}$, then the cells will tend to clusterise, and in the opposite case, they will repulse one another. The relation between J_{CM-CM} (or J_{FB-FB}) and J_{CM-FB} governs cell sorting and rearrangements [11]. If the energy for one of the cell types (J_{CM-CM} or J_{FB-FB}) is substantially smaller than J_{CM-FB} , then the cells of this type will condense into clusters. In this study, we use these energies as one of the many fitting parameters to adjust the model for cell shape reproduction. However, the rearrangements and clusterisation in cardiac tissue should be further studied in the future.

Generalised cells in the GGH model also have such parameters as volume v_σ and centre of mass cm . The volume of the cell tends to converge to the target volume $V_{\tau_\sigma}^t$, and λ_{τ_σ} characterises the cell elasticity around that value. The target volumes and elasticity are different for various cell types so that both of them are dependent on the type τ_σ .

The next term in (5.1) describes the protrusion at the attachment sites. We assume that the cell has a limited number of adhesion sites with protrusive activity (N_{protr}), and their dynamics in the absence of nanofibres are controlled by the potential $G_{\tau_{\sigma_i}}/\rho(\sigma_i, cm(\sigma_i))$, where $\rho(\sigma_i, cm(\sigma_i))$ is the distance from the cm to a given subcell. We proposed the simplest possible potential field to describe the expansion of the cell at the attachment sites, and we added a corresponding term to the GGH model (see Equation (4.3) in Section 4.2.2).

The focal adhesion can be detached from the substrate with a penalty P_{detach} . It is applied in an attempt to copy a subcell (with a focal adhesion or not) on the existing focal adhesion. If it is detached, then the number of adhesions of the cell to the substrate is reduced. The total number of focal adhesions for a cell should not exceed N_{protr} . If it is less than N_{protr} , then during the next successful expansion of the cell border, a new focal adhesion

will be established.

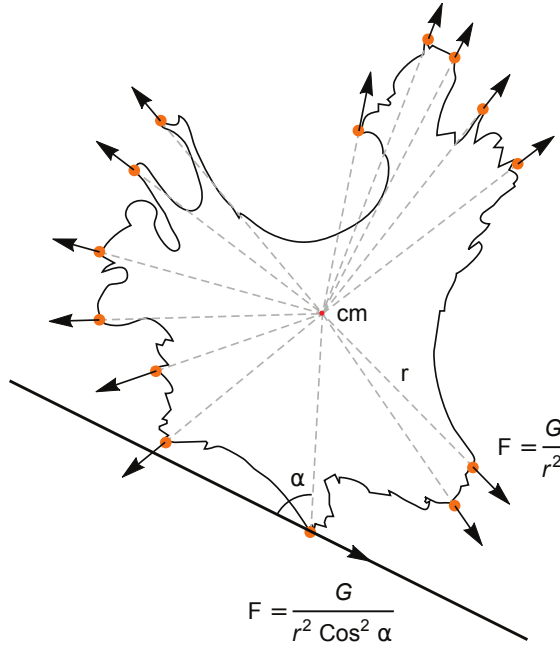
For the cell–fibre interaction, the term (4.3) was substituted with (4.4). This term takes into account the fact that the cell increases the applied force to the substrate only if there is a reaction force from the scaffold [36]. In the case of a nanofibre, this force is always aligned with it. In obtaining the corresponding energy term, the force $G/(r \cos \alpha)^2$ was integrated with the displacement along the fibre $dr \cos(\alpha)$ (see Fig. 4.7(a)), resulting in energy term $G/(r \cos \alpha)$, which is responsible for the direction dependence. Here, α is an angle between the fibre orientation (φ_{f_i}) and the direction from cm_{σ_i} to the current subcell i . The last term in (4.4) is a penalty applied for copying an adhesion site from the fibre to the non-fiber region. Copying from the non-fiber to the fibre subcell is performed without energy change (see Fig. 4.7(b)). If the Target subcell is occupied with another attachment site — the P_{detach} is additionally applied, since the target attachment was destroyed. The justification for this term is given in Section 4.2.2.

Apart from the energy terms described with Equation (5.1), the cell shapes were also affected by two rules in the algorithm. Firstly, the copy attempts that break the connectivity of the cell were not considered and automatically rejected. Secondly, the protrusion was limited by a certain maximal length, which is specified in Table 4.2. Finally, if, as a result of a copy attempt, a cell disappears, then this action is also forbidden.

Finally, a penalty was added to protect the nuclei of the cell. The nuclei were assumed to be much stiffer than the cell body. Here, P_N was set to $2.0 \times P_{\text{detach}}$ for all the cells that are closer to cm than to $7 \mu\text{m}$.

Initial conditions. The cells were seeded with the density specified in Table 4.2 for each case. The sample was divided into $N_x \times N_y$ areas, and within these areas, the square seed of the size $\sqrt{V_t/10}$ was placed in a random place within this area. There are no focal adhesions at the beginning, but during the first successful expansions of the cell border, focal adhesions are placed in newly added subcells. Their number is limited by N_{protr} for each cell.

Parameter adjustment. The parameters of the model were varied with the use of Monte Carlo algorithm to fit the experimental characteristics of



(a)

		Target	
		On fiber	Off fiber
Source	On fiber	$\frac{G}{r \cos \alpha}$	$+ P_{\text{unleash}}$
	Off fiber	$\frac{G}{r}$	$\frac{G}{r}$

(b)

Figure 4.7: Schematic representation of cell spreading and cell-nanofibre interaction. (a) The cell shape was taken from the experimental database. All protrusions are marked with orange circles. Arrows show the direction of the resulting force driving the cell expansion at the attachment sites. If no guiding fibres exist, the cell spreads equidirectionally, and the forces are directed from the centre of mass of the cell (cm). If a nanofibre exists (at the bottom), and the cell is already attached to it, then the force is aligned with the fibre. (b) Energy terms, applied for different copy attempts of the attachment site to the non-attachment subcell, from the isotropic substrate to the fiber or in opposite direction.

the cell shapes. The best fit for the five selected parameters (area, convex coverage, elongation, number of convexes and protrusions) was found, and the corresponding parameters of the model are listed in Table 4.2.

Numerical implementation. Our GGH model was implemented on the basis of the code published as a part of Ref. [61] (Protocol S1). The code for adhesive and elastic energies was unchanged, but the function for protrusion energy was added.

The space step was $2.5 \mu\text{m}$, and the mesh size was 320×320 voxels or $0.8 \text{ mm} \times 0.8 \text{ mm}$ for monolayer simulations, or 400×400 voxels or $1.0 \text{ mm} \times 1.0 \text{ mm}$ for isolated cells (see Table 4.2). For electrophysiological studies, larger meshes (with the same $2.5 \mu\text{m}$ resolution) were generated.

The code was optimised to compute large meshes. Connectivity check was performed previously in a whole sample, and the program took $O(n^2)$ time, where n is the number of voxels in the sample. Each cell was surrounded with a box and the connectivity was checked only within the box. Therefore, the connectivity check itself took $O(m)$ instead of $O(n)$, where m is the size of the box. The size of an average box is comparable to the size of a cell and does not change with a change in the sample size. Therefore, the whole GGH model now scales linearly ($O(n)$) with the sample size.

With this optimisation, it takes 3.5 hours on an Intel Core i7-3930K CPU to compute a $1 \text{ cm} \times 1 \text{ cm}$ monolayer on fibres.

4.4.7 Electrophysiological model

We used a monodomain ionic model of neonatal rat CM, developed by R. Majumder in 2016 [39], which is a modification of the Kohronen model with simplified calcium dynamics. The transmembrane potential in this model was determined as follows:

$$\frac{\partial V}{\partial t} = \nabla(D\nabla V) - \frac{I_{\text{ion}} + I_{\text{stim}}}{C_m}, \quad (4.6)$$

where V is the transmembrane potential, C_m is the membrane capacitance, and D is the coupling coefficient. Coefficient D depends on the space variable and

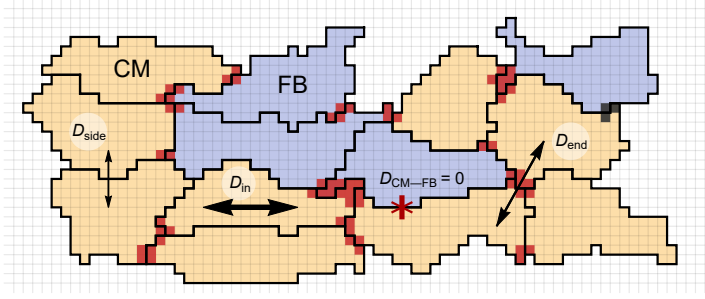


Figure 4.8: **Algorithm for the coupling coefficient assignment.** CMs are coloured in yellow, whereas FBs are coloured in blue. Dark red areas represent end-end type connections where the attachment sites in a GGH model are located. Between the red subcells of two different cells, the D_{end} coefficient was used. For all other connections between cells, the coupling coefficient was D_{side} . For connections within a cell, the coupling coefficient was D_{in} , and $D_{in} \gg D_{end} > D_{side}$. No coupling occurred between CM and FB in our model.

differs substantially for cell-cell connections or propagation within a biological cell. Each subcell in the GGH model was used as a voxel for electrophysiological simulations.

The I_{ion} is given by the sum of the following ionic currents:

$$I_{ion} = I_{Na} + I_{K1} + I_{to} + I_{Kr} + I_{Ks} + I_{CaL} + I_{NaCa} + I_{NaK} + I_{pCa} + I_{pK} + I_{bCa} + I_{bNa}. \quad (4.7)$$

The equations for these currents are listed in R. Majumder paper [39].

We implemented a non-uniform distribution of gap junctions (GJs) along the cell membrane, that was previously shown in experiments [62, 63]. We assumed that more connexins were transported to the attachment sites because the directions of the actin filaments and microtubules of the cell are correlated with one another [64]. Microtubules are pathways for the transportation of proteins making ionic channels from the centriole to the membrane [65]. Actin filaments, on the contrary, polymerise from the attachment site to the cell body. Therefore, we expect more proteins to be transported to the protrusion sites, leading to a non-uniform channel distribution.

As a result, stronger cell-cell connections were created if the protrusion of one cell touches the protrusion of the other cell. In this case, we used $D_{end-end}$

(see fig. 4.8). For all other connections, coefficient $D_{\text{side-side}}$ was applied. This approach allowed us to obtain the functional anisotropy for a geometrically elongated cell without setting any preferred direction in the model. The coupling coefficients between CMs and FBs were equal to zero in this study.

The exact value of $D_{\text{end-end}}$ was adjusted to fit the longitudinal velocity. In figure 4.6, $D_{\text{side-side}} = 0$, $D_{\text{end-end}} = 0.01D_{\text{in}}$ in isotropic case, and $0.02D_{\text{in}}$ in anisotropic sample. In simulations with $D_{\text{side-side}} = D_{\text{end-end}} = D_{\text{in}}$ the lowest possible anisotropy ratio was achieved.

GJ distribution Two types of connections are considered in our model: end-to-end and side-to-side connections. The end-to-end connection was established at the sites adjoined the attachment sites. We hypothesised that more GJs are distributed along the cytoskeleton. Therefore, we proposed one more GGH-like model for channel distribution. This model has two types of cells: more-GJ and less-GJ subcells. The Hamiltonian of the model comprises only two terms:

$$H = H_{\text{adhesive}} + H_{\text{protr}} = \sum_{\substack{(\vec{i}, \vec{j}) \\ \text{neighbours}}} J_{\tilde{\sigma}_i, \tilde{\sigma}_j}^{\sigma_i, \sigma_j} + \sum_{\substack{\vec{i} \\ \text{more-GJ}}} \frac{G}{\rho(\vec{i}, \vec{\text{cm}}_{\tilde{\sigma}_i})} \quad (4.8)$$

where $G = 25.0$ is the spreading constant, and J is equal to 0 for the end-to-end connections between two different cells, $J_H = 2.0$ for side-to-side connections and $J_B = 10.0$ for the interactions of the contacts within one biological cell. $\tilde{\sigma}$ is the index specifying the connection type (0: less GJ, 1: more GJ), and σ is the cell index, which was taken from the cell morphology simulation and remained constant during the channel distribution computations. This model induces the GJs to spread further from the cm (the higher is the G), preferably along the border (the higher is the J_B) and preferably keeping the connection with more-GJ subcells of the other cells (J_H). These parameters were adjusted to create a reasonable surrounding of the attachment sites. However, this model has no data for validation yet.

Finally, with the use of the resulting channel distribution from this simulation, coupling coefficients were assigned. The end-to-end coupling coefficient $D_{\text{end-end}}$ was applied if, on both sides of the border, a subcell of a more-GJ

type exists. For all other intercellular connections, $D_{\text{side-side}}$ was used.

The conduction velocity highly depends on the five parameters (G_N , J_H , J_B , $D_{\text{end-end}}/D_{\text{in}}$, $D_{\text{side-side}}/D_{\text{in}}$). If $D_{\text{side-side}} \ll D_{\text{end-end}}$, the anisotropy mainly depends on channel distribution, and $D_{\text{end-end}}$ regulates the longitudinal velocity. However, in our irregular discrete model, the velocity ratio was limited by the geometrical anisotropy. From this, we concluded that morphological studies provide essential constraints on the excitation propagation. The details of cell-to-cell signal transduction should be studied further.

Numerical implementation We used graphic processing units (GPUs) for the detailed ionic model integration. GPUs are very efficient for excitable media simulations with large sample sizes. The ionic model was already implemented in CUDA in our group [39, 66], but the coupling term of the model was significantly changed in the current study.

The equation (4.6) was discretised and solved with the alternating direction (AD) implicit method. The hidden $n + 1/2$ time step was added to implement it. The currents were computed with the parameters from the previous time step n . The diffusion was first computed explicitly in one direction (taking time step n) and implicitly in the other direction during the $1/2$ time step:

$$\begin{aligned} \frac{V^{n+1/2} - V^n}{\tau/2} = & \frac{D_{\text{left}}(V_{\text{left}}^{n+1/2} - V^{n+1/2}) + D_{\text{right}}(V_{\text{right}}^{n+1/2} - V^{n+1/2})}{h^2} + \\ & + \frac{D_{\text{top}}(V_{\text{top}}^n - V^n) + D_{\text{bottom}}(V_{\text{bottom}}^n - V^n)}{h^2} + I_{\text{ion}}^n \quad (4.9) \end{aligned}$$

Afterwards, the directions were swapped, and the procedure was repeated. On each half-step and at each point, there are three potentials V taken at a future $n + 1/2$ time step. To find them, let us rewrite the equation (4.9) in the form $AV^{n+1/2} = b^n$, where A is a constant matrix. This matrix is tridiagonal. Therefore, the tridiagonal solver from the cuSPARSE library was used to find $V^{n+1/2}$ from V^n . V^{n+1} was found similarly from $V^{n+1/2}$ after direction exchange.

The reason why we use the AD method is that the space step in our model should be $h = 2.5 \mu\text{m}$, the same as that in the GGH model. The explicit

algorithm is limited by the Courant number, which is equal to Dh/τ^2 and should not exceed $1/2$ for differential equations of parabolic type. Normally, in our computations for arrhythmia studies, h is equal to $250\ \mu\text{m}$ [66], which is comparable to the cell size, and the time step is $20\ \mu\text{s}$. If the space step is reduced to $2.5\ \mu\text{m}$, then the time step in the explicit model becomes $2\ \text{ns}$, and the computational time increases 10^8 times. Therefore, the explicit method is not applicable to subcellular studies.

On the other hand, implicit or semi-implicit methods possess absolute stability, and larger time steps could be used. The approximation of the solution will be affected on the subcellular level, but because the important spatial harmonics of the solution are much bigger than the cell or subcell size, then the macroscopic solution of the wavefront propagation will be calculated correctly. We took $h = 2.5\ \mu\text{m}$ and the time step $t = 1\ \text{ms}$; the highest coupling coefficient was $D = 1\ \text{cm}^2/\text{s}$.

The anisotropy was tested in the $4.96\ \text{mm} \times 4.96\ \text{mm}$ samples (1984×1984 grid points). It was cut from a larger $5.0\ \text{mm} \times 5.0\ \text{mm}$ mesh from the GGH model to reduce the margin size without the cells and to fit the GPU architecture better. The program runs on GPU most efficiently if the size of the sample is divisible by the block size (32×32 in our simulations). For the simulation of the 40 ms activity, it took 75 minutes on the GPU. For larger samples, the computation time scales as $O(n^2)$, where n is the total number of grid points.

References

- [1] R. Mehra, “Global public health problem of sudden cardiac death.,” *Journal of electrocardiology*, vol. 40, pp. S118–22, 2007.
- [2] R. Rath, J. B. Lee, T.-L. Tran, *et al.*, “Biomimetic Microstructure Morphology in Electrospun Fiber Mats is Critical for Maintaining Healthy Cardiomyocyte Phenotype,” *Cellular and Molecular Bioengineering*, vol. 9, pp. 107–115, 2016.
- [3] G. M. Fomovsky, S. Thomopoulos, and J. W. Holmes, “Contribution of extracellular matrix to the mechanical properties of the heart.,” *Journal of molecular and cellular cardiology*, vol. 48, pp. 490–6, 2010.
- [4] P. Kohl, P. Camelliti, F. L. Burton, and G. L. Smith, “Electrical coupling of

- fibroblasts and myocytes: relevance for cardiac propagation.,” *Journal of electrophysiology*, vol. 38, pp. 45–50, 2005.
- [5] S. F. A. Askar, B. O. Bingen, M. J. Schali, *et al.*, “Similar arrhythmicity in hypertrophic and fibrotic cardiac cultures caused by distinct substrate-specific mechanisms,” *Cardiovascular Research*, vol. 97, no. 1, pp. 171–181, 2013.
- [6] N. A. Trayanova, P. M. Boyle, H. J. Arevalo, and S. Zahid, “Exploring susceptibility to atrial and ventricular arrhythmias resulting from remodeling of the passive electrical properties in the heart: A simulation approach,” *Frontiers in Physiology*, vol. 5, no. Nov, p. 435, 2014.
- [7] J. R. Martina, P. H. Bovendeerd, N. de Jonge, *et al.*, “Simulation of Changes in Myocardial Tissue Properties During Left Ventricular Assistance With a Rotary Blood Pump,” *Artificial Organs*, vol. 37, pp. 531–540, 2013.
- [8] Z. Ma, J. Wang, P. Loskill, *et al.*, “Self-organizing human cardiac microchambers mediated by geometric confinement,” *Nature Communications*, vol. 6, p. 7413, 2015.
- [9] J. R. Hussan, M. L. Trew, and P. J. Hunter, “A Mean-field Model of Ventricular Muscle Tissue,” *Journal of Biomechanical Engineering*, vol. 134, no. 7, p. 071003, 2012.
- [10] F. Graner and J. Glazier, “Simulation of biological cell sorting using a two-dimensional extended Potts model,” *Physical review letters*, vol. 69, pp. 2013–2016, 1992.
- [11] J. Glazier and F. Graner, “Simulation of the differential adhesion driven rearrangement of biological cells,” *Physical review. E, Statistical physics, plasmas, fluids, and related interdisciplinary topics*, vol. 47, pp. 2128–2154, 1993.
- [12] N. J. Savill and P. Hogeweg, “Modelling Morphogenesis: From Single Cells to Crawling Slugs,” *Journal of Theoretical Biology*, vol. 184, no. 3, pp. 229–235, 1997.
- [13] V. A. Grieneisen, J. Xu, A. F. M. Marée, P. Hogeweg, and B. Scheres, “Auxin transport is sufficient to generate a maximum and gradient guiding root growth,” *Nature*, vol. 449, pp. 1008–13, 2007.
- [14] R. M. H. Merks, E. D. Perryn, A. Shirinifard, and J. A. Glazier, “Contact-inhibited chemotaxis in de novo and sprouting blood-vessel growth,” *PLoS computational biology*, vol. 4, p. e1000163, 2008.
- [15] M. A. Knewitz and J. C. M. Mombach, “Computer simulation of the influ-

- ence of cellular adhesion on the morphology of the interface between tissues of proliferating and quiescent cells.,” *Computers in biology and medicine*, vol. 36, pp. 59–69, 2006.
- [16] A. F. Marée and P. Hogeweg, “How amoeboids self-organize into a fruiting body: multicellular coordination in *Dictyostelium discoideum*.,” *Proceedings of the National Academy of Sciences of the United States of America*, vol. 98, pp. 3879–83, 2001.
- [17] N. J. Savill and J. A. Sherratt, “Control of epidermal stem cell clusters by Notch-mediated lateral induction.,” *Developmental biology*, vol. 258, pp. 141–53, 2003.
- [18] R. M. H. Merks and J. A. Glazier, “Dynamic mechanisms of blood vessel growth.,” *Nonlinearity*, vol. 19, pp. C1–C10, 2006.
- [19] M. Burrows, “Rhythmical Activity of Isolated Heart Muscle Cells in Vitro,” *Science*, vol. 36, no. 916, pp. 90–92, 1912.
- [20] P. A. Lalit, M. R. Salick, D. O. Nelson, *et al.*, “Lineage Reprogramming of Fibroblasts into Proliferative Induced Cardiac Progenitor Cells by Defined Factors,” *Cell Stem Cell*, vol. 18, pp. 354–367, 2016.
- [21] N. Huebsch, P. Loskill, N. Deveshwar, *et al.*, “Miniaturized iPS-Cell-Derived Cardiac Muscles for Physiologically Relevant Drug Response Analyses.,” *Scientific reports*, vol. 6, p. 24726, 2016.
- [22] Y. Shiba, S. Fernandes, W.-Z. Zhu, *et al.*, “Human ES-cell-derived cardiomyocytes electrically couple and suppress arrhythmias in injured hearts,” *Nature*, vol. 489, pp. 322–325, 2012.
- [23] E. Entcheva, S. N. Lu, R. H. Troppman, V. Sharma, and L. Tung, “Contact fluorescence imaging of reentry in monolayers of cultured neonatal rat ventricular myocytes.,” *Journal of Cardiovascular Electrophysiology*, vol. 11, no. 6, pp. 665–676, 2000.
- [24] Y. Orlova, N. Magome, L. Liu, Y. Chen, and K. Agladze, “Electrospun nanofibers as a tool for architecture control in engineered cardiac tissue.,” *Biomaterials*, vol. 32, pp. 5615–24, 2011.
- [25] L. Yue, J. Xie, and S. Nattel, “Molecular determinants of cardiac fibroblast electrical function and therapeutic implications for atrial fibrillation.,” *Cardiovascular research*, vol. 89, pp. 744–53, 2011.
- [26] M. B. Thomsen and K. Calloe, “Human atrial fibroblasts and their contribution to supraventricular arrhythmia,” *Physiological reports*, vol. 4, pp. 3–5, 2016.

-
- [27] J. Satulovsky, R. Lui, and Y.-L. Wang, “Exploring the control circuit of cell migration by mathematical modeling,” *Biophysical journal*, vol. 94, pp. 3671–83, 2008.
 - [28] T. Akanuma, C. Chen, T. Sato, R. M. H. Merks, and T. N. Sato, “Memory of cell shape biases stochastic fate decision-making despite mitotic rounding,” *Nature Communications*, vol. 7, p. 11963, 2016.
 - [29] P. J. Albert and U. S. Schwarz, “Dynamics of cell shape and forces on micropatterned substrates predicted by a cellular Potts model,” *Biophysical journal*, vol. 106, pp. 2340–52, 2014.
 - [30] A. Shirinifard, J. S. Gens, B. L. Zaitlen, *et al.*, “3D Multi-Cell Simulation of Tumor Growth and Angiogenesis,” *PLoS ONE*, vol. 4, p. e7190, 2009.
 - [31] A. Gamba, D. Ambrosi, A. Coniglio, *et al.*, “Percolation, Morphogenesis, and Burgers Dynamics in Blood Vessels Formation,” *Physical Review Letters*, vol. 90, p. 118101, 2003.
 - [32] A. Szabó and R. M. H. Merks, “Cellular Potts Modeling of Tumor Growth, Tumor Invasion, and Tumor Evolution,” *Frontiers in Oncology*, vol. 3, p. 87, 2013.
 - [33] J. A. Glazier, A. Balter, and N. J. Popławski, “Magnetization to Morphogenesis: A Brief History of the Glazier-Graner-Hogeweg Model,” in *Single-Cell Based Models in Biology and Medicine*, pp. 79–106, 2007.
 - [34] A. D. Doyle, F. W. Wang, K. Matsumoto, and K. M. Yamada, “One-dimensional topography underlies three-dimensional fibrillar cell migration,” *The Journal of cell biology*, vol. 184, pp. 481–90, 2009.
 - [35] J. Foolen, T. Yamashita, and P. Kollmannsberger, “Shaping tissues by balancing active forces and geometric constraints,” *Journal of Physics D: Applied Physics*, vol. 49, p. 053001, 2016.
 - [36] I. Schoen, B. L. Pruitt, and V. Vogel, “The Yin-Yang of Rigidity Sensing: How Forces and Mechanical Properties Regulate the Cellular Response to Materials,” *Annual Review of Materials Research*, vol. 43, no. 1, pp. 589–618, 2013.
 - [37] A. Muszkiewicz, O. J. Britton, P. Gemmell, *et al.*, “Variability in cardiac electrophysiology: Using experimentally-calibrated populations of models to move beyond the single virtual physiological human paradigm,” *Progress in Biophysics and Molecular Biology*, vol. 120, pp. 115–127, 2016.
 - [38] T. A. Gokhale, J. M. Kim, R. D. Kirkton, N. Bursac, and C. S. Henriquez,

- “Modeling an Excitable Biosynthetic Tissue with Inherent Variability for Paired Computational-Experimental Studies,” *PLOS Computational Biology*, vol. 13, no. 1, p. e1005342, 2017.
- [39] R. Majumder, M. C. Engels, A. A. F. de Vries, A. V. Panfilov, and D. A. Pijnappels, “Islands of spatially discordant APD alternans underlie arrhythmogenesis by promoting electrotonic dyssynchrony in models of fibrotic rat ventricular myocardium.,” *Scientific reports*, vol. 6, p. 24334, 2016.
- [40] L. L. Cooper, K. E. Odening, M.-S. Hwang, *et al.*, “Electromechanical and structural alterations in the aging rabbit heart and aorta,” *American journal of physiology. Heart and circulatory physiology*, vol. 302, pp. H1625–H1635, 2012.
- [41] N. Badie and N. Bursac, “Novel micropatterned cardiac cell cultures with realistic ventricular microstructure.,” *Biophysical journal*, vol. 96, pp. 3873–85, 2009.
- [42] H. X. Nguyen, R. D. Kirkton, and N. Bursac, “Engineering prokaryotic channels for control of mammalian tissue excitability.,” *Nature communications*, vol. 7, p. 13132, 2016.
- [43] R. D. Kirkton and N. Bursac, “Engineering biosynthetic excitable tissues from unexcitable cells for electrophysiological and cell therapy studies.,” *Nature communications*, vol. 2, p. 300, 2011.
- [44] M. S. Spach and J. F. Heidlage, “The Stochastic Nature of Cardiac Propagation at a Microscopic Level : Electrical Description of Myocardial Architecture and Its Application to Conduction,” *Circulation Research*, vol. 76, pp. 366–380, 1995.
- [45] M. S. Spach, J. F. Heidlage, E. R. Darken, *et al.*, “Cellular Vmax reflects both membrane properties and the load presented by adjoining cells,” *Am J Physiol Heart Circ Physiol*, vol. 263, pp. H1855–1863, 1992.
- [46] M. L. Hubbard and C. S. Henriquez, “Microscopic variations in interstitial and intracellular structure modulate the distribution of conduction delays and block in cardiac tissue with source-load mismatch.,” *Europace*, vol. 14 Suppl 5, pp. v3–v9, 2012.
- [47] V. Jacquemet and C. S. Henriquez, “Loading effect of fibroblast-myocyte coupling on resting potential, impulse propagation, and repolarization: insights from a microstructure model.,” *American journal of physiology. Heart and circulatory physiology*, vol. 294, no. 5, pp. H2040–52, 2008.
- [48] M. L. Hubbard, W. Ying, and C. S. Henriquez, “Effect of gap junction distri-

- bution on impulse propagation in a monolayer of myocytes: a model study.,” *Europace*, vol. 9 Suppl 6, pp. vi20–8, 2007.
- [49] J. M. Kim, N. Bursac, and C. S. Henriquez, “A Computer Model of Engineered Cardiac Monolayers,” *Biophysical journal*, vol. 98, no. 9, pp. 1762–1771, 2010.
- [50] J. Stinstra, R. Macleod, C. Henriquez, and P. E. Mchugh, “Incorporating histology into a 3D microscopic computer model of myocardium to study propagation at a cellular level.,” *Ann Biomed Eng*, vol. 38, no. 4, pp. 1399–1414, 2011.
- [51] Y. Prudat and J. P. Kucera, “Nonlinear behaviour of conduction and block in cardiac tissue with heterogeneous expression of connexin 43.,” *Journal of molecular and cellular cardiology*, vol. 76, pp. 46–54, 2014.
- [52] J. Lin and J. P. Keener, “Microdomain Effects on Transverse Cardiac Propagation,” *Biophysical journal*, vol. 106, no. 4, pp. 925–931, 2014.
- [53] T. Iwamiya, K. Matsuura, S. Masuda, T. Shimizu, and T. Okano, “Cardiac fibroblast-derived VCAM-1 enhances cardiomyocyte proliferation for fabrication of bioengineered cardiac tissue,” *Regenerative Therapy*, vol. 4, pp. 92–102, 2016.
- [54] K. Wei, V. Serpooshan, C. Hurtado, *et al.*, “Epicardial FSTL1 reconstitution regenerates the adult mammalian heart,” *Nature*, vol. 525, pp. 479–485, 2015.
- [55] E. Vigmond, A. Pashaei, S. Amraoui, H. Cochet, and M. Hassaguerre, “Percolation as a mechanism to explain atrial fractionated electrograms and reentry in a fibrosis model based on imaging data,” *Heart Rhythm*, vol. 13, no. 7, pp. 1536–1543, 2016.
- [56] N. Cusimano, A. Bueno-Orovio, I. Turner, and K. Burrage, “On the Order of the Fractional Laplacian in Determining the Spatio-Temporal Evolution of a Space-Fractional Model of Cardiac Electrophysiology,” *PLoS ONE*, vol. 10, no. 12, 2015.
- [57] A. Bueno-Orovio, D. Kay, V. Grau, B. Rodriguez, and K. Burrage, “Fractional diffusion models of cardiac electrical propagation: role of structural heterogeneity in dispersion of repolarization.,” *Journal of the Royal Society, Interface*, vol. 11, no. 97, p. 20140352, 2014.
- [58] D. E. Hurtado, S. Castro, and A. Gizzi, “Computational modeling of non-linear diffusion in cardiac electrophysiology: A novel porous-medium approach,” *Computer Methods in Applied Mechanics and Engineering*, vol. 300, pp. 70–83, 2016.
- [59] J. P. Keener and a. V. Panfilov, “A biophysical model for defibrillation of cardiac tissue.,” *Biophysical journal*, vol. 71, no. 3, pp. 1335–45, 1996.

- [60] T. Seidel, J. C. Edelmann, and F. B. Sachse, “Analyzing Remodeling of Cardiac Tissue: A Comprehensive Approach Based on Confocal Microscopy and 3D Reconstructions,” *Annals of Biomedical Engineering*, vol. 44, no. 5, pp. 1436–1448, 2015.
- [61] R. F. M. van Oers, E. G. Rens, D. J. LaValley, C. a. Reinhart-King, and R. M. H. Merks, “Mechanical cell-matrix feedback explains pairwise and collective endothelial cell behavior in vitro,” *PLoS computational biology*, vol. 10, p. e1003774, 2014.
- [62] J. Kucera, S. Rohr, and Y. Rudy, “Localization of sodium channels in intercalated disks modulates cardiac conduction,” *Circulation research*, vol. 91, no. 12, pp. 1176–1182, 2002.
- [63] S.-S. Zhang and R. M. Shaw, “Trafficking highways to the intercalated disc: new insights unlocking the specificity of connexin 43 localization,” *Cell communication & adhesion*, vol. 21, pp. 43–54, 2014.
- [64] O. C. Rodriguez, A. W. Schaefer, C. A. Mandato, *et al.*, “Conserved microtubule–actin interactions in cell movement and morphogenesis,” *Nature Cell Biology*, vol. 5, pp. 599–609, 2003.
- [65] J. W. Smyth and R. M. Shaw, “Forward trafficking of ion channels: What the clinician needs to know,” *Heart Rhythm*, vol. 7, pp. 1135–1140, 2010.
- [66] I. V. Kazbanov, K. H. W. J. ten Tusscher, and A. V. Panfilov, “Effects of Heterogeneous Diffuse Fibrosis on Arrhythmia Dynamics and Mechanism,” *Scientific Reports*, vol. 6, p. 20835, 2016.

Chapter 5

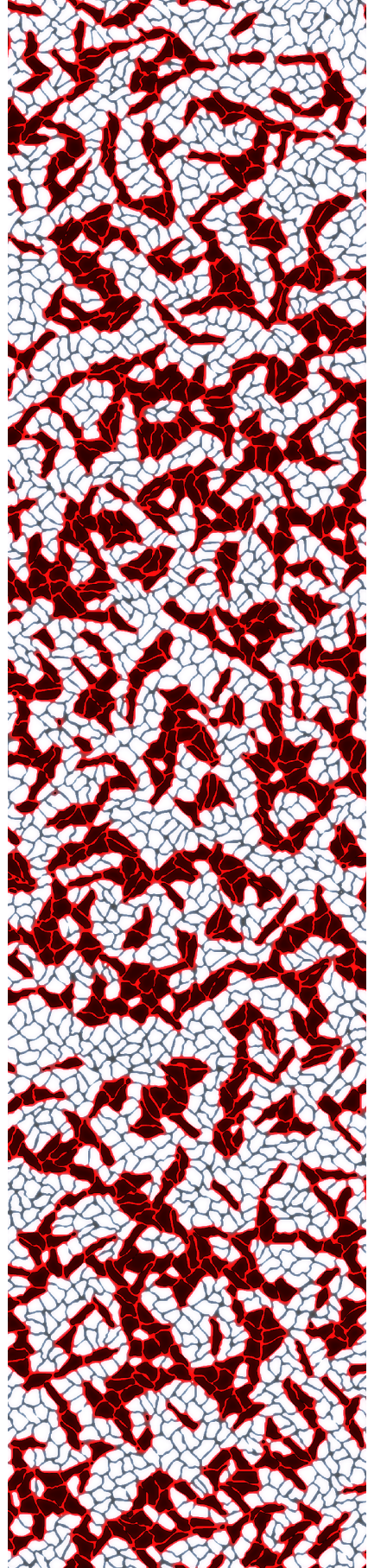
Self-organization of conducting pathways explains electrical wave propagation in cardiac tissues with high fibrosis

Nina Kudryashova^{1,2}, Valeriya Tsvelaya¹, Aygul Nizamieva¹, Alexander Panfilov², and Konstantin Agladze^{1,*}

¹Laboratory of Biophysics of Excitable Systems, Moscow Institute of Physics and Technology, Dolgoprudny, 141701, Russia

²Department of Physics and Astronomy, Ghent University, Ghent, 9000, Belgium

*kagladze@gmail.com



Abstract

Cardiac fibrosis occurs in many forms of the heart disease and is considered to be one of the main arrhythmogenic factors. The most dangerous cardiac arrhythmias arise from a block of wave propagation, which is most likely to occur in the regions with high density of fibrosis. Therefore, understanding of the wave propagation in the regions with a high percentage of fibrosis is very important. However, the precise mechanisms leading to arrhythmia formation in fibrotic cardiac tissue remain poorly understood. Particularly, it is not clear how wave propagation is organized at the cellular level, as experiments show that the regions with a high percentage of fibrosis (65-75%) are still conducting electrical signals, whereas geometric analysis of randomly distributed cells predicts connectivity loss at 40% at the most (percolation threshold). To address this question we used a joint *in vitro-in silico* approach, which combined experiments in neonatal rat cardiac monolayers with morphological and electrophysiological computer simulations. We have shown that the main reason for sustainable wave propagation in fibrotic samples is the formation of a branching network of cardiomyocytes. We have successfully reproduced the morphology of conductive pathways in computer modeling, assuming that cardiomyocytes align their cytoskeletons to fuse into cardiac syncytium. The electrophysiological properties of the monolayers, such as conduction velocity, conduction blocks and wave fractionation, were reflected as well. In a virtual cardiac tissue, we could also examine the wave propagation on the subcellular level in much more detail than in experiment, which allowed us to detect the wavebreaks formation, analyse the structure that caused them, and explain how fibrosis leads to re-entry onset.

Keywords: cardiac tissue development, cardiac remodelling, arrhythmias

Introduction

The contraction of the heart is controlled by propagating waves of excitation. Abnormal regimes of the wave propagation, or *cardiac arrhythmias*, cause asynchronous contractions and may even result in cessation of the blood flow. Irregular wave propagation often originates from blocks of propagation [1]. The wave goes around the block, re-enters the same region and forms a persistent cycle, or so-called *cardiac re-entry*, which is one of the main mechanisms of cardiac arrhythmias.

The normal heart has a complex structure, which is composed of the bundles of elongated cardiac cells. Apart from excitable cardiac cells, there are also inexcitable cells of connective tissue: *cardiac fibroblasts*. Their role is to maintain the structural integrity of the heart [2] and repair injuries [3]. They even outnumber cardiomyocytes in a healthy human heart although occupying a much smaller total volume [2, 4]. Excessive growth of the fibrous tissue, called *cardiac fibrosis*, is considered to be one of the main arrhythmogenic factors [5, 6]. However, the mechanisms that trigger waveblocks and cardiac arrhythmias remain poorly understood.

The fibrosis slows down wave propagation [7] and can completely block the wave propagation if the fibroblasts' density is high. The critical density of fibrosis above which the conduction terminates is called *percolation threshold*. This concept originates from the percolation theory, and, by definition, it specifies the point of long-range connectivity formation in random systems. Percolation threshold plays an important role in arrhythmogenicity. It was shown that cardiac tissue is most susceptible to arrhythmias if the density of fibrosis is only slightly below the percolation threshold [8]. There are two main reasons for it. First, a larger amount of fibroblasts, which act as heterogeneities, increases the probability for waveblocks. Second, a high fraction of fibrosis creates a maze that effectively lengthens the travel distance for the waves, as they follow a longer zig-zag path [9].

Up to now wave propagation failure was studied only in generic mathematical representations of cardiac fibrosis with each cell randomly chosen to be either myocyte or fibroblast. In this kind of 2D computer models, the propagation of excitation failed at 40% of fibrosis [10], which is within the range of

values predicted by classic mathematical models (37-44% of the area uncovered by conducting elongated ellipses with the shape similar to cardiomyocytes [11]). However, experimental measurements [12] indicate that wave propagation and synchronous contraction in 2D cardiac monolayers is observed for up to 75% percentage of fibrosis.

In this paper, we study the phenomenon of the wave propagation in cardiac tissue with a high density of fibrosis using a joint *in silico-in vitro* approach. We performed experiments in 40 monolayers with various percentages of fibroblasts and detected wave propagation to determine the percolation threshold. We have found that, indeed, the experimentally measured threshold (75% of the area covered by fibroblasts) is substantially higher than what was predicted in computer modeling (40% [10]) or classic mathematical models. Further morphological examination revealed that the key mechanism of conduction in highly fibrotic tissue is likely to be tissue patterning. The cardiomyocytes were not located randomly but organised in a branching network that wired the whole sample.

Next we applied a cellular model of virtual cardiac monolayer [13], based on the Cellular Potts Model, to explain cardiac network formation. We proposed a hypothesis that such self-organisation occurs due to cytoskeletons' alignment. With this model, we were able to obtain branching patterns observed in experiments, as well as reproduce the decrease in conduction velocity and wave percolation. In addition, simulations allowed us to detect wavebreaks leading to reentry formation, and analyse the tissue structure that caused them.

This paper is organized as follows. First, we describe the experiments conducted with the neonatal cell cultures that revealed the surprisingly high percolation threshold in cardiac monolayers. Second, we analyse patterns formed in these monolayers and we propose the hypothesis for the mechanism of their formation. Third, we demonstrate pattern formation *in silico* in a Cellular Potts Model (CPM) of cardiac tissue [13]. Next, we compare electrical signal propagation in computer modeling and in experiment. Finally, we show a spontaneous formation of uni-directional blocks in the model which resulted in re-entry formation.

Results

5.2.1 Experimental study of the percolation threshold in neonatal rat cardiac monolayers

We cultured neonatal rat ventricular cardiomyocytes mixed with cardiac fibroblasts in variable proportion (20-88% fibroblasts) and studied electrical activity in these monolayers using optical mapping.

In Figure 5.1a and in Supplementary Video 1 the wave propagation in a sample with high fibrosis is shown (66% fibroblasts). In spite of high percentage of fibrosis, this sample is still conducting electrical waves, however the wave propagation pattern is complex. The wave originates from the stimulation point marked by a yellow spike at the bottom of the tissue and initially spreads in all directions. However, due to a large number of fibroblasts the wave gets blocked at multiple sites. After a short delay (in areas outlined with dashed

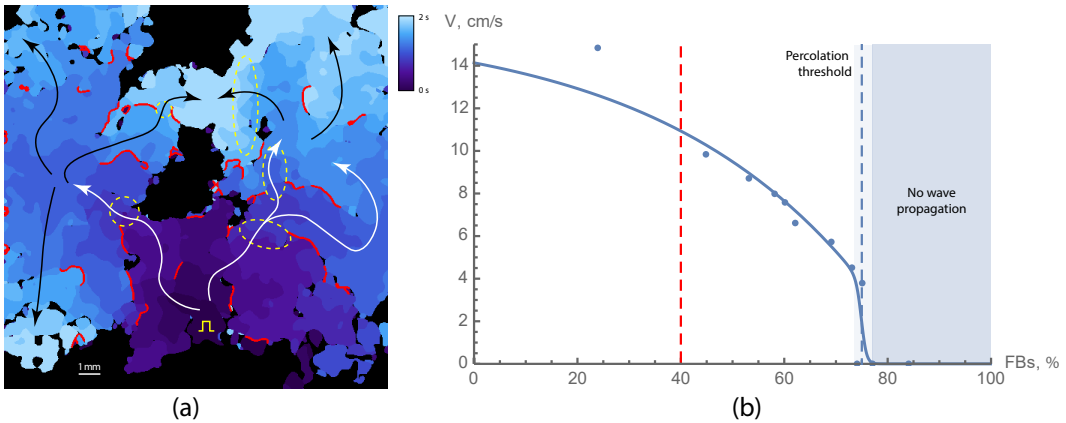


Figure 5.1: (a) Wave propagation in a neonatal rat cardiac monolayer with 66% of fibroblasts. Activation times are colour coded. Red lines show the regions where the wave was blocked. White and black arrows show the main propagation pathways. Yellow square pulse sign indicates the location of the stimulating electrode. Yellow dashed lines outline the areas of slow conduction. The original video (Supplementary Video 1) of the wave propagation is available at <https://youtu.be/3aDmsT1p13Y>. (b) Velocity decay with the increase of the portion of fibroblasts in samples. The percolation threshold is shown with the dashed line and was equal to $75 \pm 2\%$.

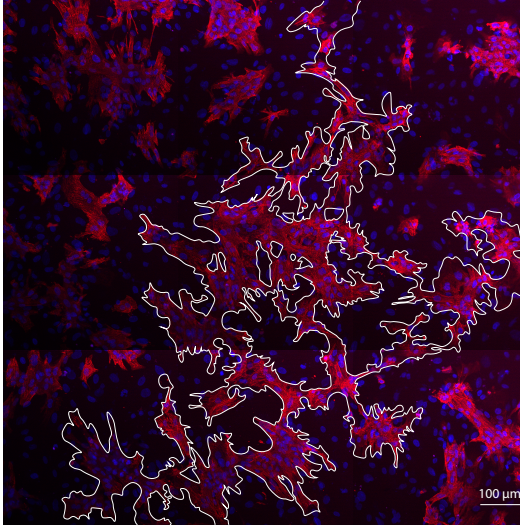


Figure 5.2: Conducting pathway in a monolayer of cardiac tissue with 31% of cardiomyocytes and 69% of fibroblasts. The interconnected region is outlined in white. Cardiomyocytes are labeled with anti- α -actinin antibody and coloured in pink. Nuclei are shown in blue.

ellipses), the wave propagates further into the left and the right parts of the sample, and again spreads in diverse directions. This process repeats multiple times, resulting in a complex, fractionated wave pattern containing narrow pathways and some bulk excited regions. The conduction blocks in Figure 5.1a are shown in red, which are the places where the wave propagation was blocked and the wave had to go around. The main propagation paths are shown with white and black arrows. In this sample, the electrical wave propagation was still possible, however the amount of fibroblasts was close to the percolation threshold. We see that a few additional blocks could drastically change the wave propagation and subdivide the sample into several disconnected parts.

We have found that the percolation threshold for the neonatal rat cardiac monolayers was $75 \pm 2\%$ of fibroblasts. We have also measured conduction velocities in the samples above the percolation threshold (Figure 5.1b). The velocity decreased when approaching the percolation threshold. In the samples with low fibrosis, the velocity was approximately 12 cm/s, and it decreased twofold in the samples with 70% fibrosis. The number of conduction blocks was higher in samples with high fibrosis. As a result, the mean conduction velocity decreased with the increase in a percentage of fibroblasts.

After optical mapping of the wave propagation was recorded, we have fixated the samples and studied their morphology using immunohistochemical labeling. We have found that the cardiomyocytes in the samples capable of

electrical wave propagation have formed connected networks. In Figure 5.2 cardiomyocytes are shown in pink, and the cluster that they have formed is outlined with a white contour. The cardiomyocytes were organised in a branching structure that wired the whole sample. We have followed the pathway using a confocal microscope and it was possible to find long-range connectivity in the tissue. Therefore, we observed that the cardiomyocytes were organised in conduction pathways and assumed that there must be a mechanism responsible for their self-organisation.

5.2.2 Formation of branching structures in a computer model

After trying several models that were previously used in developmental biology to create branching structures, we have finally succeeded to reproduce the pattern by including one specific property of cardiomyocytes. This property was the alignment of the cytoskeletons of the neighbouring cells. Alignment of the actin fibres is clearly seen in our experimental preparations. In Figure 5.3 the bundle of neonatal rat cardiomyocytes is shown. The red arrows indicate the intercalated disks between the cells. The white arrows point at the actin

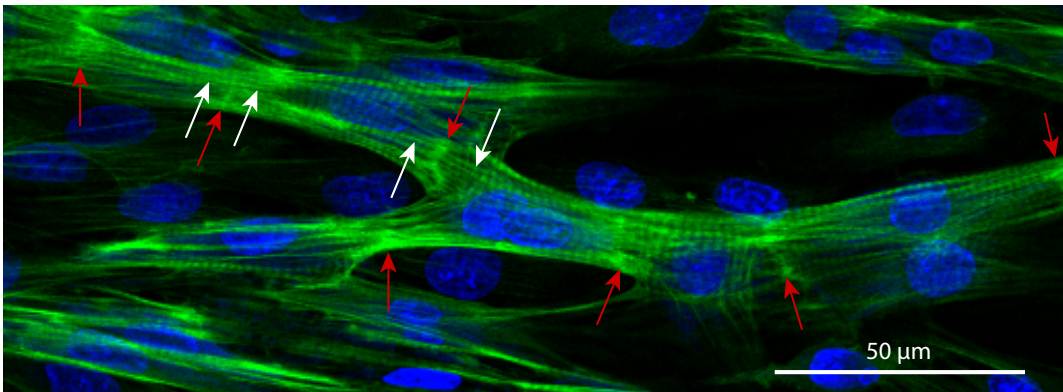


Figure 5.3: Cardiac syncytium in a 3-days culture of the neonatal rat cardiomyocytes. The cells have formed intercalated disks (ID, bright-green, highlighted with red arrows), aligned their cytoskeletons (the aligned strains on the both sides from ID are shown with white arrows) and formed a branching network. Nuclei are shown in blue (DAPI, labels DNA), and actin strands are shown in green (phalloidin, labels F-actin).

bundles on the opposite sides of the intercalated disk, that smoothly continue one another.

The precise mechanism of such alignment is unknown. We hypothesized that the mechanism which can account for alignment can be derived from a well-known property of actin cytoskeleton reinforcement in response to the external force [14]. Actin filaments, as well as the adaptors that link them, remodel under applied tension. In case of contact of two cells, the actin filaments are connected through adherens junctions, which transmit the tensile forces between the filaments of the neighbouring cells. It was shown that higher tension stabilises the whole complex [14]. The tension is maximal, if the actin filaments are aligned with each other, which gives a preference for intercellular alignment of the cytoskeletons.

We have incorporated this mechanism into our Cellular Potts Model (CPM) of cardiac cells [13]. This model was already adjusted to reproduce characteristic shapes of the cardiac cells in virtual tissue model, and here we extended it with a new energy term, that corresponded to the alignment of actin bundles in the neighbouring cells.

In our CPM model, cell-substrate adhesion sites, to which actin bundles are anchored, were represented as separate entities: specially labeled subcells of the lattice. If two adhesion sites of two cells came into contact, we established the connection between them. The connection means, that the new bond energy was applied to them. This energy depended on the angle between the linked actin bundles (see Figure 5.4). The minimum of the energy corresponded to smooth coupling between the bundles, or zero angle. In this case, the bond was the most stable, but couplings with the non-zero angle between the bundles had a tendency to break apart.

With this new energy term that favours cytoskeletons alignment, the cardiomyocytes in simulations created branching patterns. In Figure 5.5a a resulting simulated structure of the sample with 70% fibroblasts is shown. We see that in this sample only 30% of cardiomyocytes were able to build a network, and even with such a high density of fibroblasts, this network was fully interconnected. Our further studies showed that such interconnection was established for every sample with 30% of cardiomyocytes ($n = 10$) of $1\text{ cm} \times 1\text{ cm}$ size, which is close to the size of the Petri dish used in our experimentals. For

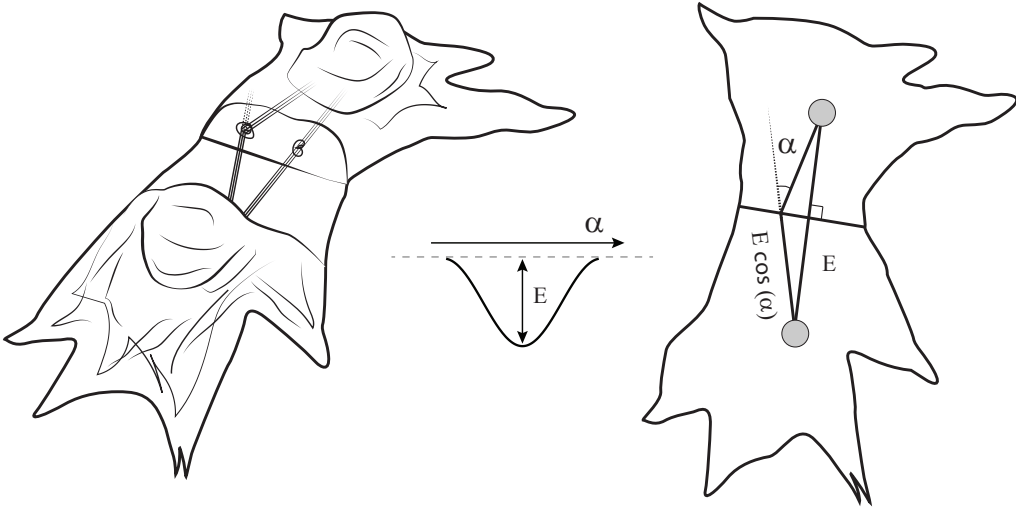


Figure 5.4: The schematic of the cell-to-cell interaction in a computational model. The energy term was assigned to every pair of connected actin bundles in coupled cells. This term depends on the angle between the bundles and reaches its minimal value when the bundles are aligned ($\alpha = 0$). Left image shows quasi-3D schematic of the cells, middle image shows energy profile and right image shows a view from the top.

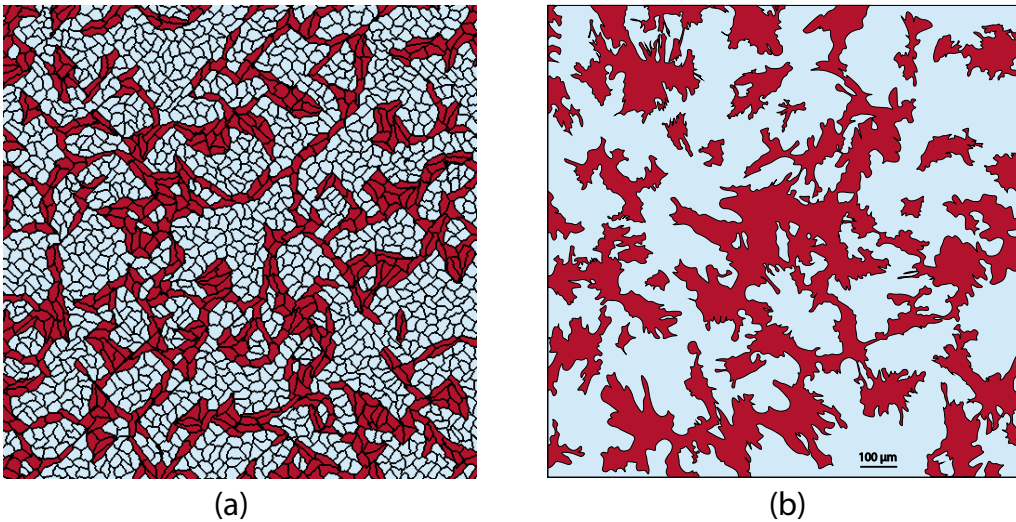


Figure 5.5: The branching pattern obtained in a computer model (a) compared to one observed in an experiment (b). (a) A virtual sample with 70% of fibroblasts. (b) A segmented image of the experimental sample with 66% of fibroblasts. The original image is shown in Figure 5.2.

samples with 28% of cardiomyocytes the network was interconnected in 20% of cases. We also see that the patterns in computer simulation (Figures 5.5a) and in experiment (Figures 5.5b) have similar features, such as long single-cell-wide connections that bridged the gaps between cell clusters, or isolated clusters of fibroblasts trapped within the main cardiac pathway. Therefore, using the hypothesis on cytoskeletons' alignment allowed us to reproduce the main features of the pattern.

Using this model with cytoskeleton alignment, we have studied further wave excitation patterns and the percolation threshold for electrical waves in the system.

5.2.3 Wave propagation in virtual cardiac tissue monolayers

We have reproduced the experiments from Figure 5.1a *in silico* using Majumder et al. [15] model for neonatal rat ventricular cardiomyocytes.

Figure 5.6a and in Supplementary Video 2 show the wave propagation in a virtual sample with 70% fibroblasts. The wave propagation pattern is complex and similar to one observed in experiment (see Figure 5.1a). One can see, that the number of percolation blocks per unit area is similar to that of the experimental activation pattern, and the trajectories of the waves share the same features. Note, that the scale of the simulated activation map is slightly smaller than those of the experimental one.

The percolation threshold in virtual cardiac monolayers was equal to $71.5 \pm 1.5\%$ of fibroblasts, meaning that 100% of the samples ($n = 10$) with 70% fibrosis were interconnected, whereas samples with more than 73% fibrosis ($n = 10$) were never conducting. For 72% fibrosis 20% of the samples were functional and for 71% fibrosis, those were 80%. The conduction velocity dependence on the density of fibrosis is shown in Figure 5.6b. For each simulated sample we have indicated the mean value of the velocity, and the standard deviation of the velocity distribution was shown with error bars. One can see, that the velocity decay is similar to one measured in experiments (see Figure 5.1b). Closer to the percolation threshold the fluctuations in conduction velocities amplified due to the stochastic nature of the percolation block. Moreover,

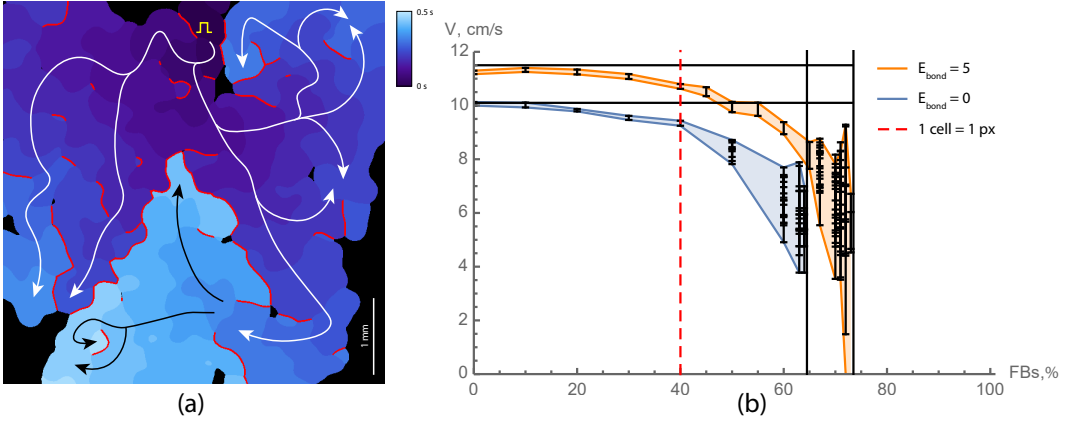


Figure 5.6: **(a)** Wave propagation in a neonatal rat cardiac monolayer with 70% of fibroblasts. Activation times are colour coded. Red lines show the regions where the wave was blocked. White and black arrows are showing the main propagation pathways. Yellow square pulse sign indicates the location of the stimulating electrode. **(b)** Velocity decay with the increase of the fibrosis density. Orange lines represent velocities in virtual samples with cytoskeletons alignment ($E_{bond} = 5$), and blue lines without ($E_{bond} = 0$). Waves propagation in samples with branching patterns (orange) was failing in part of the samples starting from 71% and not possible in all of the samples for $\geq 75\%$. For each density 10 samples with the size of $5 \text{ mm} \times 5 \text{ mm}$ were tested. For each sample the distribution of velocities is shown (mean \pm SD).

variations in conduction velocities within one sample were very high, because of a large number of conduction blocks.

The percolation threshold in our simulations was slightly lower ($\approx 72\%$) than in experiment (75%). However, both values are much higher than the predictions of the models with random cells distribution (40%). Also, the range of fibroblasts' densities, for which the conduction failure was uncertain, was small both in experiments and in simulations. We suggest that self-organisation significantly reduced this range, which was two times smaller in our simulations and experiments (3%), than in an earlier paper with random cell distribution (6% [16]). It can be explained by the fact, that self-organisation reduces the uncertainty in the system: if there were enough cells in the sample, they could organise in a branching pattern. Therefore, the abrupt change in probability to conduct electric waves also supports our hypothesis, that self-organisation events take place in fibrotic cardiac tissue.

5.2.4 The uni-directional block and spontaneous reentry onset were observed in virtual cardiac monolayers with high fibrosis

We have shown that in virtual tissues the spontaneous onset of reentry can occur. It was observed in samples with a high level of fibrosis. Figure 5.7 shows such process for a sample with 70% fibrosis. We see that after the first stimulus applied to the left border of the sample (shown in yellow), the wave propagation was blocked at the lower part of the sample, but continued propagation through the upper part. After reaching the right border, the wave turned around and entered the bottom region. However, this first wave was blocked in the middle of the sample, as the tissue in the upper part of the sample did not recover. The wave from the second stimulus, applied at the same site, has followed the same path and formed a sustained circulation along the path shown with the red dashed line in Figure 5.7.

Detailed analysis of the structure revealed that formation of a reentry here is solely due to specific structure which is shown in the middle (inside the yellow square) and acts as an area of uni-directional block (or “diode”): the waves can propagate from right to left, but not in the opposite direction. The diode is formed by two cell clusters that barely touch each other. These cell clusters have slightly different areas adjacent to this connection. Therefore, if the wave propagates from left to right (from a smaller cluster to a larger one), then the small cell does not produce enough current and can not depolarise a bigger one. The transmembrane potential in the largest cluster raises (which is shown in red colour), but not enough for the sodium channels to open. This effect is called *source-sink mismatch* [1]. When the source (a smaller cluster) is insufficient compared to the sink (a larger inactive cell cluster), the wave propagation gets blocked. This effect was observed in chemical systems [17] and later in cardiac monolayers [18].

In a sample in Figure 5.7 the “diode” may initiate a reentry if the sample is stimulated from the left or from the top with a high frequency (4 Hz or more).

We have performed studies in 6 large samples with 70% of fibroblasts. All of these samples had 2-5 areas of the uni-directional block and many bi-directional blocks, but only one of these samples was arrhythmogenic. Thus,

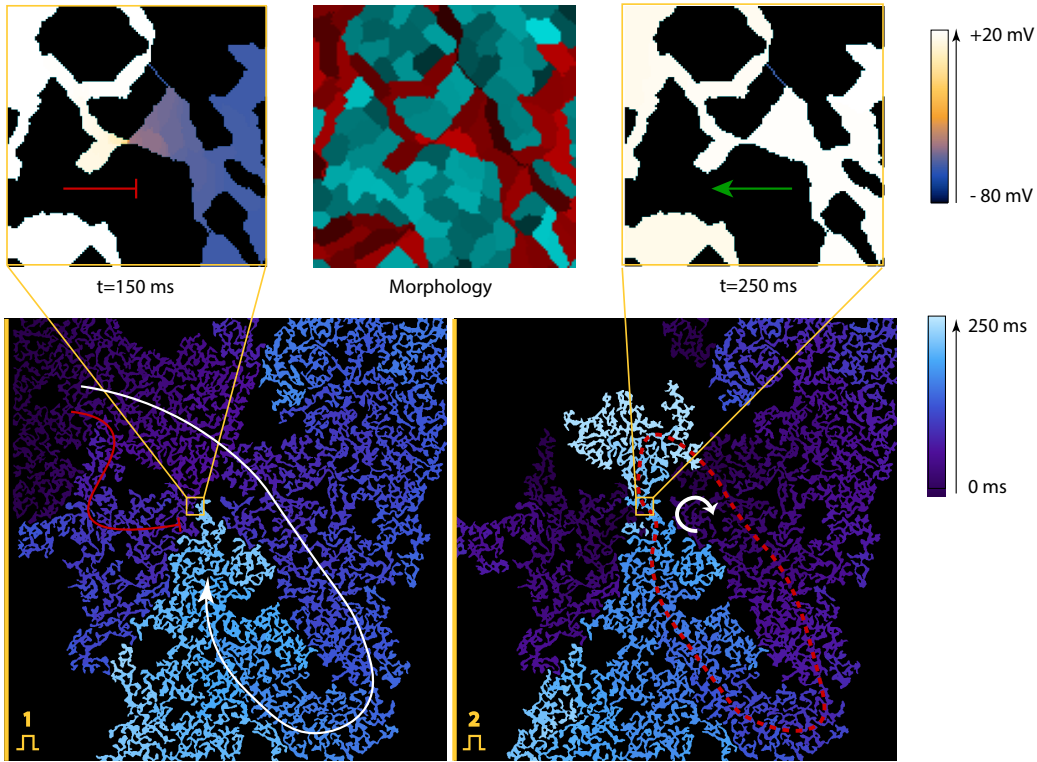


Figure 5.7: Spontaneous formation of the structure, that produces a uni-directional block, which results in reentry formation. The virtual sample had 30% of cardiomyocytes. Images on top show the insets of the place, where a uni-directional clock has occurred: the central image shows its morphology and images on the side show wave propagation in different directions. The voltage on the top images is colour coded. In the central image, cardiomyocytes are represented with red tints and fibroblasts with cyan. The bottom images show the whole sample. The bottom-left image shows the uni-directional block after the first stimulus, which was applied on the left boundary. The bottom-right image shows the reentry formation after the second stimulus. The activation times are colour coded. The arrows show the main wave paths. The red dashed line represents the reentry cycle.

in addition to “diodes”, some extra geometrical conditions are required. The precise conditions are to be studied in the future, however, they are related to the presence of the long conducting circuits in the tissue. In fact in Figure 5.7 we see that apart from the diode, there is also a loop, which is shown with a red dashed curve in the bottom-right image. The diode is a part of this loop, however, the loop is large enough to account for recovery of the bottom part of

the tissue after one rotation. The samples with a higher density of fibrosis were even less likely to have long circuits, thus we didn't observe sustained reentry there. We concluded, that reentry formation requires not only uni-directional blocks but also long circuits, and the intermediate densities of fibrosis are the most arrhythmogenic ones. This result was previously shown for random cell distributions, that reentry is most likely to occur 5-10% below the percolation threshold [8]. The principle holds true in our model, but quantitatively the densities of fibrosis are different.

Our model shows, that the areas of the uni-directional block can be naturally formed during tissue growth. Every time one spreading cell comes in contact with the other cell cluster, there is a chance that this connection will be asymmetric. It may explain the fact that reentries are frequently observed in the experimental setups with cardiac monolayers.

Discussion

We have observed paradoxical electrical wave propagation in samples with up to 73–75% of fibroblasts instead of mathematically predicted 40% for randomly distributed cells. We have shown both *in vitro* and *in silico*, that electrical wave propagation was possible due to the formation of the conduction pathways that rewired the whole monolayer. We have proved the existence of this branching network with immunohistochemical images. We have measured the conduction velocity, which decreased with the increase of the portion of fibroblasts in the monolayer in a similar way in experimental and computational studies. Assuming that cardiomyocytes align their cytoskeletons to fuse into cardiac syncytium, the morphology of conductive pathways was successfully reproduced in computer modeling as well as the electrophysiological properties of the monolayers.

To explain the formation of the pathways, we have considered several hypotheses. First, we suggested that differential adhesion together with cell elongation may be enough to explain this patterning. A similar system with autonomously elongating cells was successfully used to explain vasculogenesis [19]. However, we did not impose obligatory elongation on the cardiac cells, because they are not necessarily elongated according to our experimen-

tal observations. Cardiomyocytes obtain their typical brick-like shape with the guidance of the extracellular matrix over the course of development. However, there is no evidence for any internal autonomous mechanism for elongation. In experiments on the glass, cells were not only bipolar but also tripolar and multipolar. In our model, this feature was reproduced with explicit introduction of the actin bundles. Similar approach was previously used to describe the shapes of dendritic cells [20]. Cooperation between aligned actin bundles pulling in one direction shaped the cell more efficiently, which resulted in clustering of these bundles and multipolar cell shapes. Therefore, since the elongation was not imposed, there was no mechanism forcing cardiomyocytes out of clusters to search for new connections.

Next, we considered various mechanisms that were previously used to explain similar branching patterns in angiogenesis. The main sources of instability in those models were chemotaxis and contact-inhibition [21]. The percolation in the networks formed due to sharp gradients of chemoattractants was also studied previously in a continuous model [22]. However, there was no evidence for directed migration of cardiac cells and for type-specific contact-inhibition, similar to those that select a tip cell in a growing blood vessel. Therefore, we discarded this hypothesis either.

This mechanism is similar to *diffusion limited aggregation*: a process in which random-walking particles form fractal aggregates. In our model, a cell does not only stick to the growing pattern but also aligns its orientation with it. The mechanism for it actually exists as a part of syncytium formation, when cardiomyocytes fuse and align their cytoskeletons. Once a cell aligns cytoskeleton with its neighbours, this structure matures and fixes the cell in place. In some sense, this process causes contact-inhibition only between cardiomyocytes and not between cardiomyocytes and fibroblasts, which results in the branching structure like one shown in angiogenesis [21].

Formation of conduction pathways and complex texture of the tissue may be important not only in terms of arrhythmogenicity. For example, it was shown that texture of cardiac tissue at subcellular level can substantially affect the propagation of external current during defibrillation [23, 24]. Therefore, it will be interesting to perform a similar study for the textures generated with our model.

There are several limitations of the methods used in this study. First of all, we have conducted experiments with cell cultures, which are different from the real cardiac tissue. It would be interesting, yet more complicated, to study patterning of the real 3D cardiac tissue. However, the mechanisms of patterning that we discovered here could be universal and might be applicable to the real cardiac development as well. Second, fibrosis is a more complex condition than just excessive growth of fibroblasts, which also involves collagen deposition. The collagen electrically insulates the cardiac fibers from one another and is also considered to increase arrhythmogenicity. In this study, we did not take the extracellular matrix into account, but it would be also interesting to measure its effect on the percolation threshold in the future studies. Finally, percolation depends on the size of the sample and scales with this size. For random systems, the scaling laws are known. In our case, we did not consider scaling and used similar size of the samples *in silico* as in the experiment. However, it would be interesting to study scaling of the percolation threshold and see how the size can affect the probability of wavebreak formation.

We conclude, that the cardiomyocytes in fibrotic areas can form a connected network and allow electrical signal propagation in monolayers containing up to 75% of connective tissue.

Methods

5.4.5 Experimental samples preparation

Neonatal cardiac cell isolation. All studies conformed to the Guide for the Care and Use of Laboratory Animals, published by the United States National Institutes of Health (Publication No. 85-23, revised 1996) and approved by the Moscow Institute of Physics and Technology Life Science Center Provisional Animal Care and Research Procedures Committee, Protocol #A2-2012-09-02. In this study, we used enzymes adapted to the existing two-day protocol selection from Worthington-Biochem¹. Cardiac cells were isolated from the ventricles of rat pups (*Rattus norvegicus*, Sprague Dawley breed) with different ages (1–4 days). Then, the isolated cells were seeded on the specimens covered

¹<http://www.worthingtonbiochem.com/NCIS/default.html>

with fibronectin (0,16 mg/ml, Gibco, USA, 33016015) at different concentrations before they were cultivated in DMEM culture medium (Gibco, USA, 11960) with 5% of FBS (foetal bovine serum, Gibco, USA, 10100147). For the study of the shapes of the isolated cells, the cells were seeded at $5 \cdot 10^3$ cells/cm². After 3 days of cultivation, the samples were fixated. The monolayers of primary culture cells were seeded at $30 \cdot 10^3$ cells/cm², and after 3–5 days monolayers were used in morphometrical studies and optical mapping.

Immunohistochemical staining. The cells were fixated with 5% PFA (paraformaldehyde powder, 95%, Sigma-Aldrich, USA, 158127-100G), and nuclear staining was performed with DAPI (VECTASHIELD Mounting Medium with DAPI, Vector, USA, Cat. No. H-1200). In our work, we used anti- α -actinin (Sigma-Aldrich, USA, A7811) and alexa fluor 594 like Secondary Antibody (A-11020, Life Technologies) for CM-specific labelling, Alexa Fluor 488 phalloidin (Molecular Probes, USA, A12379) for F-actin non-specific staining and DAPI for labelling cell DNA. Pictures were taken with an inverted fluorescence microscope (Axio Imager with ApoTome optical sectioning module, Zeiss). Immunofluorescent staining of the CMs was performed with the use of secondary and primary antibodies according to a previously described protocol². Signals from each fluorescent label were recorded in a corresponding wavelength range. Channels were then pseudo-coloured and merged together.

Optical mapping. To monitor activity and record the excitation patterns, the 3- to 5-day-old monolayers were loaded with the Ca²⁺-sensitive indicator Fluo-4-AM (Molecular Probes, USA, F14201). After staining, the medium was exchanged with Tyrode's solution (Sigma-Aldrich Co., USA, T2145-10L) and kept at room temperature during the observations. The excitation waves were monitored with a high-speed imaging setup (Olympus MVX-10 Macro-View fluorescent microscope equipped with high-speed Andor EM-CCD Camera 897-U at 68 fps). All videos were processed with ImageJ software.

Velocity measurements To measure velocity of excitation wave propagation, especially for samples with low concentration of CMs and thereby fluc-

²<http://www.abcam.com/protocols/immunocytochemistry-immunofluorescence-protocol>

tuating velocity values, 10 space intervals for each sample were selected. The velocity was measured for each interval and after the mean velocity and standard deviation were calculated.

Cell counting Two techniques were applied for cell counting. After immunostaining, cells were counted either manually or by means of cytofluorometry. For manual counting cells' nuclei stained with DAPI represented the overall number of cells, while only those within α -actinin stained fibers were accounted for cardiomyocytes. The second method was performed on cytofluorometer (Accuri C6, BD Biosciences, USA) by distinguishing non-cardiomyocytes, stained only for F-actin, from CMs, stained both for F-actin and α -actinin

Mathematical model for cardiac tissue growth

In this study we have used previously developed mathematical model for cardiac monolayers formation [13]. It is based on the Cellular Potts Model (CPM) formalism, which describes cells as the domains of the regular lattice and assigns energy to the system of cells to describe their growth and motility. In our previous work [13], we have selected the main features of the cardiac cells and parametrised our model to reproduce the cell shapes. In this study, we extended the model with a new energy term responsible for syncytium formation.

The evolution of the cardiac monolayer is described by the Hamiltonian:

$$H = H_{\text{adhesive}} + H_{\text{elastic}} + H_{\text{protr}} + H_{\text{nuclei}} + H_{\text{junctions}}, \quad (5.1)$$

where $H_{\text{adhesive}} + H_{\text{elastic}}$ is the basic CPM model and H_{protr} is the term describing the protrusion dynamics of the cardiac cells, which produces a characteristic polygonal shapes of these cells. H_{nuclei} corresponds to higher rigidity of the nuclei compared to the cell body. Finally, $H_{\text{junctions}}$ is a new term, that describes the stability of adherens junctions and alignment of the cytoskeletons of the neighbouring cells.

The core feature of the model of cardiac cells is the explicit representation of cell attachments as special labels on the lattice subcells. They first appear when the cell expands, and can be destroyed with a certain penalty, if, for

example, the cell is stretched due to the movement in other direction. The number of attachments per cell is limited by the amount of actin present in the cytoplasm, which is also reflected in a model. If the maximal number of attachments is reached, the new attachments do not form.

H_{protr} is an energy term, that decreases with the distance from the centre of mass of the cell, and which is applied only to these labeled attachment sites. As a result, the attachment sites spread out and reproduce a characteristic polygonal shape of the cardiac cells. Here we omit the details of the spreading process, which involves polymerization and depolymerisation of the actin, attachment/detachment, etc., but we mimic the overall dynamics of the protrusion. Also, we assume, that for every attachment cite a corresponding actin bundle exists, which stretches from the attachment cite towards the proximity of the nuclei.

If two attachment cites in the neighbouring cells come into contact, the bond between these attachment cites can be formed. In the algorithm, this bond appears if one attachment cite attempts to move over the other. Instead of copying of the subcell in this case the connection establishes. A new energy term $H_{\text{junctions}}$ applies to the subcells, which are involved in an established junction. This term determines the stability of the cell-to-cell junction and depends on the angle between the actin bundles, associated with the attachment cites involved (see Figure 5.4). It is determined as follows:

$$H_{\text{junctions}} = \sum_{\substack{\vec{i}, \vec{j} \\ \text{labeled junction}}} E_{\text{bond}}(1 - \cos(\alpha_{i,j})),$$

where $\alpha_{i,j}$ (also shown in Figure 5.4) is the angle between two cytoskeleton bundles of two neighbouring cells which ends at points i and j and are labeled as an established junction. The higher is the angle, the less stable is the junction. Therefore, the junctions with continuous actin bundles on both sides persist, but the kinked bundles tend to lose the connection. As a result, the actin bundles of the neighbouring cells tend to align and stay in the aligned state.

The parameters of the model used in simulations (see Table 5.1) in this paper were adjusted to compensate the additional energy term $H_{\text{junctions}}$. The

Table 5.1: Parameters of the morphological model used in stimulations. CM—cardiomyocytes, FB—fibroblasts.

Parameter	Units	CM	FB
Temperature T	1.0	1.0	
G_N	mm	100.0	20.0
V_t	$\cdot 10^3 \mu\text{m}^2$	0.9	0.8
λ	mm^{-4}	60.0	20.0
P_{detach}		11.0	10.0
$J_{\text{Cell-MD}}$	mm^{-1}	600.0	275.0
$J_{\text{Cell-Cell}}$		700.0	500.0
$J_{\text{CM-FB}}$		700.0	
L_{MAX}	μm	40.0	40.0
N_{protr} (fixed)		14	8
E_{bond}		5.0	-
Sample dim.	$\text{mm} \times \text{mm}$	4.8×4.8	
Simulation time	MCS	50 000	
Number of cells	1	162×162	

most of them are close to the parameters used in our original paper [13]. The maximal value of the new energy term was set to $E_{\text{bond}} = 5.0$, which provided enough stability for the junctions to maintain the branching structure but at the same time not too much stability to allow cells to search for possible new connections. Addition of $H_{\text{junctions}}$ effectively increased the adhesion between cardiomyocytes. Therefore, the differential adhesion was toned down in a model to allow cardiomyocytes to migrate randomly before they mature and stick to the pattern. In this study we have changed type-specific adhesion coefficients $J_{\text{cell-cell}}$. Our choice of the parameters was guided by the desired balance between branching and clustering. Lower adhesion energy (J) to the cells of the same type increases the size of unstructured, irregularly shaped clusters. On the other hand high adhesion energy forced cells out of clusters. We have chosen neutral values of $J_{\text{CM-CM}} = J_{\text{CM-FB}}$, which meant that cardiomyocytes had no preference in neighbours. Their energy was equal for being surrounded with other cardiomyocytes or with the fibroblasts. The fibroblasts had a slight tendency to cluster ($J_{\text{FB-FB}} < J_{\text{CM-FB}}$). This choice

of parameter allowed us to qualitatively reproduce the patterns observed in experiments (see Figure 5.2 and 5.5).

5.4.6 Simulations of wave propagation

The virtual samples generated with the Cellular Potts Model were then used as a map for electrophysiological studies. The methodology was already described in our previous papers [13, 25].

Author contributions statement

K.A. conceived the experiments, A.N. and V.Ts. conducted the experiments, N.K. performed simulations under supervision of A.P. A.N., V.Ts. and N.K. analysed the results. All authors reviewed the manuscript.

References

- [1] A. G. Kléber and Y. Rudy, “Basic mechanisms of cardiac impulse propagation and associated arrhythmias,” *Physiological reviews*, vol. 84, pp. 431–88, 2004.
- [2] P. Camelliti, T. K. Borg, and P. Kohl, “Structural and functional characterisation of cardiac fibroblasts,” *Cardiovascular research*, vol. 65, no. 1, pp. 40–51, 2005.
- [3] P. Kohl and R. G. Gourdie, “Fibroblast-myocyte electrotonic coupling: does it occur in native cardiac tissue?,” *Journal of molecular and cellular cardiology*, vol. 70, pp. 37–46, 2014.
- [4] L. Yue, J. Xie, and S. Nattel, “Molecular determinants of cardiac fibroblast electrical function and therapeutic implications for atrial fibrillation,” *Cardiovascular research*, vol. 89, pp. 744–53, 2011.
- [5] S. de Jong, T. A. B. van Veen, H. V. M. van Rijen, and J. M. T. de Bakker, “Fibrosis and Cardiac Arrhythmias,” *Journal of Cardiovascular Pharmacology*, vol. 57, pp. 630–638, 2011.
- [6] T. P. Nguyen, Z. Qu, and J. N. Weiss, “Cardiac fibrosis and arrhythmogenesis: the road to repair is paved with perils,” *Journal of molecular and cellular cardiology*, vol. 70, pp. 83–91, 2014.

- [7] H. Arevalo, G. Plank, P. Helm, H. Halperin, and N. Trayanova, “Tachycardia in Post-Infarction Hearts: Insights from 3D Image-Based Ventricular Models,” *PLoS ONE*, vol. 8, p. e68872, 2013.
- [8] S. Alonso, R. W. Dos Santos, and M. Bär, “Reentry and Ectopic Pacemakers Emerge in a Three-Dimensional Model for a Slab of Cardiac Tissue with Diffuse Microfibrosis near the Percolation Threshold,” *PloS one*, vol. 11, no. 11, p. e0166972, 2016.
- [9] J. M. T. de Bakker and H. M. V. van Rijen, “Continuous and discontinuous propagation in heart muscle,” *Journal of cardiovascular electrophysiology*, vol. 17, pp. 567–73, 2006.
- [10] K. H. W. J. Ten Tusscher and A. V. Panfilov, “Influence of diffuse fibrosis on wave propagation in human ventricular tissue,” *Europace*, vol. 9, no. suppl_6, pp. vi38–vi45, 2007.
- [11] W. Xia and M. F. Thorpe, “Percolation properties of random ellipses,” *Physical Review A*, vol. 38, no. 5, pp. 2650–2656, 1988.
- [12] J. Rother, C. Richter, L. Turco, *et al.*, “Crosstalk of cardiomyocytes and fibroblasts in co-cultures,” *Open Biology*, vol. 5, no. 6, p. 150038, 2015.
- [13] N. Kudryashova, V. Tsvelaya, K. Agladze, and A. Panfilov, “Virtual cardiac monolayers for electrical wave propagation,” *Scientific Reports*, vol. 7, no. 1, p. 7887, 2017.
- [14] I. Schoen, B. L. Pruitt, and V. Vogel, “The Yin-Yang of Rigidity Sensing: How Forces and Mechanical Properties Regulate the Cellular Response to Materials,” *Annual Review of Materials Research*, vol. 43, no. 1, pp. 589–618, 2013.
- [15] R. Majumder, M. C. Engels, A. A. F. de Vries, A. V. Panfilov, and D. A. Pijnappels, “Islands of spatially discordant APD alternans underlie arrhythmogenesis by promoting electrotonic dyssynchrony in models of fibrotic rat ventricular myocardium,” *Scientific reports*, vol. 6, p. 24334, 2016.
- [16] S. Alonso and M. Bär, “Reentry near the percolation threshold in a heterogeneous discrete model for cardiac tissue,” *Physical Review Letters*, vol. 110, no. 15, 2013.
- [17] K. Agladze, R. R. Aliev, T. Yamaguchi, and K. Yoshikawa, “Chemical Diode,” *The Journal of Physical Chemistry*, vol. 100, pp. 13895–13897, 1996.
- [18] S. Rohr, J. P. Kucera, and V. G. Fast, “Paradoxical Improvement of Impulse

- Conduction in Cardiac Tissue by Partial Cellular Uncoupling,” *Science*, vol. 275, no. February, 1997.
- [19] R. M. H. Merks and J. A. Glazier, “Dynamic mechanisms of blood vessel growth,” *Nonlinearity*, vol. 19, pp. C1–C10, 2006.
- [20] J. B. Beltman, A. F. M. Marée, and R. J. De Boer, “Spatial modelling of brief and long interactions between T cells and dendritic cells,” *Immunology and Cell Biology*, vol. 85, no. 4, pp. 306–314, 2007.
- [21] R. M. H. Merks, E. D. Perryn, A. Shirinifard, and J. A. Glazier, “Contact-inhibited chemotaxis in de novo and sprouting blood-vessel growth,” *PLoS computational biology*, vol. 4, p. e1000163, 2008.
- [22] A. Gamba, D. Ambrosi, A. Coniglio, *et al.*, “Percolation, Morphogenesis, and Burgers Dynamics in Blood Vessels Formation,” *Physical Review Letters*, vol. 90, p. 118101, 2003.
- [23] J. P. Keener and A. V. Panfilov, “A biophysical model for defibrillation of cardiac tissue,” *Biophysical journal*, vol. 71, no. 3, p. 1335, 1996.
- [24] S. Luther, F. H. Fenton, B. G. Kornreich, *et al.*, “Low-energy control of electrical turbulence in the heart,” *Nature*, vol. 475, pp. 235–239, 2011.
- [25] A. V. Panfilov and A. V. Holden, “Computer simulation of re-entry sources in myocardium in two and three dimensions,” *Journal of Theoretical Biology*, vol. 161, no. 3, pp. 271–285, 1993.

Summary

The contraction of the heart is controlled by the propagating waves of excitation. Abnormal regimes of the wave propagation, or *cardiac arrhythmia*, often originate from the blocks of propagation. The wave goes around the block, re-enters the same region and forms a persistent cycle, or so-called *cardiac re-entry*, which is one of the main mechanisms of cardiac arrhythmias.

The normal heart has a complex structure, which is composed of the bundles of elongated cardiac cells. This complicated structure is believed to serve the optimal contraction and blood pumping. Cardiac bundles allow fast signal propagation in longitudinal, and slow propagation in the transversal direction. This phenomenon is called *anisotropy*. In this thesis, we have studied various aspects of anisotropy of the cardiac tissue, such as the formation of cardiac bundles, the origins of anisotropy and its effect on conduction block formation and arrhythmogenicity of the tissue. Apart from excitable cardiac cells, there are also inexcitable cells of connective tissue: cardiac fibroblasts. They even outnumber cardiomyocytes in a healthy human heart. The interaction between these cell types results in a complex tissue morphology, which contributes to anisotropy and stability of the wave propagation.

In **Chapters 1 and 2** we have proposed a new scenario of re-entry formation caused by an abrupt change in anisotropic direction. We have shown that the border zone between the regions with different cardiac fibre orientation can block wave propagation. The waves propagating across the fibres can be blocked, once they transfer to a propagation along the fibres. The reason for this block is the source-sink mismatch: the cells in a region of slow conduction can not efficiently depolarize cells in another region with fast conduction. In the opposite direction, waves can propagate without any delays and even slightly accelerate when approaching the border zone. As a result, the border between the regions of different cells alignment serves as a “diode”, that breaks the symmetry in the heart and produce a re-enty.

In **Chapter 1** we have demonstrated the arrhythmogenicity of the border between the areas with orthogonal fibre directions in a generic FitzHugh-Nagumo model [1, 2]. We have reproduced the delays in transversal to longitudinal propagation and the accelerations of the waves (or “leaps”) in the

opposite direction. We have shown, that theoretically, the delay can increase up to infinity, resulting in a full block in one direction, or it can become that high, that only every second or third way can propagate (so-called, Wenckebach rhythm). We have proposed the scenario of how this block may lead to reentry initiation. However, the full block was not observed in the experiments in neonatal rat ventricular monolayers.

In **Chapter 2** we have investigated further if a uni-directional block due to anisotropy can occur in a human heart. We have used a detailed ionic Ten Tusscher model [3] for human cardiomyocytes. Our simulations predict that in normal conditions the typical anisotropy of the human heart ($AR = 2.0$) should not cause the block of propagation. However, in pathological conditions, such as severe hyperkalemia, uni-directional block occurs for the samples with relatively low anisotropy, lower than the typical anisotropy of the ventricles. We concluded, that the normal anisotropic structure of the heart may turn into an arrhythmogenic substrate in hyperkalemia.

In the same paper we have also studied the effects of various drugs on the block of propagation. We have found, that antiarrhythmic drugs of class I (blocking sodium current I_{Na}) and class IV (blocking calcium current I_{Ca}) have a pro-arrhythmogenic effect, by increasing the probability of the propagation block due to source-sink mismatch. The inhibition of the inward rectifier K^+ current (I_{K1}) substantially decreased the range of anisotropy ratios, for which the block occurred. Therefore, suppression of I_{K1} should be the most effective way to prevent the waveblock in the areas of abrupt change in anisotropy.

After studying the extreme case of two areas with orthogonal fibre directions, in **Chapter 3** we considered a case of many areas with moderate variations in cells alignment. The idea behind this study is that local cell clustering and co-orientation, which is often seen in experimental preparations, may affect the wave propagation on a larger scale. We have generated samples with local anisotropy by dividing them into triangles with a fixed fibre direction within each element of the mesh and smoothly linked them together on the edges. At the same time, my colleagues have prepared samples of neonatal cardiac culture grown on the irregular nets made of polymer nanofibres. The density of the polymer nanofibres determined the size of the clusters of

aligned cells. We have shown together, both *in silico* and *in vitro*, that the local alignment perturbed wave propagation. Bigger clusters with higher anisotropy had more influence on the wave propagation. In simulations, clusters as big as $1/20$ of the wavelength, substantially decreased the maximal captured frequency of the wave propagation, meaning that the high-frequency wave trains could not propagate in a patterned tissue due to many blocks of propagation and wavebreaks. These predictions were in agreement with the experiment, which showed that the tissue with the clusters bigger than $40\ \mu\text{m}$ could not capture stimulations with the frequency higher than 3 Hz. The main purpose of this study was to show that the microstructure of the tissue could not be neglected. Even if the propagation is overall isotropic, local cells clusterisation can substantially perturb wave propagation.

The studies of the anisotropic tissues, presented in **Chapters 1–3**, have motivated us to study the phenomena of the anisotropic waves propagation in more details. It was not clear, which microscopic events contributed to the macroscopic anisotropy[4]. There were two main hypothesis: that cell-to-cell coupling determines the anisotropy, or that the waves propagate in a zig-zag manner across the fibres, which delays transversal propagation. However, any attempt to investigate the origin of anisotropy required a realistic geometry of the cells, with the correct area, elongation, and complexity of the shape.

In **Chapter 4** we proposed a virtual model of the cardiac tissue, that reproduced the geometry of cardiac cells. We based our model on the Cellular Potts Model model formalism, or, more specifically, on the Glazier-Graner-Hogeweg model [5–7]. We have included the two major cell types in our model: cardiomyocytes and cardiac fibroblasts. The cells in our model maintained their volume, interacted via type-specific adhesion, and, most importantly, they attached to the substrate and spread out. The spreading of the cells is a complex process, which involves actin polymerisation and destruction, integrin complexes formations, etc. We have focused on the dynamics of the attachment site, neglecting the details on the molecular scale. As a result, we obtained the cells with a polygonal shape, which is typical for both types of cardiac cells. With my colleagues, we have gathered a large database of the cell shapes and adjusted the model to reproduce them. We were able to fit the area, elongation, number of protrusions and coverage of the convex hull.

We further used virtual tissues in electrophysiological studies. We have prepared isotropic and anisotropic samples of virtual and real (experimental) tissue with approximately 35% of fibroblasts. We compared the wave propagation recorded with optical mapping with simulations. The wavefront had similar complexity in both cases. Our model predicted a limited range of the possible anisotropy ratios, assuming that the ionic channels may be distributed on the cell membrane either uniformly or non-uniformly. If most of the channels were localised at the ends of the cells, the anisotropy ratio reached its highest value of 2.7. If channels were distributed uniformly, the anisotropy ratio dropped down to 1.5, but still not to 1 meaning that longitudinal and transversal velocity were not equal. We suggested that in was due to the interstitial fibrosis, which caused zig-zag propagation in the transverse direction and limited the minimal value of the anisotropy. The simulated range of anisotropy ratios corresponded to the range observed in experiments.

Finally, in **Chapter 5** we applied our new model of the virtual tissue to explain the paradoxical wave propagation in samples with high fibrosis. The phenomenon was observed in neonatal rat ventricular cell cultures, that the samples with up to 75% of fibroblasts were still able to contract synchronously and conduct electrical signals. The immunohistochemical imaging showed that cardiomyocytes were organised in a complex branching network, that wired the whole sample. To explain this phenomenon, we tried several hypotheses. First, we assumed that differential adhesion, diffusion limited aggregation or contact inhibition may explain the formation of these branching structure. These mechanisms were used to explain branching patterns in angiogenesis but did not work in densely packed monolayers of cardiac tissue. We have finally succeeded to reproduce the branching structure when we included syncytium formation in a model. Cardiomyocytes in our model align their cytoskeletons to form a syncytium, which results in the formation of a branching structure. This structure wires the whole sample if there are only 28% of cardiomyocytes in the tissue. The proposed hypothesis allows to reproduce the morphology of cell clusters and explains the paradoxical wave propagation in samples with high fibrosis.

Overall the results of this thesis show that the architecture of the tissue plays an essential arrhythmogenic role. We have developed a novel computa-

tional technique which allows one to study tissue growth and effects of tissue architecture on the wave propagation.

Future directions As future research, we propose to investigate further the relation between structure and function, to obtain more insights in cardiac arrhythmogenesis. The model in its current state can already be utilised to answer many scientific questions, such as the principles of arrhythmogenicity of remodelled tissue or mechanisms of formation of various fibrotic patterns. Especially, the most valuable results could be attained if the model is used in combination with experiments, as we did in most of the studies above.

The model could also be extended into three dimensions (3D), which will, however, require much more computational resources for simulations. There is already plenty of data available regarding 3D shapes and positions of the cells, collagen fibers, blood vessels and extracellular space [8], and also how these structures change in remodelling. The 3D images of collagen fibers provide locations and directions of the extracellular matrix. These data on ECM can be used to describe substrate in the model, similarly to the fibres used in our studies in two dimensions. The remaining data on cell shapes and relative positions can be used for parametrisation of the model. Therefore, such extension of a modelling framework should be feasible, since the mechanisms of cells protrusion, cell-cell and cell-matrix interaction should remain the same as in two dimensions, and the necessary data for quantitative validation already exists. In three dimensions, all the effects related to percolation would be remarkably different, since the cells or signals had more paths to go around. This would apply both to morphological and electrical processes.

Despite the fact that there is a vast amount of structural data available, there are no records of dynamical changes in cardiac tissue. This kind of data could have provided necessary means for validation of the dynamic cell motility if it had been available. Some research has been done on motility of fibroblasts seeded on various substrates [9, 10]. Tracking of these movements revealed the acquired asymmetry of cell shapes on the ECM and related persistence of movement in the direction along ECM. A similar study for cardiomyocytes may give the so much required parameters of cell movements, such as speed and persistence, and contribute to the validity of this model.

Similarly, the model in its current state can mimic structural changes during cardiac remodelling. For this, the target volume of the cells and stiffness of the cytoskeleton should be adjusted to reproduce cells hypertrophy. Also, it is rather simple to add fibroblasts proliferation in a model and reproduce cardiac fibrosis. The model then could reveal the exact mechanisms that lead to cardiac arrhythmias in remodelled tissue, and various approaches to its treatment can be tested *in silico*.

Many studies also highlighted the importance of mechanical conditions in cardiogenesis, especially the fact that periodic mechanical and/or electrical stimulation can induce maturation of the cells [11–14]. The studies were conducted with the use of the human induced pluripotent stem cells (hiPSC), and they revealed that cyclic stretching of the samples resulted in the development of longer sarcomeres and overall enhanced contractile force levels [12]. Static stress applied on the tissue also led to cells elongation and alignment[13]. Recent studies also show that periodic contractions predictably change the metabolism of the cardiomyocytes by increased production of mitochondria [14]. Overall, these findings emphasise the crucial role of the periodic mechanical contractions coupled with electrical stimulation during heart development.

Our model can potentially be applied to studies of the mechano-electrical feedback during early cardiogenesis. In this thesis, however, we have first virtually “grow” cardiac tissue and only then studied its electrical properties. Although, these two parts can also be intermingled and executed alternately. A morphological mechanism coupled with electrical waves could be suggested. For example, the stiffness of the cytoskeleton can gradually increase if the cell was stimulated. Then, by alternating computation of the morphological and electrophysiological models this coupling could be studied. We have developed and optimised all the necessary software needed for this. The only question left is the nature of this mechano-electrical coupling during heart development.

Improved understanding of how the tissue architecture is formed could also eventually provide control over tissue growth and age-related remodelling. The further joint *in vitro*–*in silico* research on cardiac morphogenesis may create new approaches to arrhythmia treatment aiming at regulation of the structural changes.

Samenvatting

De samentrekking van het hart wordt gereguleerd door propagerende excitatiegolven. Abnormale regimes van de golfvoortplanting, of *hartritmestoornissen*, komen vaak voort uit de blokkering van de voortplanting in een specifieke regio. De golf gaat deze regio rond, komt opnieuw in dezelfde regio en vormt een persistente cyclus, *cardiale reentry* genoemd. Dit is een van de belangrijkste mechanismen van hartritmestoornissen.

Het normale hart heeft een complexe structuur, die is samengesteld uit bundels langwerpige hartcellen. Aangenomen wordt dat deze gecompliceerde structuur een optimale samentrekking en bloedcirculatie verzorgt. Hartbundels maken snelle signaalvoortplanting mogelijk in de longitudinale richting en langzame voortplanting in de transversale richting. Dit fenomeen wordt *anisotropie* genoemd. In deze thesis hebben we verschillende aspecten van anisotropie van het hartweefsel bestudeerd, zoals de vorming van hartvezelbundels, de oorsprong van anisotropie en het effect hiervan op de vorming van conductieblok en de aritmogeniteit van het weefsel. Afgezien van exciteerbare hartcellen, zijn er ook niet exciteerbare cellen bestaande uit bindweefsel: cardiale fibroblasten. Ze zijn zelfs talrijker dan cardiomyocyten in een gezond menselijk hart. De interactie tussen deze celtypes resulteert in een complexe weefselmorfologie die bijdraagt aan anisotropie en stabiliteit van de golfvoortplanting.

In **Hoofdstukken 1 en 2** hebben we een nieuw scenario van reentryformatie voorgesteld, veroorzaakt door een abrupte verandering in anisotrope richting. We hebben aangetoond dat de grenszone tussen de regio's met verschillende hartvezeloriëntatie de golfvoortplanting kan blokkeren. De golven die zich over de vezels verspreiden, kunnen worden geblokkeerd, zodra ze worden overgedragen naar een voortplanting langs de vezels. De reden voor dit blok is de verkeerde mismatch: de cellen in een regio met langzame geleiding kunnen cellen met een snelle geleiding niet efficiënt depolariseren in een ander gebied. In de tegenovergestelde richting kunnen golven zich zonder vertragingen voortplanten en zelfs iets versnellen bij het naderen van het grensgebied. Als gevolg gedraagt de grens tussen de gebieden met verschillende celuitlijningen zich als een "diode", die de symmetrie in het hart verbreekt en een reentry produceert.

In **Hoofdstuk 1** hebben we de arrhythmogeniciteit van de grens tussen de gebieden met orthogonale vezelrichtingen in een generiek FitzHugh-Nagumo-model [1, 2] uitgewerkt. We hebben de vertragingen van transversale naar longitudinale propagatie en de versnellingen van de golven (of “sprongen”) in de tegenovergestelde richting gereproduceerd. We hebben aangetoond dat theoretisch de vertraging kan oplopen tot oneindig, wat resulteert in een volledig blok in één richting, of het kan zo hoog worden dat alleen elke seconde of derde weg zich kan voortplanten (het zogenaamde Wenckebach-ritme). We hebben aangetoond hoe dit blok kan leiden tot de initiatie van reentry. Echter, een volledige blok werd niet waargenomen in experimenten in neonatale rattenventriculaire monolagen.

In **Hoofdstuk 2** hebben we verder onderzocht of een unidirectioneel blok door anisotropie in een menselijk hart kan voorkomen. Hiervoor hebben we het gedetailleerd ionisch Ten Tusscher-model [3] voor menselijke cardiomyocyten gebruikt. Onze simulaties voorspellen dat onder normale omstandigheden de typische anisotropie van het menselijk hart ($AR = 2.0$) het voortplantingsblok niet zou moeten veroorzaken. Echter, in pathologische omstandigheden, zoals ernstige hyperkaliëmie, vindt unidirectioneel blokkeren plaats voor monsters met relatief lage anisotropie, lager dan de typische anisotropie van de ventrikels. Daarom concludeerden we dat de normale anisotrope structuur van het hart kan veranderen in een aritmogeen substraat in hyperkaliëmie.

In dezelfde paper hebben we ook de effecten van verschillende medicijnen op het propagatieblok bestudeerd. We hebben ontdekt dat anti-aritmica van klasse I (blokkeren van I_{Na}) en klasse IV (blokkeren van I_{Ca}) een pro-aritmogeen effect hebben, door de kans op het propagatieblok te vergroten (source-sink wanverhouding). De remming van de binnenkomende rectificator K^+ stroom (I_{K1}) verminderde aanzienlijk het bereik van anisotropie verhoudingen, waarvoor de blokkering plaatsvond. Daarom zou onderdrukking van I_{K1} de meest effectieve manier moeten zijn om het golfblok te voorkomen in de gebieden van abrupte verandering in anisotropie.

Na het bestuderen van het extreme geval van twee gebieden met orthogonale vezelrichtingen, hebben we in **Hoofdstuk 3** het volgende geval bestudeerd: veel gebieden met matige variaties in de uitlijning van cellen. Het idee achter deze studie is dat clustering van lokale cellen en co-oriëntatie, wat

vaak wordt gezien in experimentele preparaten, de golfvoortplanting op grotere schaal kan beïnvloeden. We hebben monsters gegenereerd bestaande uit aan elkaar gelinkte driehoeken van variërende grootte met een vaste vezelrichting in elk driehoek. Tegelijkertijd hebben mijn collega's monsters gemaakt van neonatale hartkweken die zijn gegroeid op de onregelmatige netten gemaakt van polymeer nanovezels. De dichtheid van de polymeer nanovezels bepaalde de grootte van de clusters van de uitgelijnde cellen. We hebben samen aangetoond, *in silico* en *in vitro*, dat de lokale uitlijning de golfvoortplanting verstoort. Grotere clusters met hogere anisotropie hadden meer invloed op de golfvoortplanting. In simulaties verminderde de maximale mogelijke stimulatiefrequentie aanzienlijk voor clusters met grootte $1/20$ van de golflengte. Dit betekent dat hoogfrequente golftreinen zich niet konden voortplanten in een patroonweefsel. Deze voorspellingen waren inderdaad in overeenstemming met het experiment, waaruit bleek dat het weefsel met de clusters groter dan $40\ \mu\text{m}$ geen stimulaties kon opvangen met een frequentie hoger dan 3 Hz. Het belangrijkste doel van deze studie was om te laten zien dat de microstructuur van het weefsel niet kan worden verwaarloosd. Zelfs als de propagatie algeheel isotroop is, kan clustering van lokale cellen de golfvoortplanting aanzienlijk verstoren.

De studies van de anisotrope weefsels, gepresenteerd in **Hoofdstukken 1–3**, hebben ons gemotiveerd om de fenomenen van de anisotrope golvenvoortplanting in meer detail te bestuderen. Het was niet duidelijk, welke microscopische gebeurtenissen hebben bijgedragen aan de macroscopische anisotropie [4]. Er waren twee hoofdhypothesen: dat cel-naar-cel koppeling de anisotropie bepaalt, of dat de golven zigzag over de vezels propageren, wat de transversale voortplanting vertraagt. Elke poging om de oorzaak van anisotropie te onderzoeken, vereiste echter een realistische geometrie van de cellen, met het juiste gebied, de juiste rek en de complexiteit van de vorm.

In **Hoofdstuk 4** hebben we een virtueel model van het hartweefsel gemoedeerd, dat de exacte geometrie van de hartcellen voorstelt. We hebben ons model gebaseerd op het cellulair Potts-modelformalisme, of, meer specifiek, op het Glazier-Graner-Hogeweg model [5–7]. We hebben de twee belangrijkste celtypen in ons model opgenomen: cardiomyocyten en cardiale fibroblasten. De cellen in ons model behielden hun volume, de interactie via type-specifieke ad-

hesie, en, belangrijker nog, ze werden aan het substraat gehecht en uitgespreid. Het verspreiden van de cellen is een complex proces, dat actine polymerisatie en vernietiging, integrinecomplexformaties, ... omvat. We hebben ons gericht op de dynamiek van de hechtingsplaats, waarbij we de details op moleculaire schaal hebben verwaarloosd. Als resultaat hebben we cellen verkregen met een veelhoekige vorm, die kenmerkend is voor beide typen hartcellen. Met mijn collega's hebben we een grote database van celvormen verzameld en het model aangepast om deze te reproduceren. Hierbij zijn we erin geslaagd het gebied, de verlenging, het aantal uitsteeksels en dekking van de convexe romp weer te geven.

We hebben verder virtuele weefsels gebruikt in elektrofysiologische studies. We hebben isotrope en anisotrope monsters gemaakt van virtueel en reëel (experimenteel) weefsel met ongeveer 35% fibroblasten. We hebben de gegenereerde golfvoortplanting van optische mapping (experiment) met simulaties vergeleken. Het golfvront had in beide gevallen een vergelijkbare complexiteit. Ons model voorspelde een beperkt bereik van de mogelijke anisotropieverhoudingen, ervan uitgaande dat de ionkanalen op het celmembraan gelijkmatig of niet-uniform kunnen worden verdeeld. Als de meeste kanalen aan de uiteinden van de cellen waren gelokaliseerd, bereikte de anisotropieverhouding de hoogste waarde van 2.7. Als de kanalen gelijkmatig werden verdeeld, daalde de anisotropieverhouding wel tot 1.5, maar niet tot 1, maw de longitudinale en transversale snelheid waren niet gelijk. Om dit te verklaren, suggereren we dat dit fenomeen door interstitiële fibrose veroorzaakt wordt, wat zigzagpropagatie in de transversale richting veroorzaakte, en hierdoor de minimale waarde anisotropie limiteert. Onze gesimuleerde anisotropieverhoudingen komen overeen met het bereik dat werd waargenomen in experimenten.

Ten slotte pasten we in **Hoofdstuk 5** ons nieuwe model van het virtuele weefsel toe om de paradoxale golfvoortplanting in monsters met hoge fibrose te verklaren. Het fenomeen werd waargenomen in neonatale celculturen van rattencellen: monsters met tot 75% fibroblasten konden nog steeds synchron samentrekken en elektrische signalen geleiden. De immunohistochemische beeldvorming toonde aan dat cardiomyocyten georganiseerd waren in een complex vertakt netwerk, dat het hele monster bekabelde. Om dit fenomeen te verklaren, hebben we verschillende hypothesen geprobeerd. Eerst hebben

we aangenomen dat differentiële adhesie, diffusie beperkte aggregatie of contactremming de vorming van deze vertakkingsstructuur kan verklaren. Deze mechanismen werden gebruikt om vertakkingspatronen in angiogenese te verklaren, maar werkten niet in dicht gepakte monolagen van hartweefsel. We zijn er eindelijk in geslaagd de vertakkingsstructuur te reproduceren wanneer we syncytiumvorming in een model hebben opgenomen. Cardiomyocyten in ons model richten hun cytoskeletonten op elkaar om een syncytium te vormen, wat resulteert in de vorming van een vertakkingsstructuur. Deze structuur bekaamt het hele monster als er slechts 28% cardiomyocyten in het weefsel aanwezig zijn. Deze hypothese maakt het mogelijk om de morfologie van celclusters te reproduceren en verklaart de paradoxale golfvoortplanting in monsters met hoge fibrose.

Over het algemeen laten de resultaten van dit proefschrift zien dat de architectuur van het weefsel een belangrijke aritmogene rol speelt. We hebben een nieuwe computationele techniek ontwikkeld waarmee we weefselgroei en effecten van weefselarchitectuur op de golfvoortplanting kunnen bestuderen.

Toekomstperspectieven Als toekomstig onderzoek stellen we voor om inzichten in hartritmestoornissen te verkrijgen door het verder bestuderen van de relatie tussen structuur en functie van hartcellen. Het model in zijn huidige staat kan al worden gebruikt om veel wetenschappelijke vragen te beantwoorden, zoals de principes van arrhythmogeniciteit van het remodelerende weefsel of mechanismen van de vorming van verschillende fibrotische patronen. De meest waardevolle resultaten kunnen worden behaald als het model wordt gebruikt in combinatie met experimenten, zoals we in de meeste van de bovenstaande studies hebben gedaan.

Het model kan ook worden uitgebreid naar drie dimensies (3D), waarvoor echter veel meer rekenbronnen nodig zullen zijn voor simulaties. Er zijn al veel gegevens beschikbaar over 3D-vormen en posities van de cellen, collageenvezels, bloedvaten en de extracellulaire ruimte. De 3D-beelden van collageenvezels verschaffen locaties en richtingen van de extracellulaire matrix. Deze data met betrekking tot de ECM kan gebruikt worden om het substraat in het model te beschrijven in een soortgelijke manier als gedaan is voor de vezels in onze studies in twee dimensies. De resterende gegevens over celvormen en

relatieve posities kunnen worden gebruikt voor parametrisering van het model. Daarom moet de verlenging van dit modelleerkader haalbaar zijn, aangezien de mechanismen van celprotrusie, cel-cel-, en cel-matrix interacties gelijk blijven aan die in twee dimensies en de noodzakelijke gegevens voor de kwantitatieve validatie al bestaan. In drie dimensies zouden alle effecten met betrekking tot percolatie opmerkelijk anders zijn aangezien de cellen of signalen meer paden hebben om obstakels te ontwijken. Dit zou zowel gelden voor morfologische als elektrische processen.

Ondanks het feit dat er een grote hoeveelheid structurele gegevens beschikbaar is, zijn er geen gegevens over dynamische veranderingen in hartweefsel. Dit soort gegevens zou voorzien in de noodzakelijke middelen voor het valideren van de dynamische celmotiliteit als deze beschikbaar was geweest. Er is enig onderzoek gedaan naar de beweeglijkheid van fibroblasten gezaaid op verschillende substraten [9, 10]. Het volgen van deze bewegingen onthulde de verworven asymmetrie van celvormen op de ECM en de daarmee samenhangende persistentie van beweging in de richting van de ECM. Een soortgelijk onderzoek voor cardiomyocyten kan de noodzakelijke parameters voor celbewegingen geven, zoals snelheid en persistentie, en bijdragen aan de validiteit van dit model.

Het model kan in zijn huidige staat eveneens structurele veranderingen tijdens hartremodellering nabootsen. Hiervoor moeten het doelvolumen van de cellen en de stijfheid van het cytoskelet worden aangepast om hypertrofie van cellen te reproduceren. Het is ook vrij eenvoudig om proliferatie van fibroblasten in een model toe te voegen en cardiale fibrose te reproduceren. Het model kan dan het exacte mechanisme aangeven dat leidt tot hartritmestoornissen in geremodelleerd weefsel. Verschillende methodes van aanpak voor de behandeling hiervan kunnen getest worden *in silico*.

Vele studies hebben ook gewezen op het belang van mechanische omstandigheden in cardiogenese. In het bijzonder het feit dat periodieke mechanische en/of elektrische stimulatie rijping van de cellen kan induceren [11–14]. De studies werden uitgevoerd met behulp van de humane geïnduceerde pluripotente stamcellen (hiPSC), en ze legden bloot dat cyclische rek van de monsters resulteerde in de ontwikkeling van langere sarcomeren en algehele verhoogde samentrekkingskracht niveaus [12]. Statische stress op het weefsel leidde ook

tot cel-elongatie en alignatie [13]. Recente studies tonen ook aan dat periodieke contracties voorspelbaar het metabolisme van de hartspiercellen veranderen door een verhoogde productie van mitochondria [14]. Met elektrische stimulatie tijdens de ontwikkeling van het hart.

Ons model kan mogelijk worden toegepast op de studie van mechano-elektrische feedback tijdens vroege cardiogenese. In dit proefschrift hebben we echter eerst hartweefsel “gekweekt”, waarna we de elektrische eigenschappen hebben bestudeerd. Deze twee delen kunnen ook verwoven worden en afwisselend worden uitgevoerd. Een morfologisch mechanisme in combinatie met elektrische golven zou zo kunnen worden gesuggereerd. De stijfheid van het cytoskelet kan bijvoorbeeld geleidelijk toenemen als de cel wordt gestimuleerd. Door de berekening van de morfologische en elektrofysiologische modellen af te wisselen, kan deze koppeling bestudeerd worden. We hebben hiervoor alle benodigde software ontwikkeld en geoptimaliseerd. De enige vraag die nog rest is de aard van deze mechano-elektrische koppeling tijdens de ontwikkeling van het hart.

Verbeterd inzicht in hoe de weefselarchitectuur zich vormt kan uiteindelijk ook controle leveren op het groeien van weefsel en leeftijdsgerelateerde remodeling. Het verdere gezamenlijke onderzoek met *in vitro* – *in silico* naar de morfogenese van het hart kan nieuwe benaderingen van aritmiebehandeling creëren, gericht op de regulatie van structurele veranderingen.

References

- [1] R. FitzHugh, "Mathematical models of threshold phenomena in the nerve membrane," *The Bulletin of Mathematical Biophysics*, vol. 17, pp. 257–278, 1955.
- [2] J. Nagumo, S. Arimoto, and S. Yoshizawa, "An active pulse transmission line simulating nerve axon," *Proceedings of the IRE*, vol. 117, no. m V, pp. 2061–2070, 1962.
- [3] K. H. W. J. ten Tusscher, D. Noble, P. J. Noble, and a. V. Panfilov, "A model for human ventricular tissue.," *American journal of physiology. Heart and circulatory physiology*, vol. 286, pp. H1573–89, 2004.
- [4] I. Erofeev and K. I. Agladze, "Two models of anisotropic propagation of a cardiac excitation wave," *JETP letters*, vol. 100, no. 5, pp. 351–354, 2014.
- [5] F. Graner and J. Glazier, "Simulation of biological cell sorting using a two-dimensional extended Potts model.," *Physical review letters*, vol. 69, pp. 2013–2016, 1992.
- [6] J. Glazier and F. Graner, "Simulation of the differential adhesion driven rearrangement of biological cells.," *Physical review. E, Statistical physics, plasmas, fluids, and related interdisciplinary topics*, vol. 47, pp. 2128–2154, 1993.
- [7] N. J. Savill and P. Hogeweg, "Modelling Morphogenesis: From Single Cells to Crawling Slugs," *Journal of Theoretical Biology*, vol. 184, no. 3, pp. 229–235, 1997.
- [8] T. Seidel, J. C. Edelmann, and F. B. Sachse, "Analyzing Remodeling of Cardiac Tissue: A Comprehensive Approach Based on Confocal Microscopy and 3D Reconstructions," *Annals of Biomedical Engineering*, vol. 44, no. 5, pp. 1436–1448, 2015.
- [9] A. D. Doyle, F. W. Wang, K. Matsumoto, and K. M. Yamada, "One-dimensional topography underlies three-dimensional fibrillar cell migration.," *The Journal of cell biology*, vol. 184, pp. 481–90, 2009.
- [10] Q. Y. Tang, W. X. Qian, Y. H. Xu, *et al.*, "Control of cell migration direction by inducing cell shape asymmetry with patterned topography.," *Journal of biomedical materials research. Part A*, vol. 103, pp. 2383–93, 2015.
- [11] R. Zhu, A. Blazeski, E. Poon, *et al.*, "Physical developmental cues for the maturation of human pluripotent stem cell-derived cardiomyocytes," *Stem cell research & therapy*, vol. 5, no. 5, p. 117, 2014.

-
- [12] G. Kensah, A. Roa Lara, J. Dahlmann, *et al.*, “Murine and human pluripotent stem cell-derived cardiac bodies form contractile myocardial tissue in vitro,” *European heart journal*, vol. 34, no. 15, pp. 1134–1146, 2012.
 - [13] N. L. Tulloch, V. Muskheli, M. V. Razumova, *et al.*, “Growth of engineered human myocardium with mechanical loading and vascular coculture,” *Circulation research*, vol. 109, pp. 47–59, 2011.
 - [14] B. M. Ulmer, A. Stoehr, M. L. Schulze, *et al.*, “Contractile Work Contributes to Maturation of Energy Metabolism in hiPSC-Derived Cardiomyocytes,” *Stem cell reports*, vol. 10, no. 3, pp. 834–847, 2018.

Acknowledgments

I would like to thank my scientific advisors, Prof. Alexander V. Panfilov and Prof. Konstantin I. Agladze. It has been an honor to be a Ph.D. student under supervision of these outstanding scientists, who were at the very origins of excitable media studies in the 1980s in Pushchino. I am very grateful to the immense knowledge and, particularly, their vision of science that they have shared with me.

I am grateful to the Examination committee: Prof. Dirk Poelman (UGent), Prof. Henri Verschelde (UGent), Prof. Roeland Merks (CWI Amsterdam), Prof. Olivier Bernus (IHU Liryc, Bordeaux), Dr. D.A.Pijnappels (LUMC, Leiden), Dr. Hans Dierckx (UGent), and Dr. Nele Vandersickel (UGent), for their insightful comments and hard questions on the private defence which challenged me to widen my vision of the work as a whole and showed me more future perspectives. A very special gratitude goes to Professor Roeland Merks, who has helped me a lot to understand and set up the morphological model at first, provided me with the code, and also advised on the development of the model along the way.

I thank my fellow officemates, Tim De Coster, Nele Vandersickel, Kseniya Parkhomenko, and also Enid Van Nieuwenhuyse, who not only advised me on scientific work, but also cared so much about my mental well-being, improved my social skills and language, and showed me so many fun and interesting places in Belgium. My special gratitude goes to Hans Dierckx, Sander Arens and Ivan Kazbanov, for their immense experience and knowledge that they shared with me, and for their help with setting up algorithms for my model. I would like to thank once again Tim De Coster and Nele Vandersickel for their help with translation of the Summary of my thesis in Dutch.

I express my gratitude to my colleagues back in Moscow: Valeriya Tsvelaya, Aygul Nizamieva, Anna Krasheninnikova, Alisa Podgurskaya, Luibov Selina, for their persistent and accurate work on cell culture experiments. I would like to express gratitude to Nadezhda Agladze and Yulia Orlova, for their careful supervision of these experiments. Especially, I would like to thank Alexander Teplenin, who was also preparing experiments for the first Chapters of my thesis back in Moscow, and then continued supporting me during his Ph.D. in

Leiden. His engineering creativity helped us many times to achieve our goals with the smart design of the experiments.

I would like to express my sincere gratitude to many other excellent scientists who consulted me and critiqued along the way: Prof. Arkady Pertsov, Dr. Daniel Pijnappels, Dr. Antoine de Vries, Dr. Jan Kucera, and many-many others. Thank you for your opinions and your vision.

I would like to thank my best old friend, Sergey Efimov, who helped me to improve my figures and also designed the cover of this thesis.

A very special gratitude goes out to the Bijzonder Onderzoeksfonds (BOF) and Russian Foundation for Basic Research (RFBR) for providing the funding for the work.

Last but not the least, I would like to thank my family: my parents, grandparents and my beloved husband, for supporting me and pushing me forward to finish my PhD and to never give up.